Aus dem Bereich Physiologie
Theoretische Medizin und Biowissenschaften
der Medizinischen Fakultät
der Universität des Saarlandes, Homburg/Saar

Maturation, acidification and fusion of cytotoxic granules in primary $CD8^+$ T lymphocytes

**Dissertation zur Erlangung des Grades eines Doktors der Naturwissenschaften der Medizinischen Fakultät
der UNIVERSITÄT DES SAARLANDES
2019**

vorgelegt von: Praneeth Chitirala
geb. am: 06.07.1986 in Kavali, India.

Tag des Promotionskolloquiums:	05.06.2020
Dekan:	Prof. Dr. M. D. Menger
Vorsitzender:	----------
Berichterstatter:	Prof. J. Rettig Prof. M. Hoth Prof. St. Herlitze

Dedicated to my father

Narasimha Rao & mother

Leelavathi

Table of Contents

Abbreviations

APC	Antigen presenting cell
a.u	Arbitrary units
BSA	Bovine serum albumin
CTL	Cytotoxic T lymphocyte
°C	Degree Celsius
CGs	Cytotoxic granules
$[Ca^{2+}]_i$	Intracellular calcium concentration
CCCP	Carbonyl cyanide 3-chlorophenylhydrazone
cSMAC	Central supra-molecular activation cluster
dSMAC	Distal supra-molecular activation cluster
FHL	Familial hemophagocytic lymphohistiocytosis
GFP	Green fluorescent protein
h	Hour
HEPES	4-(2-Hydroxyethyl)-1-piperazineethanesulfonic acid
IS	Immunological synapse
MTOC	Microtubule organizing center
PBS	Phosphate buffer saline
pH	Potential hydrogen
$[pH]_{CG}$	Cytotoxic granule pH concentration
pSMAC	Peripheral supra-molecular activation cluster
PCR	Polymerase chain reaction
PCTV	Pre-chylomicron transport vesicle
SEA	Staphylococcal enterotoxin A
SEM	Standard error of the mean
SNAP	Synaptosomal-associated protein
SIM	Structured illumination microscopy
SNAREs	Soluble N-ethyl-maleimide-sensitive attachment protein receptor
Syb2	Synaptobrevin2
TCR	T-cell receptor
t-SNARE	Target-SNARE
mTFP	monomeric-Teal fluorescent protein
TIRFM	Total internal reflection microscope
v-SNARE	Vesicular-SNARE
VAMP	Vesicle associated membrane protein

Acknowledgements

I would first like to express my deepest and highest gratitude to my supervisor Prof. Dr. Jens Rettig, for giving me the opportunity to initiate my Doctoral thesis under his guidance. Without his encouragement and motivation, I would have not been able to successfully complete my thesis. I will always be grateful to him for being such a great advisor, mentor and importantly a wonderful person.

I would like to extend my thanks to Dr. David Stevens, Dr. Elmar Krause, Dr. Ute Becherer, Dr. Claudia Schirra, Dr. Varsha Pattu, Dr. Hsin Fang Chang, Dr. Hawraa Bzeih and Dr. Marcel Lauterbach for their support and guidance during new experiments particularly in the beginning of my PhD.

I sincerely thank our collaborators Prof. Veit Flockerzi and all his group members for helping me with experiments at his laboratory during the early days of my PhD. I thank also Prof. Markus Hoth and Prof. Dieter Bruns and all their group members for helping me in some important experiments and in general discussions.

I would like to thank Dr. Joe Casey and all IRTG1830 members for great scientific discussions during the meetings. I also thank IRTG1830 for funding and Dr. Gabrielle Amoroso for her excellent support during my PhD.

I thank especially Dr. Madhurima Dhara for valuable discussions that led to the VAMP7 project.

I thank all my friends and lab members for their excellent company including Dr. Olga Ratai, Marwa Sleiman, Angelina Staudt and Ali Shahib for being very friendly and helpful. I especially thank Mazen Makke, Mayur Dembla, Ekta Dembla, Ali Harb and Ahmed Shaaban for always being there for help and for being such good friends that made my stay in Germany memorable. I thank Anja Bergsträßer, Katrin Sandmeier, Nicol Rothgerber, Anne Weinland, Margarete Klose, Jacqueline Vogel and Tamara Paul for excellent technical help. I extend my thanks to Bernadette Schwarz and Josephine Kretschmer for their wonderful assistance and help.

I sincerely thank my first supervisor Dr. Subba Rao Gangisetty in India for giving me an opportunity in his lab that started my scientific career.

My special thanks to TVHomburg Badminton for giving me the best friends of my life during my stay in Homburg.

Finally and most importantly, I would like to thank my family, my wife as well as colleague Keerthana Ravichandran for her lovely support and motivation throughout my journey making it much effortless for me to finish my PhD.

-----List of figures-----

Zusammenfassung

Zytotoxische T-Lymphozyten (CTLs) spielen eine wichtige Rolle im Immunsystem unseres Körpers. Ihre hauptsächliche Effektorfunktion besteht darin, viral infizierte und tumorartige Zielzellen zu erkennen und abzutöten. Sie enthalten zytotoxische Substanzen wie Granzyme und Perforin in speziellen sekretorischen Vesikeln, die als zytotoxische Granula (CGs) bezeichnet werden und durch Exozytose an der als Immunsynapse (IS) bezeichneten Kontaktstelle von CTL und Zielzelle freigesetzt werden. Wir untersuchten, wie sich die pH-Regulierung in CGs auf die Funktion der primären Maus-CD8+-T-Zellen auswirkt. Wir identifizierten die a3-Untereinheit der vakuolären ATPase als einen wichtigen Kandidaten, der für die Ansäuerung von CGs verantwortlich ist. Unter Verwendung eines neu generierten CG-spezifischen pH-Indikators bestimmten wir den pH-Wert von CGs mit 6,11 ± 0,2. Der Knockdown der a3-Untereinheit erhöhte den pH-Wert in CGs auf 6,8 und führte zu einer signifikant verringerten Abtötung von p815-Zielzellen. Außerdem untersuchten wir die CG-Sekretion mit Hilfe der TIRF-Mikroskopie. Die Reduktion der a3-Untereinheit in Maus-CTLs ergab eine 75%ige Verringerung der CG-Sekretion, die durch einen fehlerhaften Transport der CGs zur IS verursacht wurde. Wir haben durch elektronenmikroskopische Untersuchungen gezeigt, dass der a3-Knockdown in CTLs die Biogenese von CGs unverändert lässt. Aus unseren hochauflösenden mikroskopischen TIRF- und STED-Daten schließen wir, dass die a3-Untereinheit der vATPase nicht nur für die Ansäuerung von CGs verantwortlich ist, sondern auch zum effizienten Transport der CGs zur IS beiträgt. Darüber hinaus haben wir unsere Studie erweitert, um die vesikulären Komponenten von CGs zu identifizieren, die an der Fusion beteiligt sind. Die familiäre hämophagozytäre Lymphohistiozytose (FHL) ist eine genetisch bedingte Erkrankung, die durch Mutationen vieler Gene verursacht wird, die in Plasmamembran-Fusionsmaschinen funktionieren. In dieser Studie identifizierten wir VAMP7 als einen wesentlichen Bestandteil der vesikulären Fusionsmaschinerie von primären humanen CD8+T-Zellen. Eine SIM-Mikroskopieanalyse verschiedener VAMP-Isoformen zeigte, dass nur VAMP7 zusammen mit Granulamarkern (Granzym B und Perforin) lokalisiert ist und gleichzeitig mit ihnen an der IS fusioniert. Ferner verringerte die Herunterregulierung der VAMP7-Proteinexpression die Abtötungseffizienz von T-Zellen bei Inkubation mit RAJI-Zielzellen signifikant. Interessanterweise interferierte VAMP7 nicht mit der frühen Signalgebung von T-Zellrezeptoren. Biochemische Assays zeigten, dass VAMP7 seine Funktion in einem SNARE-Komplex mit Syntaxin11 und SNAP-23 an der Plasmamembran ausübt. Die Überexpression der VAMP7-Longin-Domäne in CTLs hemmt die Fusion von CGs spezifisch, ohne die Fusion von Recycling-Endosomen zu beeinträchtigen. Unsere Daten identifizieren die essentiellen Komponenten der Fusionsmaschinerie in T-

Zellen. Diese Kenntnisse könnten einen Ausgangspunkt für die Entwicklung potenzieller Medikamente in der Immuntherapie darstellen, die auf die für VAMP7 spezifische Longin-Domäne abzielen.

1. Introduction

1.1 Cytotoxic T Lymphocytes

Cytotoxic T Lymphocytes (CTLs) are decisive for immune surveillance against tumour cells and cells infected with viruses. The combined responses from both innate and adaptive immune systems provide the capacity to the host to fight against pathogens. CTLs and natural killer (NK) cells are the key players of innate or adaptive immunity (Peters et al., 1991). Upon activation, peripheral blood mononuclear lymphocytes (PBMCs) get differentiate into mature CTLs, which contain cytotoxic granules (CGs) with the pore-forming protein Perforin and the serine protease granzyme B (GzmB). Once the CTL recognizes its cognate target, a highly organized system of intracellular communication starts by triggering the TCR/CD3 complex. CTLs rapidly reorganize their cytoskeleton within minutes to translocate the Microtubule-organizing center (MTOC) towards the target cell followed by directed polarization of granules that are exocytosed for destroying target cells (Berke and Rosen, 1988) (Huse, 2012). Perforin monomers bind to the target cell membrane and assemble into multimeric complexes building pores on the target cell membrane that allow GzmB to enter the target cells activating apoptosis pathways through proteolytic substrate processing (Sutton et al., 2000) (Griffiths and Isaaz, 1993).

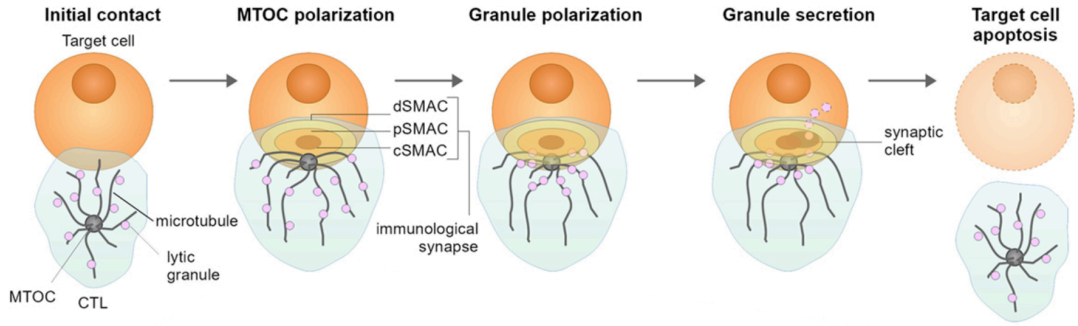

Figure 1: Assembly at the CTL synapse.
(A) Recognition of target cells by CTLs leads to the generation of the lytic immune synapse distinguished by the initiation of central supramolecular activation cluster (cSMAC) surrounded by the peripheral supramolecular activation cluster (pSMAC) and distal supramolecular activation cluster (dSMAC) followed by Microtubule-organizing center (MTOC) and CGs polarization towards the synaptic cleft. (Kabanova et al., 2018)

1.2 T cell development and differentiation

Producing the proper number and variety of cell types is critical for the physiological function of multicellular organisms. Most cell differentiation decisions are controlled by signals from widely expressed receptors that interact with germ-line ligands which are co-evolved (Freeman, 2000).

Genesis of immature $CD4^{+}CD8^{+}$ thymocytes starts in the bone marrow by committed lymphoid progenitors which arise and migrate via the blood to the primary lymphoid organ thymus (Germain, 2002b). In the thymus, these cells lose the ability

for B-cell (Pui et al., 1999) and NK-cell (Barten et al., 2001) development. The cells which develop in the thymus (aka thymocytes) undergo a sequence of maturation steps that can be distinguished based on different markers expressed on their cell surface or plasma membrane. The thymus is composed of two regions, an outer cortex and an inner medulla. Developing thymocytes are devoid of co-receptor CD4 and CD8 expression on their membrane during the earliest stages. These cells are termed double-negative (DN) committed T-cell precursors. These DN thymocytes undergo four sequential stages of differentiation by expressing CD44 and CD25 (Godfrey et al., 2012). In the process of differentiation, the cells which proceed in the direction of the αβ TCR pathway express the pre-TCR composed of the non-rearranging pre-Tα and rearranged TCR-β chains. Productive pre-TCR expression leads to increased cell multiplication along the DN4 to DP (double-positive) transition and ends with the pre-TCRα chain replaced with a newly rearranged TCR α-chain. This results in the complete formation of the αβ TCR (Germain, 2002b). Further, these DP (αβ-TCR$CD4^+CD8^+$) thymocytes interact with cortical epithelial cells which express a high density of MHC class I and II molecules associated with self-peptides. Too weak or too strong signaling can lead to either delayed or acute apoptosis. Effective maturation of T cells occurs only from the appropriate level of TCR signaling. $CD8^+$ T cells originate from thymocytes that express TCRs which recognize self-peptide-MHC-class-I complexes, whereas $CD4^+$ cells develop from TCRs that recognizes self-peptide-MHC-class-II ligands (Hazeldine and Lord, 2015). These cells will be transported from the medulla to peripheral lymphoid sites for immune surveillance (Vonboehmer et al., 1989).

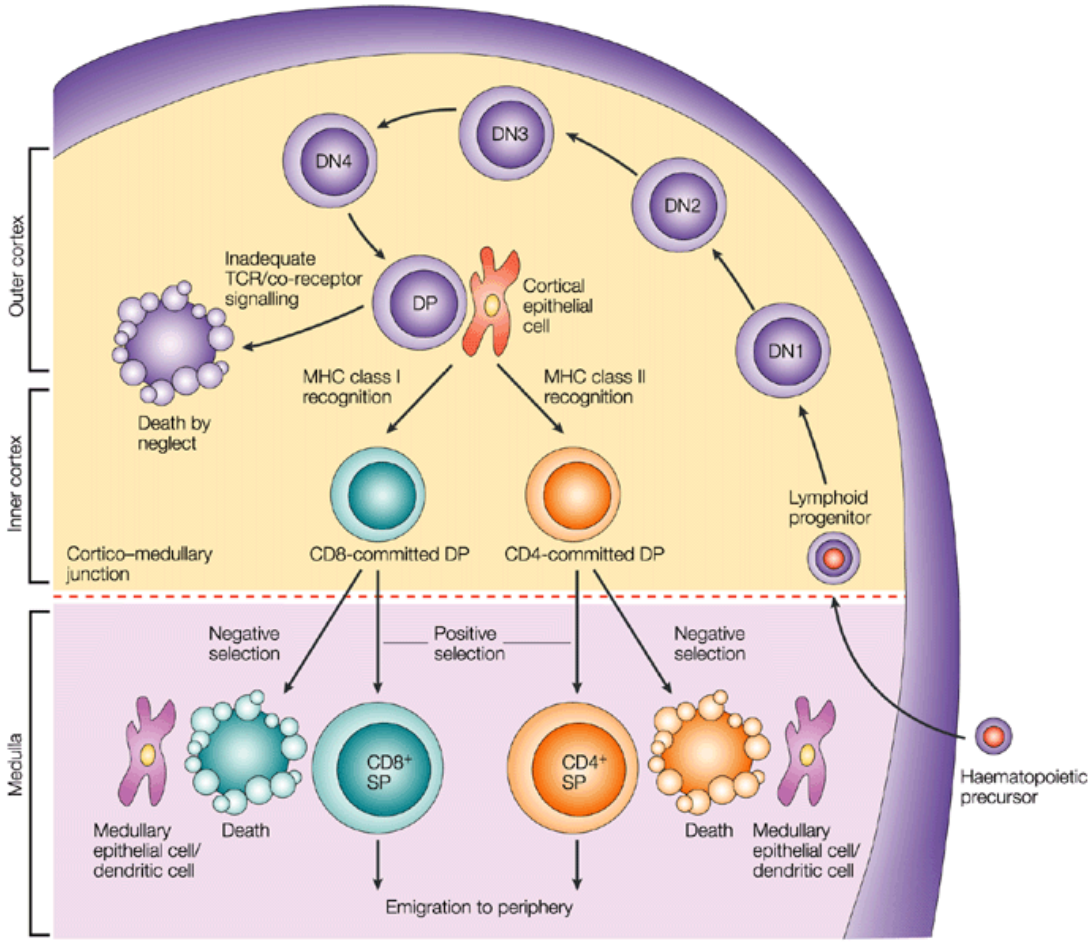

Figure 2: T cell developmental scheme in the thymus.
Dedicated lymphoid progenitors that emerge in the bone marrow relocate to the thymus where these cells do not express TCR, CD4, and CD8 (DN thymocytes). These cells can undergo four stages of differentiation (DN1, CD44+CD25-; DN2, CD44+CD25+; CD3, CD44-CD25+; and DN4, CD44-CD25-) (Godfrey et al., 2012). Cells that lack expression of CD44, but with CD25 (DN3) on their surface go through a β-selection process. The β chain further pairs with the pre - Tα and produce a pre-TCR forming a complex with CD3 molecules. This complex formation promotes the survival, proliferation, and arrest in further β chain loci rearrangement and differentiation steps later by expression of CD4 and CD8 on their surface (DP: double-positive cells). These DP cells undergo TCR-α-chain loci rearrangement and give rise to αβ-TCR. In the cortex, these cells undergo positive or negative selection (Klein et al., 2014). After selection process, down-regulation of co-receptor generates either naive CD4 or CD8 positive cells that leave the thymus and circulate in the periphery. (Germain, 2002a)

1.3 Composition of cytotoxic granules

CTLs consist of two types of killer cells called $CD8^+$ and Natural Killer (NK) cells, which fight against invading virus-infected or cancerous cells. Two major pathways of killing target cells were described. One of the mechanisms of CTL killing is to invoke a strong stimulus to activate caspase by the protease granzyme B. T cell recognition and binding to target cell leads to exocytosis of cytotoxic granules. In addition to many pro-apoptotic proteins, these organelles are very complex and consist of other proteins found in lysosomes (Podack and Kupfer, 1991).

Proteins responsible for target cell destruction are present in the dense core of CGs. These include mainly Perforin (pore-forming protein or cytolysin), calreticulin, granzymes (serine proteases: Gzm A, B, C, D, E, F, G, H, J, and M) associated with proteoglycans rich in chondroitin sulfate, granulysin and cathepsins. Except for calreticulin, other proteins are expressed only in activated CTL and NK cells (Burkhardt et al., 1990).

Contents of the dense core	Function
Perforin	Pore formation on the target cell membrane
Granzymes	Serine proteases: pre-directed cleavage at specific amino acids
Granulysin	Microbial agent
Calreticulin	Binding to calcium and Perforin proteins
Chondroitin sulfate proteoglycans	Complexes to granzymes
Cathepsin D and L	Proteases
Dipeptidylpeptidase I	Activation of granzymes from pre-pro to active forms
Mannose 6-phosphate receptor	Granule acidification, protein trafficking (granzymes)
Arylsulfatase	Hydrolyse sulfates in the body
β-Hexosamidase	Ganglioside metabolism
β-Glucuronidase	Hydrolysis of β-D-glucuronic acid residues
LAMP1 (lysosomal associated membrane protein 1)	Ligand for selectins, mediates cell-cell adhesion
LAMP2 (lysosomal associated membrane protein 2)	Maintaining integrity, pH and catabolism

Modified from (Smyth et al., 2001).

1.4 Immunological Synapse

The organization of membrane proteins which occurs at the interface between the killer T cells and the Antigen Presenting Cells (APCs) during the contacts or effector phase is called the Immunological Synapse (IS) (Grakoui et al., 1999). This energy-dependent synapse formation leads to polarization of the T cell which involves cytoskeletal rearrangement (movement of the microtubule organizing center (MTOC) from the cells' rear end to the synapse). The molecular interactions which regulate the immune response occur in a 15 nm gap between T cells and target cells or APCs (Garcia et al., 2010). Proteins such as dynein and kinesin-1 directly regulate the directed movement of CGs towards the IS. Immunofluorescence microscopy and reconstitution methods based on fluid supported lipid bilayer approaches helped tremendously to understand IS formation in live T cells (Monks et al., 1998). The mature IS is best studied between T helper cells (T_h cells) and their conjugated APCs and consists of three clusters with central TCR-MHC (T Cell Receptor-Major Histocompatibility Complex) interaction cluster surrounded by a LFA-1-TCAM-1 adhesion molecule ring and a distal ring that consists of transmembrane tyrosine phosphatase CD45 termed cSMAC (central

supramolecular activation clusters), pSMAC (peripheral supramolecular activation clusters) and dSMAC (distal supramolecular activation clusters) respectively (Johnson et al., 2000).

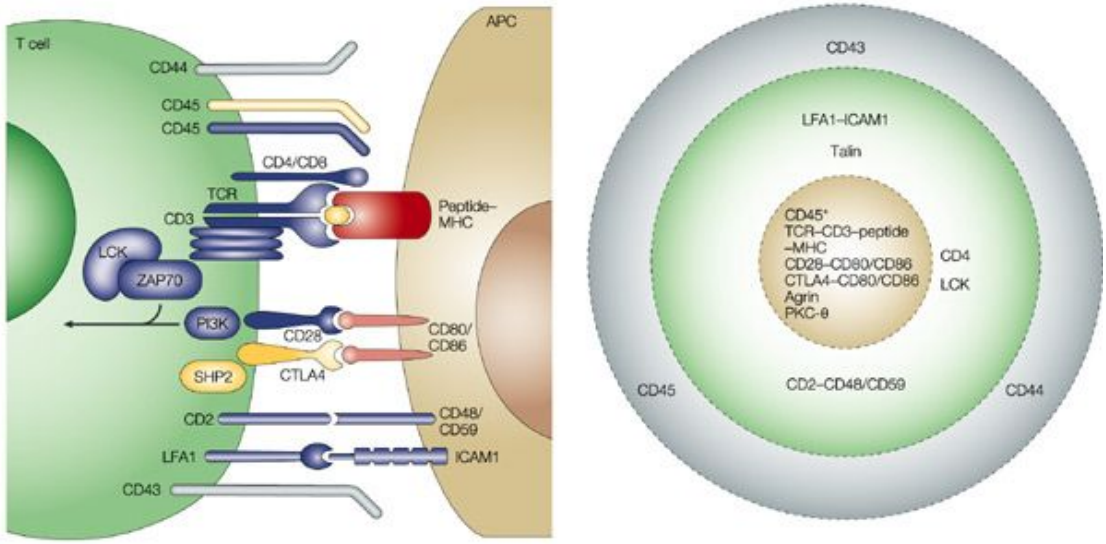

Figure 3: Formation of Immunological Synapse (IS).
(A) A side view showing a selection of important ligand pairs and signaling molecules involved in T-cell recognition. The stimulatory peptide-MHC molecules (red), activating or co-stimulatory molecules (blue), inhibitory molecules (yellow) and grey depict the molecules that are not involved in the signaling pathway. The inwardly directed arrow indicates converging signals that divert to activation of T-cell. (B) A face-on view of the IS indicating the characteristic 'bulls-eye' zone pattern that involves cSMAC (yellow), pSMAC (green) and dSMAC (grey) regions and also including molecules/ligand pairs during the IS formation (Huppa and Davis, 2003).

Finally, In the last phase of synapse maturation, vesicle-associated membrane protein 8 (VAMP8) mediates recycling endosomal fusion at the plasma membrane to deliver important components of fusion machinery such as factors involved in priming, proteins that mediate docking and soluble N-ethyl-maleimide-sensitive attachment protein receptor (SNAREs) (components of fusion machinery), responsible for CG exocytosis (de Saint Basile et al., 2010; Marshall et al., 2015b).

1.5 Vesicular Fusion

The delivery of the molecules to their precise intracellular destinations without compromising the structural integrity of cellular compartments is achieved by transport vesicles budding from one donor organelle that further target, dock, and fuse with another acceptor organelle (Chen and Scheller, 2001). In the nervous system, fusion with the plasma membrane to release vesicular content into the synaptic cleft is a highly coordinated calcium-dependent process (Lledo et al., 1998). Before fusion, a vesicle is transported to its target membrane and docked or tethered there. It further undergoes many priming events to prepare its release (Klenchin and Martin, 2000) (Pfeffer, 1999). Ca^{2+} regulates many vesicle trafficking

and directional fusion events (Heidelberger et al., 1994). The cellular fusion machinery overcomes the repulsive ionic forces and dissipates the hydration between two lipid bilayers with the help of SNARE proteins (Toei et al., 2010).

The SNARE superfamily of proteins has been implicated as primary players of membrane fusion in most of the intracellular membrane trafficking events. Syntaxin1 (Bennett et al., 1992) and VAMP1 (Baumert et al., 1989) were the first membrane fusion proteins discovered. SNAREs have been classified as R-SNARES (arginine-containing) or Q-SNARES (glutamine-containing) based on the presence of highly conserved amino acid residues (Toei et al., 2010) (Fasshauer et al., 1998). SNAREs vary widely in size and structure but contain SNARE motifs consisting of conserved 60-70 amino acid (aa) heptad repeat sequences called coiled-coil domains in their membrane-proximal regions. More than 100 SNARE proteins have been categorized into syntaxin, VAMP or SNAP-25 families where many of them have specified cellular localization indicating their particular functional involvement in specific intracellular trafficking.

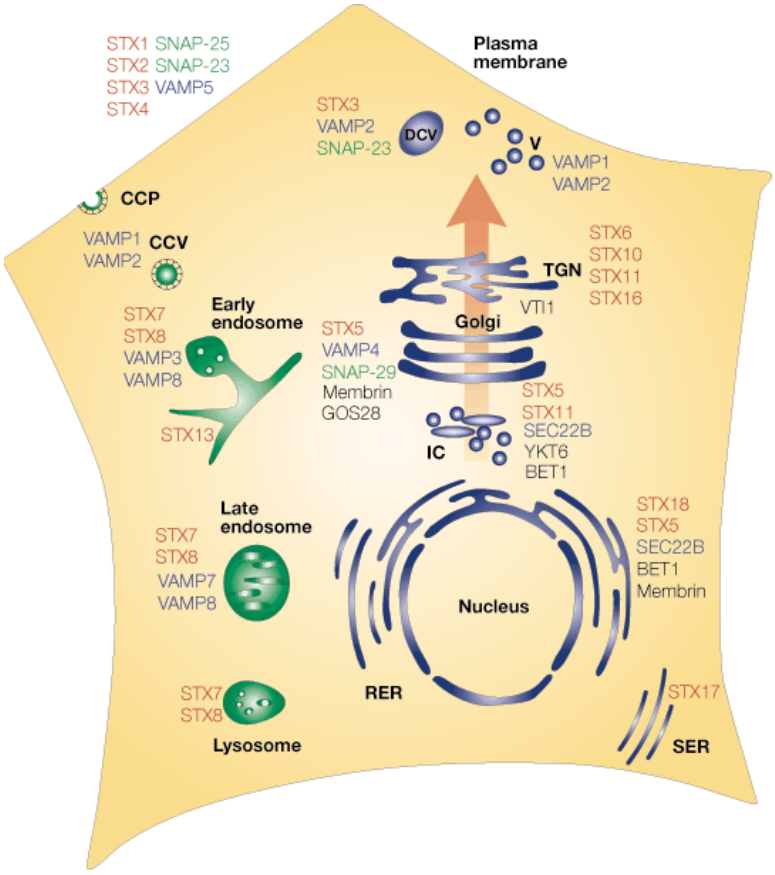

Figure 4: Mammalian SNAREs and their subcellular localization.
Specific compartmental localization of mammalian SNAREs shown (red, syntaxin family; blue, VAMP family; green, SNAP-25 family; black, others) (Chen and Scheller, 2001).

1.6 pH regulation in CGs

Using DMAP (3-(2,4-dinitroanilino)-3'-amino-N-methyldipropyl-amine) as a pH probe, cytotoxic granules from OE4 ($CD8^+$ T cell clone) cells have been found to be

acidic (pH 5.5 ± 0.2) and the pH increases to 6.8 ± 0.2 upon concanamycin A (CMA) treatment. Immunoelectron microscopy observations of these CMA treated cells revealed significant changes in the morphology of the CGs and reduced CG number (Kataoka et al., 1996). CMA induced a pH shift in CTLs with decreased levels of Perforin due to dissociation of Perforin from proteoglycans in a calcium-dependent manner. Thus, proteoglycans play an important role in sustaining the integrity of Perforin within the CGs for efficient target cell killing. Perforin in its free form is degraded by the serine proteases associated with it, to ensure the directional killing of the target cells while avoiding killing of bystander cells (Kataoka et al., 1997). Taken together, acidic pH plays a pivotal role in preserving lytic machinery of CGs and function of CTLs.

1.7 V-ATPase

Vacuolar-type H^+-ATPase (V-ATPase) is a multi-subunit membrane protein complex, highly conserved across different species with exceptional functions in many eukaryotes (Toei et al., 2010). V-ATPases acidify a wide range of intracellular organelles such as endosomes, lysosomes, phagosomes, autophagosomes, elements of Golgi apparatus (Forgac, 2007b). V-ATPases are also localized at the plasma membrane of osteoclasts to acidity the extracellular space between the cells and bone for resorption of bone material (Sun-Wada and Wada, 2013).

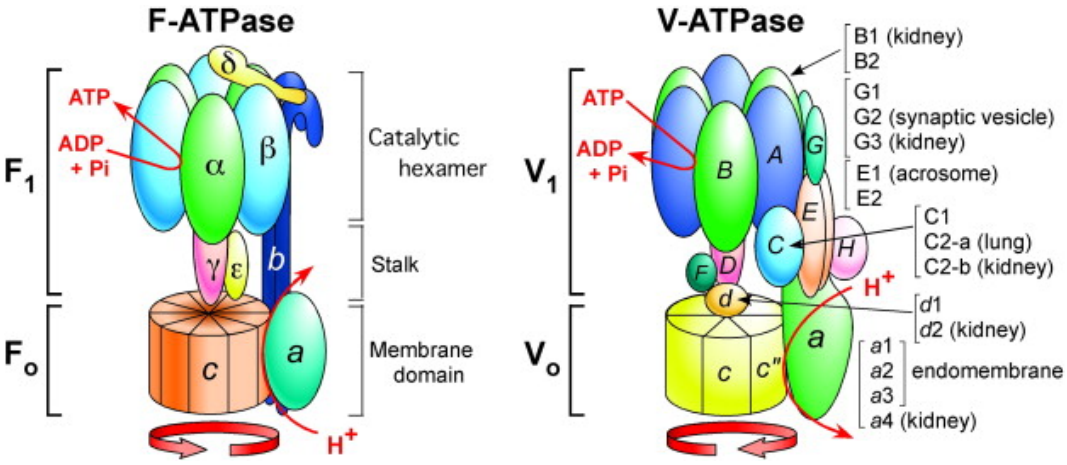

Figure 5: V-ATPase schematic.
Schematic representations of *E.coli*-F-ATPase (left) and mammalian-V-ATPase (right) with membrane specific F_1 and V_1 domains, catalytic hexamers ($\alpha_3\beta_3$ and A_3B_3), stalks and membrane sectors (F_0 and V_0) are depicted. Red arrow denotes the direction of the chemical reaction, rotation of subunits and transport of protons in physiological contexts. Various isoforms of V-ATPase are displayed with their specific localization and some with ubiquitous expression are not indicated. (Nakanishi-Matsui et al., 2010).

1.8 V-ATPase structure

V-ATPase is composed of 14 subunits that are organized into two domains called V_1 and V_0. Subunits (A-H) in the V_1 domain are involved in ATP hydrolysis whereas the V0 domain utilizing a rotary mechanism to pump protons across cell membranes carries out proton transport Qin et al., 2012). The central stack of the V-ATPase is made up of D, F and d subunits that are rotated from the energy generated by ATP hydrolysis within the V_1 domain. Every protonated glutamic acid residue that is situated on each subunit of the proteolipid ring comes in contact with an 'a'-subunit hemichannel at the luminal side. Due to the stabilization of the deprotonated glutamic acid by a crucial arginine residue from subunit 'a', the proton is released into the lumen (Forgac, 2007b) (Cotter et al., 2015). It has been shown that subunit 'H' regulates the V-ATPase activity by reversibly dissociating the V_1 and V_0 domains (Diab et al., 2009). The specific V-ATPase inhibitors identified to date such as bafilomycin and CMA bind to the proteolipid ring of the V_0 domain. These drugs inhibit by intercalating into the proteolipid ring of V_0 domain and prevent the helical swiveling required for the transport of protons (Toei et al., 2011) (Cotter et al., 2015). Mammalian V_0 domain of V-ATPase is more complicated than the V_0 of F-ATPase in structure and subunits. The 'a' subunit in mammalian V-ATPase consists of four isoforms (a1, a2, a3 and a4). The presence of a particular 'a' isoform determines the specific localization of V-ATPase or determines the specific organelle localization in different cell types (Figure 6) (Toyomura et al., 2000). a1-isoform is mainly targeted to synaptic vesicles and from there it could be transported to the presynaptic plasma membrane (Morel et al., 2003). In humans, a2-isoform is involved in Golgi function and also in the development of congenital disorders of glycosylation (Kornak et al., 2008) (Marshansky and Futai, 2008). The a3-isoform is mainly expressed in osteoclasts and its mutation leads to 50 % of osteopetrosis cases in humans (a lethal disease with defective bone resorption). a3-isoform is also important for insulin secretion from β-cells of pancreatic islets (Sun-Wada et al., 2006). The a4-isoform is predominantly expressed in the kidney, where it is targeted to the apical plasma membrane of collecting duct and epididymal clear cells (Pietrement et al., 2006) (Marshansky and Futai, 2008).

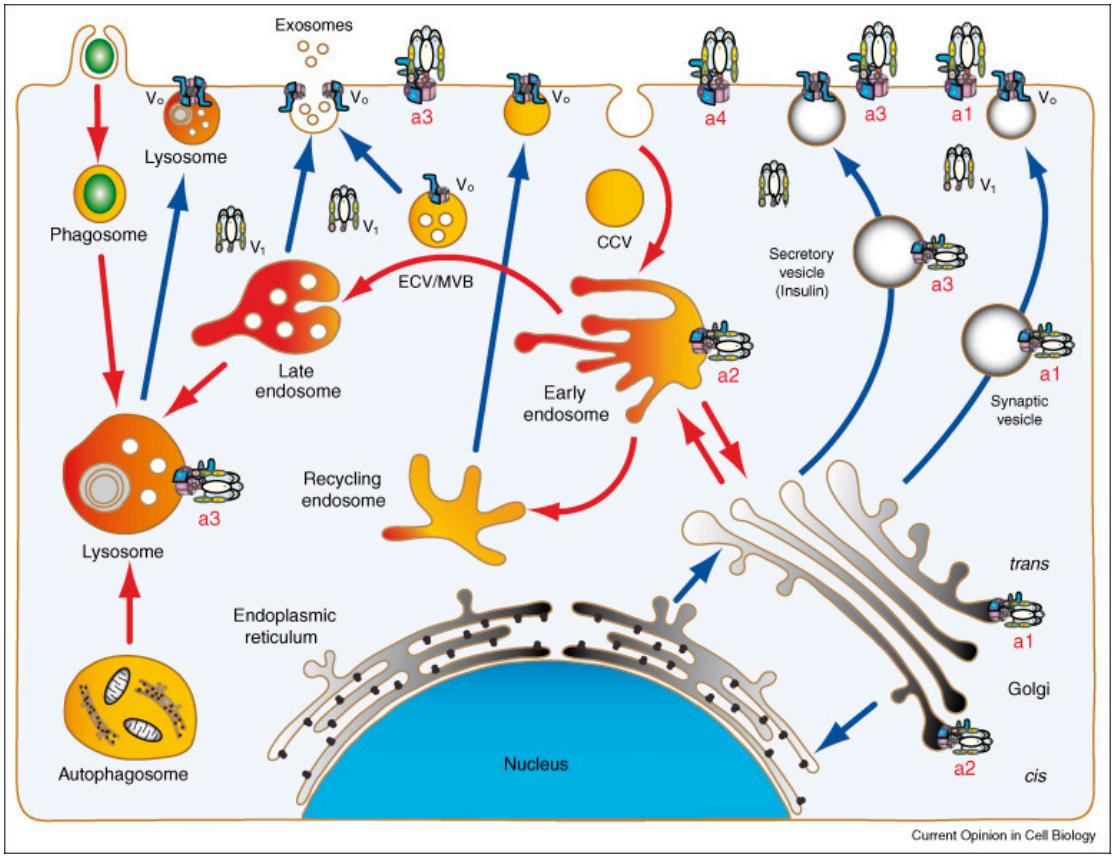

Figure 6: **Schematic showing of distinctive targeting of the 'a' subunit isoforms and vesicular trafficking of eukaryotic V-ATPases.**
The above scheme displays the compartments of endo (yellow/red) and exocytic (grey) pathways. Red and blue arrows indicate vesicular trafficking steps for endo- and exocytosis respectively. Four a-subunit isoforms being targeting to specific subcellular locations were shown. (Marshansky and Futai, 2008)

1.9 V-ATPase in membrane fusion

Vesicular trafficking is an important process required for inter-organelle communication in eukaryotes. This involves tightly regulated steps such as budding of vesicles from one donor compartment to fusion with an acceptor compartment or membrane (Marshansky and Futai, 2008). In addition to the role of V-ATPase in acidification, its direct involvement in budding and fusion of vesicle has been reported. For yeast vacuole biogenesis, the direct involvement of c-subunit of V_0 sector has been reported (Baars et al., 2007). In contrast to vesicle fusion, vacuole fission and fragmentation in vivo also depend on the proton pumping action of V-ATPase. In *Drosophila melanogaster,* the a1-subunit isoform is responsible for fusion of synaptic vesicles, and also interacts with calcium-binding messenger protein calmodulin at fly synapses. Similarly, in *Caenorhabditis elegans,* the secretion of Hedgehog related proteins from exosomes to the apical membrane is mediated by a1-subunit of V-ATPase (Marshansky and Futai, 2008) (Liegeois et al., 2006). Specifically, observations from (Klemmer et al., 2009) and (Di Giovanni et al., 2010b) provided evidence of specific V0 subunit (c-subunit) interaction with

membrane trafficking machinery such as synaptophysin, synaptobrevin2, and Rab7 in various cell types. These data corroborate the function of V-ATPase in membrane fusion.

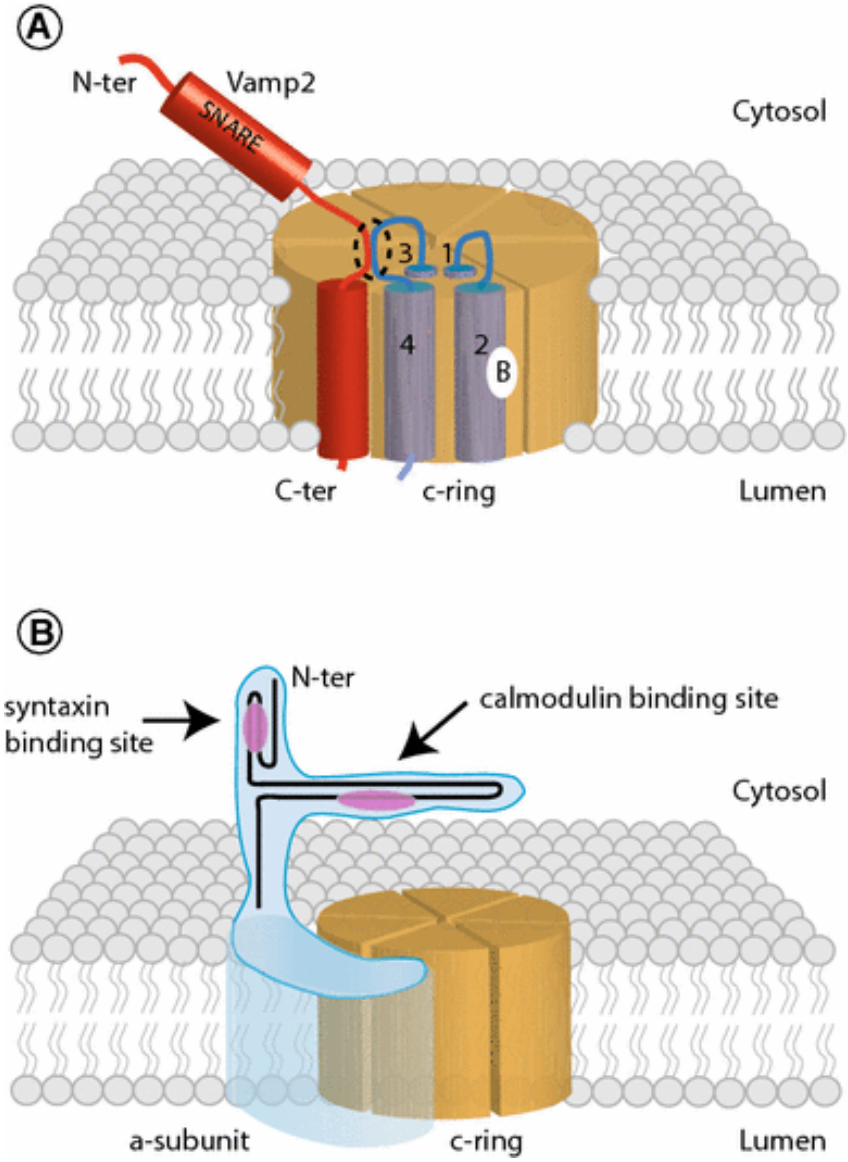

Figure 7: Model showing the V0 interaction with Syb2 and Ca^{2+}/calmodulin.
(A) The four transmembrane domains of c-subunit are depicted (numbered 1-4). Syb2 binding site has been mapped in the loop region of c-subunit between 3 and 4 transmembrane domains (broken circle). This domain also has been shown to interact with Ca^{2+}/calmodulin. (B) Bafilomycin A, syntaxin-1, and Ca^{2+}/calmodulin binding sites were shown (Morel and Poea-Guyon, 2015).

1.10 Infantile malignant osteopetrosis

In humans, mutations in the a3-subunit isoform (TCIRG1: 116-kD protein) are responsible for most of the cases with a severe form of infantile malignant osteopetrosis (rare autosomal recessive disease; MIM 259700) generally within the first 10 years of life. In affected individuals, the osteoclasts are present in normal or increased numbers with the only defect in the functional capacity of mature osteoclasts (Gerritsen et al., 1994). Some other cases showed defects in both

osteoclast differentiation and function (Marks et al., 1985) (Kong et al., 1999; Lazner et al., 1999; Marks et al., 1985). More than 120 mutations have been described in TCIRG1 gene including missense mutations, stop mutations, deletions or insertions, splicing defects, and large genomic deletions leading to autosomal recessive (ARO) cohort (detailed in the table from (Palagano et al., 2018)). Currently, the only established and reliable cure for ARO is hematopoietic stem cell transplantation (HSCT) allowing the restoration of bone resorption from donor-derived cells. The genetic heterogeneity of osteopetrosis disease sets out a challenge for molecular diagnosis.

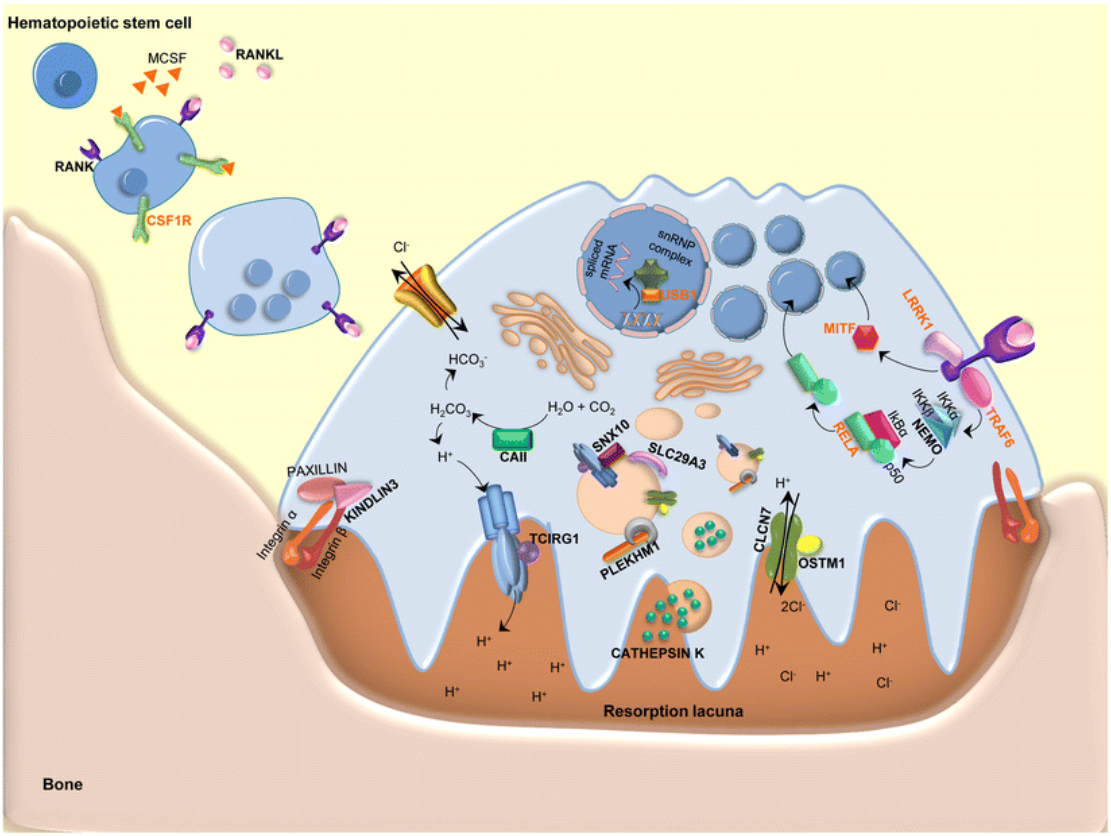

Figure 8: Representation of molecular players in pathogenesis of osteopetrosis.
The well-known disease causing genes are showed in black (bold) and newly identified are showed in orange (bold) (Palagano et al., 2018).

Recent studies on osteoclasts from a3-knockout mice showed that a3-subunit directly recruit specific co-factors including small GTPases Rab7a and Rab27a (in GDP-bound forms) and play an important role in the trafficking of lysosomes to the cell periphery for bone resorption, which is abrogated in a3-knockout mice. But a3-knockout (KO) did not affect the early endosomal and Golgi localization in osteoclasts (Matsumoto et al., 2018).

1.11 Longin-SNARE proteins

There are three subfamilies of longin SNAREs identified. They are Ykt6, VAMP7, and Sec22b. In addition to the coiled-coil domain that induces fusion, VAMP proteins from the longin-SNARE family consist of a long N-terminal domain, which aids in membrane fusion by regulating the assembly of trans-SNARE complex (Filippini et al., 2001). The N-terminal regions of longin SNAREs consist of α-β-α sandwich architecture in contrast to an autonomously folded three-helix bundle in Habc domain of syntaxins. Genetic analysis showed that alternative splicing of the human VAMP7 gene can give rise to an isoform lacking a SNARE coiled-coil domain. This eventually leads to different tissue expression pattern and subcellular localization with unknown function (Vacca et al., 2011) (Daste et al., 2015).

Longin domain of VAMP7 has an auto-inhibitory role on neurite outgrowth upon overexpression whereas its deletion has the opposite effect, indicating an additional function as 'on/off' switch for - fusogenic activity in addition to their regulatory function in localization of SNAREs to their site of action. Similarly, deletion of the longin domain showed increased spontaneous Ca^{2+}-independent fusion of synaptic vesicles that contain VAMP7 (Hua et al., 2011). Further, the auto-inhibitory role of VAMP7 was confirmed by NMR data that disclosed the adaptation of a closed conformation of VAMP7 in solution with the help of 126-160 aa residues from the SNARE coiled-coil domain. The aa leucine (43^{rd}) and tyrosine (45^{th}) on the longin domain were shown to be critical for longin domain interaction with the coiled-coil domain. In particular, mutation of tyrosine to glutamate modifies the protein structure from the closed to an open conformation (similar to the effect of tyrosine phosphorylation). This results in increased SNARE complex formation and also VAMP7-mediated vesicle exocytosis *in-vivo*. Surprisingly, VAMP7, in its closed conformation, still interacts with Varp (GDP-GTP exchange factor (GEF) for Rab21) and stabilizes its interaction with t-SNARE partner SNAP25 (to a lower extent compared to VAMP7 without a longin domain) (Vivona et al., 2010a) (Burgo et al., 2013). Further, VAMP7 longin domain can directly interact with coat components of clathrin-coated vesicles (δ-adaptin subunit AP3D1 of adaptor protein 3 complexes; AP-3) targeting VAMP7 to synaptic vesicles as well as to late-endosome and lysosomal compartments. Another crucial interacting partner of VAMP7 longin domain is HIV Rev-binding protein (Hrb). This interaction is responsible for the efficient retrieval of VAMP7 from the plasma membrane during endocytosis (Chaineau et al., 2008a). These findings suggest two important regulatory functions of the VAMP7 longin domain controlling SNARE complex formation and ensuring precise intracellular localization of VAMP7 through specific interactions with other proteins (Varp, AP-3, and Hrb) (Daste et al., 2015).

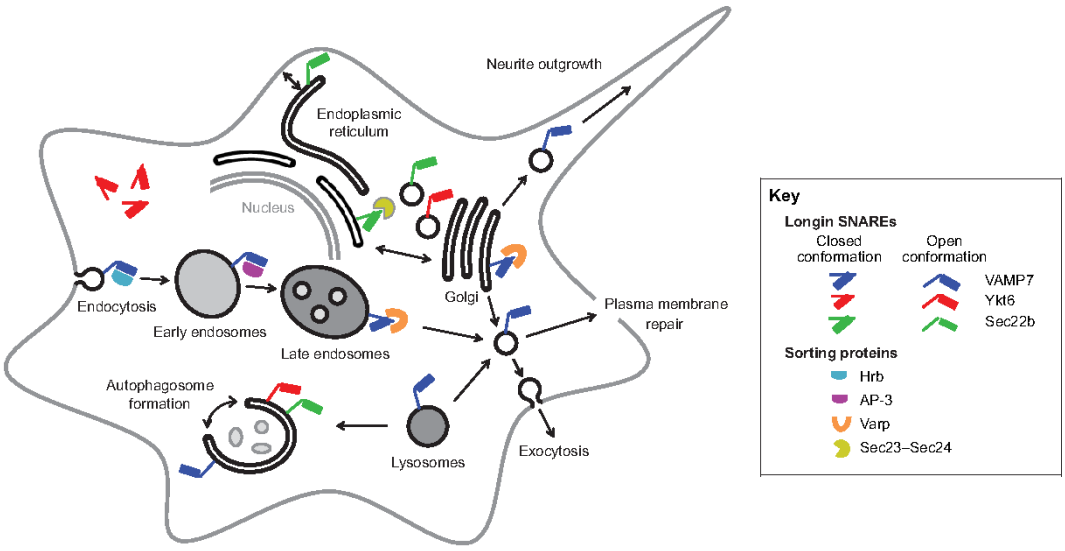

Figure 9: Main functions of longin SNAREs (overview)
Various functions of longin SNAREs Tkt6 (red), Sec22b (green) and VAMP7 (blue) (Daste et al., 2015b).

1.12 Vesicle associated membrane protein (VAMP7)

VAMP7 is derived from the Synaptobrevin-like 1 (SYBL-1) gene that is located in the pseudoautosomal region at the termini of the long arm of the X chromosome (Chaineau et al., 2009). It is ubiquitously expressed and conserved in eukaryotes (plants and flies to rat, mice, primates and humans) (DEsposito et al., 1996). Due to epigenetic mechanisms, SYBL-1 is transcriptionally inactive on the Y chromosome (Matarazzo et al., 2002). The SYBL-1 gene encodes a 2576 bp cDNA and generates a 220 aa containing protein with 25 kDa molecular weight. VAMP7 (also known as tetanus neurotoxin-insensitive VAMP; TI-VAMP) differs in only 12 aa from VAMP2 (Galli et al., 1998). It is an R-SNARE that is involved in important cellular functions including mitosis, cell migration, phagocytosis, membrane repair, and growth. It accomplishes these functions mainly by mediating the fusion of Golgi, late endosome and lysosomal compartment derived vesicles with the plasma membrane (Rossi et al., 2004) (Chaineau et al., 2009a). VAMP7 mediates fusion of transport vesicles and delivers lipids, adhesion proteins and growth factors for neurite outgrowth during neuronal development in PC12 cells (Martinez-Arca et al., 2000). In granulocytes (eosinophils and neutrophils) VAMP7 has been identified as a major SNARE involved in secretion of stored mediators from crystalloid and azurophilic granules by using antibody-mediated inhibition studies (Logan et al., 2006a). In YT-Indy (an NK-cell line) (Marcet-Palacios et al., 2008a) and NK-cells (Krzewski et al., 2011b), siRNA mediated silencing of VAMP7 resulted in defective exocytic release of granzyme B and reduced target cell killing. In allergic and non-allergic inflammatory disorders, mediator release from mast cells (MC) is a critical step. Human MC express VAMP3, VAMP7, VAMP8 and low levels of VAMP2. Using specific neutralizing antibodies against the cytoplasmic

NH2-terminal region and antibodies against SNAP-23, SNARE interactions between SNAP-23, STX-4, VAMP7 or VAMP8 were blocked resulting in a striking reduction in histamine release mediated by high-affinity IgE receptor (Sander et al., 2008b). In platelets, immunoprecipitation experiments revealed that VAMP7 associates with VPS9-domain ankyrin repeat protein (VARP) and Arp2/3, linking exocytosis of granules and actin reorganization (Koseoglu et al., 2015). To investigate the role of VAMP7 in vivo, (Sato et al., 2011) generated VAMP7 knockout (KO) mice and showed that the KO mice were almost identical compared to control, displaying similar epithelial cell polarity and lysosomal exocytosis. However, neurite outgrowth in cultured hippocampal neurons was reduced in KO mice.

Interestingly, in mouse primary CD4+ T cells VAMP7 is involved in the recruitment of a vesicular pool of Lat (linker for activation of T cells) to TCR-activation sites and in phosphorylation of the vesicular pool of Lat (Larghi et al., 2013b). However, this Lat recruitment was independent of tetanus neurotoxin-sensitive SNARE proteins such as VAMP1, VAMP2 and VAMP3. This defective recruitment of Lat to the TCR activation sites leads to defective T cell signaling during antigenic stimulation of T cells.

In B-lymphocytes, VAMP7 is associated with LAMP1 containing lysosomes, which are recruited and docked at the center of the B-cell IS. A decrease in VAMP7 expression on lysosomes does not change lysosomal transport to the synaptic interface but affects their local exocytosis which leads to the inability of B-cells to extract, process and presents immobilized antigens (Obino et al., 2017).

1.13 Genetic defects affecting cytotoxicity of lymphocytes

Many factors affect the complex coordinated series of steps in CTL activation such as biogenesis, polarization and exocytosis of CGs and lastly many players involved in efficient killing of target cells (Lieberman, 2003) (Stinchcombe et al., 2004) (Stinchcombe et al., 2006). Mutations in SH2DIA gene (encoding the SLAM-associated protein (SAP)) that is expressed in T and NK cells leads to fulminant infectious mononucleosis that is associated with X-linked proliferative syndrome (XLP) (Latour and Veillette, 2004). Mutations in the gene encoding β subunit of the adaptor protein AP3 (involved in lysosomal protein sorting from early endosomes) has been linked to Hermansky Pudlak Syndrome type II (HPS II) (Clark et al., 2003). CTLs isolated from HPS II patients show defective polarization of CGs to the IS. Another disorder known as Griscelli Syndrome type II (GS II) is characterized by mutations in Rab27a gene. Rab27a is a small GTP-binding protein that interacts with effectors to enable tethering of CGs to the IS (Menasche et al., 2000). Familial hemophagocytic lymphohistiocytosis (FHLH3) is a disorder caused by mutations in UNC13D, a gene encoding Munc13-4. FHLH3 is

characterized by early-onset HLH and defective priming of CGs leading to reduced cytotoxicity of T cells (Feldmann et al., 2003). In human CD8+ T cells, syntaxin11 (Stx11) acts as a t-SNARE for the fusion of CGs at the IS (Halimani et al., 2014). Patients suffering from mutations in Stx11 gene (cause of FHL4) show many clinical symptoms such as hepatosplenomegaly, hypercytokinemia, neurological alterations, hyperactivation of polyclonal $CD8^+$ T cells and macrophages (Bryceson et al., 2007). Perforin deficiency leads to a FHL2 disorder characterized by the defective entry of protease granzyme B into the target cells leading to inefficient target cell killing (Voskoboinik et al., 2005). Perforin deficiency accounts for 30-40 % of the total FHL incidence. Mutations in MUNC18-2 and lysosomal trafficking regulator protein (LYST) genes cause FHL5 (Cote et al., 2009) and Chediak-Higashi syndrome (characterized by abnormal granule size) respectively (Nagle et al., 1996). In summary, the altered function of SNAREs and SNARE associated proteins lead to severe defects in lymphocyte function both in humans and mice.

1.14 Aim of the work

The killing capacity of CTLs depends upon the efficient fusion and release of cytotoxic materials at the IS. The proton gradient generated by V-ATPase is used by an antiporter to fill synaptic vesicles with neurotransmitters. Empty vesicles are fused due to the loss of acidification in synaptic vesicles. Loss of a1-subunit in *Drosophila melanogaster* leads to complete loss of neurotransmission. Chromophore assisted photoinactivation of the a1-subunit in chromaffin cells and in primary rat neuronal culture leads to disruption of secretion (Poea-Guyon et al., 2013). Works from many groups indicate that the V-ATPase membrane sector is a missing link between acidification and exocytosis.

In this study, we aim to understand the role of V-ATPase a3-subunit in CTL function. We hypothesize that a3-subunit plays an important role in acidification of CGs and subsequently aids in fusion of CGs by interacting with the v-SNARE (Syb2). Alternatively, the a3-subunit might play a role in the trafficking of CGs to the IS by recruiting Rab proteins which in turn interacts with kinesin motor proteins that transport the vesicles along the microtubules. Further, we aim to investigate the role of a3-subunit in the biogenesis and maturation of CGs. We extended our studies to investigate the molecular machinery underlying CTL-mediated target cell killing in primary human $CD8^+$ T cells.

The immunological synapse shares a similar structural pattern with neuronal synapses by forming an interface between an activated T cell and an antigen-presenting cell or target cell. In the neuronal synapse, signaling molecules called neurotransmitters are released by the axon terminal of a presynaptic neuron and bind to and react with the receptors on the dendrites of the postsynaptic neuron.

Whereas, at the immune synapse cytotoxic granules containing cytotoxic substance fuse at the IS resulting in death of the target cells. In both the synapses (neuronal and immune), the fusion of transport vesicles is mediated by SNAREs. Coordinated interplay between many proteins are necessary from the recognition of target cells by CTLs to the formation of a functional IS, which end with target cell apoptosis or death involves many complex processes that include intracellular interactions, directional trafficking of CGs towards the IS and final fusion. Mutations in many of these genes lead to severe immune reactions such as FHL. The identification of cognate SNARE partners and modulators required for CG trafficking and fusion at the IS is important to understand the molecular mechanisms underlying CTL-mediated target cell killing in humans.

In this study, we aim to understand the role of VAMP7 in cytotoxic granule trafficking to the IS and their final fusion. Importance of VAMP7 in the exocytosis of CGs was shown in NK cell lines. However, its precise mechanistic role in the fusion of CGs in primary human $CD8^+$ T cells is enigmatic. CTLs display defective polarization of CGs towards the IS and reduced target cell killing upon VAMP7 silencing. Here, we aim to discover functional role of VAMP7 in primary human $CD8^+$ T cells.

2. Materials

2.1 Materials

2.1.1 Reagents

Chemical substance	Company (cat/order number)
Agar-Agar	Roth (5210.3)
Ammonium persulphate	Bio-Rad (1610700)
BSA	Sigma-Aldrich (A4503)
Bromophenol blue	Roth (A512.1)
β-Mercaptoethanol	Roth (4227.3)
Chloroform	Sigma-Aldrich (288306)
Carbonyl cyanide 3-chlorophenylhydrazone (CCCP)	Sigma-Aldrich (C2759)
cOmplete mini, EDTA-free Protease Inhibitor Cocktail tablets	Roche (11836170001)
Dithiothreitol	Sigma-Aldrich (10197777001)
D-Biotin	IBA Lifesciences (2-1016-002)
Dodecylsulphate Na-salt in pellets (SDS)	Roth (2326.2)
Dimethyl sulfoxide (DMSO)	Sigma-Aldrich (D8418)
dNTP-Mix	Fermentas (R0192)
D-PBS (1X)	Thermo Fisher Scientific (14190-094)
Ethanol (100%)	Roth (5054.1)
Ethidium bromide	Roth (2218.2)
Ethylenediamine tetraacetic acid disodium salt (EDTA)	Sigma-Aldrich (E6635)
Glucose	Merck (1.08342.1000)
Glycerol	Sigma-Aldrich (G5516)
Glutamax	Thermo Fisher Scientific (35050061)
Heat inactivated Bovine Serum (FBS)	Gibco (10500)
HEPES	Thermo Fisher Scientific (15630080)
Hybond N^+ nylon membrane	GE Healthcare (RPN119B)
Deoxyribonucleic acid from herring sperm	Merck (D3159)
HPLC water	Thermo Fisher Scientific (11307090)
Hydrochloric acid	Merck (9057.1000)
Isopropanol	Roth (AE73.1)
Ionomycin calcium salt	Merck (407952)
Kanamycin	Sigma-Aldrich (K-1377)
KCl	Merck (1049360500)
L-Glutamine 200 mM (100X)	Gibco (25030-024)
Methanol (100%)	Roth (HN41.1)
NaCl	Merck (1064040500)
N, N, N', N'- Tetramethyl ethylenediamine (TEMED)	Merck (1107320100)
NuPAGE LDS sample buffer 4X	Thermo Fisher Scientific (NP0007)
NuPAGE MES SDS Running Buffer 20x	Thermo Fisher Scientific (NP0002)
NuPAGE Transfer Buffer 20x	Thermo Fisher Scientific (NP00061)

L-Glutamine 200 mM (100X)	Gibco (25030-024)
Methanol (100%)	Roth (HN41.1)
NaCl	Merck (1064040500)
N, N, N', N'- Tetramethyl ethylenediamine (TEMED)	Merck (1107320100)
NuPAGE LDS sample buffer 4X	Thermo Fisher Scientific (NP0007)
NuPAGE MES SDS Running Buffer 20x	Thermo Fisher Scientific (NP0002)
NuPAGE Transfer Buffer 20x	Thermo Fisher Scientific (NP00061)
Penicillin/streptomycin	Gibco (15140122)
Paraformaldehyde	Merck (1040051000)
Phusion High-Fidelity DNA polymerase	Thermo Fisher Scientific (F530L)
Poly-L-ornithine	Sigma-Aldrich (P4957)
pfu-Polymerase	Fermentas (EP0501)
Ponceau S solution 0,1%	Sigma-Aldrich (P7170)
PAGE ruler Prestained Protein Ladder	Thermo Fisher Scientific (26616)
Restore Western Blot Stripping Reagent	Thermo Fisher Scientific (21059)
Roti Nanoquant 5x	Roth (K880)
Rotiphorese Gel 40 (37, 5:1)	Roth (T802.1)
Spectra Multicolor Broad Range Ladder	Thermo Fisher Scientific (26634)
Super Signal West Dura Extended	Thermo Fisher Scientific (34075)
Super Signal West Pico Chemiluminiscent Substrate	Thermo Fisher Scientific (34076)
Strep-Tactin XT Superflow 50% suspension	IBA Lifesciences (2-4010-002)
20 % Sarcosyl	Sigma-Aldrich (L7414)
Tryptone/Peptone	Roth (8952.3)
Trypan blue solution	Sigma-Aldrich (93595)
Triton X-100	Sigma-Aldrich (T8787)
Tris-hydrochloride	Roth (9090.3)
Tween 20	Roth (2727.1)
Water	Sigma-Aldrich (W4502)

2.1.2 Commercial Kits

Kits	**Company (cat/order number)**
EndoFree Plasmid Maxi Kit	Qiagen (12362)
QIAquick PCR Purification Kit	Qiagen (28106)
Plasmid Midi Kit	Qiagen (10023)
Plasmid Mini Kit	Qiagen (27106)
QIAquick Gel Extraction Kit	Qiagen (28706)
Nucleofection kit for mouse T cells	Lonza (VVPA-1006)
P3 Primary Cell 4D- Nuclofector X Kit L	Lonza (V4XP-3024)
Dynabeads™ FlowComp™ Mouse CD8 Kit	Thermo Fisher Scientific (11462D)
Dynabeads™ Untouched™ Mouse CD8 Cells Kit	Thermo Fisher Scientific (11417D)
Dynabeads™ Untouched™ Human CD8 Cells Kit	Thermo Fisher Scientific (11348D)
Dynabeads™ FlowComp™ Human CD8 Kit	Thermo Fisher Scientific (11362D)
Dynabeads™ Mouse T-Activator CD3/CD28	Thermo Fisher Scientific (11453D)

Dynabeads™ Human T-Activator CD3/CD28	Thermo Fisher Scientific (111.32D)
NuPAGE™ 10% Bis-Tris Protein Gels, 1.0 mm, 10-well	Thermo Fisher Scientific (NP0301BOX)
NuPAGE™ 10% Bis-Tris Protein Gels, 1.5 mm, 10-well	Thermo Fisher Scientific (NP0315BOX)
NuPAGE™ 12% Bis-Tris Protein Gels, 1.0 mm, 10-well	Thermo Fisher Scientific (NP0341BOX)
NuPAGE™ 4-12% Bis-Tris Protein Gels, 1.0 mm, 10-well	Thermo Fisher Scientific (NP0321BOX)

2.1.3 Antibodies

Antibodies	Species	Dilution	Company (cat/order number)
Primary antibodies			
anti-alphatubulin	rabbit	ICC 1:500	Abcam (4074)
Alexa Fluor488 anti-CD107a (LAMP-1, clone 1D4B)	mouse	FACS 1:400	Biolegend (121607)
Human anti-CD3ε (B-B11)	mouse	30µg/ml	Diaclone (854.010.000)
Mouse anti-CD3ε (clone145-2C11)	hamster	30µg/ml	BD Pharmingen (553057)
anti-Tcirg1 (a3 subunit)	rabbit	ICC 1:200	Thomas Jentsch (Leibniz-Institut fur Molekulare Pharmakologie, Berlin, germny)
anti-FLAG TAG	rabbit	WB 1:5000	Cell Signaling (2368)
anti-granzyme B	mouse	WB 1:3000	Cell Signaling (4275S)
Alexa Fluor 647 anti-human Perforin (DG9)	rabbit	ICC 1:200	BioLegend (308109)
anti-Perforin 1	mouse	WB 1:1000	Santa Cruz (136994)
Alexa Fluor 647 anti-granzyme B (GB11)	rabbit	ICC 1:200	BioLegend (515405)
anti-GAPDH (clone 14C10)	rabbit	WB 1:5000	Sigma Aldrich, (2118L)
anti-LAT	rabbit	ICC 1:500 WB 1:1000	Merck (06-807)
anti-Phospho-p44/42 MAPK (Erk1/2) (Thr202/Tyr204)	rabbit	WB 1:1000	Cell Signaling (9101)
anti-SNAP-23	rabbit	WB 1:2000	Synaptic Systems (111203)
anti-Syntaxin 11	rabbit	WB 1:2000	Synaptic Systems (110113)
anti-Tcirg1 (a3 subunit)	rabbit	WB 1:2000	ProSci (6973)
anti-VAMP7	rabbit	WB 1:2000	Novus Biologicals (NBP2-32232)
anti-VAMP2 (D6O1A)	rabbit	WB 1:2000	Cell Signaling (13508)
Secondary antibodies			
Alexa 488 conjugated anti-rabbit IgG	goat	1:2000	Thermo Fisher Scientific (A27034)
Alexa 568 conjugated anti-rabbit IgG	goat	1:2000	Thermo Fisher Scientific (A-11011)
Alexa 488 conjugated anti-mouse IgG	goat	1:2000	Thermo Fisher Scientific (A28175)
HRP-conjugated anti-mouse IgG	goat	1:1000	Thermo Fisher Scientific (31430)
HRP-conjugated anti-rabbit IgG	goat	1:10,000	Thermo Fisher Scientific (31460)
HRP conjugated anti-Strep-tagII	rabbit	1:10,000	IBA Lifesciences (2-1509-001)

2.1.4 Media for cell culture and solutions

Media (Company (cat/order number))	Supplements
IMDM (GIBCO) (21980-032)	10% FCS, 50µM 2-Mercaptoethanol, 0.5% Pen/Strep
RPMI (GIBCO) (21875-034)	10% FCS, 50µM 2-Mercaptoethanol, 0.5% Pen/Strep, 10mM HEPES
AIM V (for mouse primary $CD8^+$ T cells) (GIBCO) (12055-091)	10% FCS, 50µM 2-Mercaptoethanol
AIM V (for human primary $CD8^+$ T cells) (GIBCO) (12055-091)	10% FCS
Erythrocyte lysis buffer (pH: 7.3)	H_2O, 100 ml, NH_4Cl, 0.829 g, (155 mM), $KHCO_3$, 0.1 g, (10 mM), EDTA from 50 mM stock-260 µl, pH 7.4 (0.1 mM) (Bzeih, H 2016)
Isolation Buffer	PBS, 500 ml, BSA 0.5 g, (0.1%), EDTA from 0.5 M stock solution, 2 ml, (2 mM) (Bzeih, H 2016)
Extracellular buffer for TIRF measurements: 0 mM calcium buffer	155 mM NaCl, 4.5 mM KCl, 5 mM HEPES, 3 mM $MgCl_2$, (pH: 7.4 and Osmolarity: 300-310 mOsm) (Bzeih, H 2016)
10 mM calcium buffer	140 mM NaCl, 4.5 mM KCl, 5 mM HEPES, 2 mM $MgCl_2$, 10 mM $CaCl_2$ (Bzeih, H 2016)
Solutions for immunocytochemistry	
Fixation	4% PFA in 1X D-PBS
Permeabilization	0.1% triton-X100 in D-PBS
Blocking	0.1% triton-X100 in D-PBS+ 2% BSA
Solutions for western blot	
Lysis buffer	50 mM Tris-HCl (pH 7.5), 150 mM NaCl, 250 uM PMSF, 1% Triton-X100, 1 mM Deoxyclolate, 1 mM EDTA, 1 mM DTT and 1 protease inhibitor tablet (Roche), and H_2O
Lysis buffer for Twin-Strep-tag pulldowns	300 mM NaCl, 0.5 % NP-40 or Triton X-100 50 mM, 50 mM Tris-HCl (pH-7.5), 1 protease inhibitor tablet (Roche) and H_2O
TBS (10X)	87.7 g NaCl, 24 g Tris-Cl (pH 7.5) and H_2O up to 1 L
1X TBST (0.1%) (1L)	10x TBS-100 ml, Tween 20-1 ml and H_20 up to 1 L

2.1.5 Mounting medium

Mounting medium was prepared by dissolving 6 g Glycerol, 2.4 g Mowiol 4-88 in 6 ml H_2O and stirred for 2 h at room temperature and 12 ml of 0.2 M Tris-HCl buffer (pH 8.5) was added and stirred at 53 °C overnight. The solution was centrifuged at 1700g for 20 min at room temperature and aliquoted the clear supernatant and stored at -20 °C.

2.2 Methods

2.2.1 Primary CD8$^+$ lymphocytes isolation

Mouse CD8$^+$ T cells

C57BL/6 wild type (WT), homozygous Synaptobrevin2-mRFP knock-in (Sybki), granzyme B-TFP Knock-in, mice were used for experiments. Spleens from 8-30 weeks old mice were taken out and gently crushed through a 70µm cell-strainer (Corning Life Sciences). RPMI medium was used to collect and mix the splenocytes which were spun down without a break (in a centrifuge). Splenocytes were incubated with erythrocyte lysis buffer for 30 s to remove erythrocytes. Cells were immediately washed with isolation buffer and CD8$^+$ T cells were isolated using Dynabeads FlowComp Mouse CD8 Kit (Thermo Fisher Scientific) according to the user manual. Briefly: the CD8$^+$ T cells were positively isolated from splenocytes by incubating 5x10^7 cells with 25 µl of anti-CD8 antibody for 10 min on ice followed by washing with isolation buffer. Later, 75 µl of CD8 antibody-coated Dynabeads were added to the cells and mixed gently on the rocker at 4° C. Finally, cells were detached from Dynabeads using releasing buffer followed by an isolation buffer. CD8$^+$ T cells were then collected and resuspended in AIM V culture medium supplemented with 10% FCS with 50 µM 2-Mercaptoethanol.

Human CD8$^+$ T cells

Human peripheral blood mononuclear cells (PBMCs) were isolated from healthy donors by density gradient centrifugation (Lymphoprep; Axis-Shield). Isolated PBMCs were stimulated with SEA (5 µg/ml) at a density of 108 cells/ml at 37°C for 1 h. The stimulated PBMCs were resuspended at a density of 1.5 × 10^6 cells/ml in complete medium (AIMV medium; Thermo Fisher Scientific) supplemented with 10% FCS (Thermo Fisher Scientific) and 100 U/ml of recombinant human IL-2 (Biosource). After 5 days, SEA-specific CTLs were positively isolated by using a Dynal CD8$^+$ isolation kit (Thermo Fisher Scientific) and cultured further in complete medium. For some experiments, CTLs from day 1-2 after positive isolation were used. For some experiments, CD8$^+$ T cells were isolated from PBMCs by negative magnetic selection (CD8$^+$ negative isolation kit; Thermo Fisher Scientific) and further activated with CD3/CD28 beads (Chitirala et al., 2019).

2.2.2 Activation of naive cells

Mouse CD8$^+$ T cells

The isolated naive CD8$^+$ T cells were cultured for 3 days at a density of 1x10^6 cells/mL in AIM V medium at 37°C with 5% CO_2 in 24-well plate with additional anti-CD3/CD28 activator beads (1:0.8 ratio) and 100 U/ml recombinant IL-2 to generate effector CTLs (Bzeih, H 2016). Cells were split after every 2 or 3 days in culture by adding fresh AIM V medium supplemented with 100 U/mL IL-2 (Thermo Fisher

Scientific). All experiments were performed using the cells from day 2 to day 15 in culture.

Human CD8$^+$ T cells

The isolated naive CD8$^+$ T cells were cultured for 2 days at a density of 1.5x10^6 cells/mL in AIM V complete medium at 37°C with 5% CO_2 in 6-well plate with additional anti-CD3/CD28 activator beads (1:0.8 ratio) to generate effector CTLs. All experiments were performed using the cells after 2 days of activation.

2.2.3 Electroporation

Mouse CD8$^+$ T cells

Mouse cells from day 2 to 15 were used according to the experiment and electroporated with a Lonza Mouse T cell Nucleofector Kit (Lonza). Briefly, cells (2-5 x 10^6 cells/transfection) were washed with warm isolation buffer once and resuspended in 100 µl of nucleofection solution supplied in the kit. Depending on the construct, 1-5 µg of plasmid DNA was used per transfection. Cells were mixed with DNA and then electroporated using an electroporation device (Lonza). After electroporation, cells were immediately transferred to mouse T cell nucleofector medium (Lonza). Depending on the experiment, cells were used after 8 to 16 h of transfection.

Human CD8$^+$ T cells

For human, CD8$^+$ T cells were used after 2 days of activation for transfection using P3 Primary Cell 4D-Nucleofector X Kit (Lonza). Briefly, (2-5 x 10^6 cells/transfection and 1-5 µg of plasmid DNA) were used and electroporated using a 4D electroporation device (Lonza). After electroporation cells were immediately transferred to AIM V complete medium. Depending on the experiment, cells were used after 8 to 16 h of transfection.

2.2.4 Target cell culture

RAJI (target cells for human CD8$^+$ T cells) and P815 (target cells for mouse CD8$^+$ T cells) cells were cultured in RPMI medium (Thermo Fisher Scientific) containing 10 % FCS and P/S antibiotics.

2.2.5 Plasmids

Mouse CD8$^+$ T cells

The pH and chloride sensor ClopHensorN was purchased from Addgene (50758). ClopHensorN was cloned in pMAX vector by digesting the pCDNA3-ClopHensorN plasmid with HindIII and blunted the DNA with DNA polymerase 1, large (Klenow) fragment followed by digestion with NotI. The same was performed for pMAX vector and both vector and insert were ligated. ClopHensorN (Q69M) construct

was generated by mutating glutamine at the 69th position in E^{2}GFP to methionine by using forward primers 5'-ATG TAT ACT AGC TAG CTG GAG CCA CCC GCA GTT C-3', 5'- ACG GCG TGA TGT GCT TCA-3' and reverse primers 5'- TGA AGC ACA TCA CGC CGT-3', 5'- ATG TAT ACG CGG ATC CGC GCT TGT ACA GCT CGT CCA T-3'. Citrine was amplified from D1ER (gift from Adolfo lab) using forward primer 5'- ATG TAT ACC GGA ATC CAT GGT GAG CAA GGG CGA G-3' and reverse primer 5'-ATG TAT ACG CGG ATC CTT ACT TGT ACA GCT CGT CCA T-3' and cloned in pMAX vector. GzmB-Citrine was cloned by replacing mCherry at the C-terminus of GzmB with forward primer 5'- ATG TAT ACG CGG ATC CAC CGG TCG CCA CCA TGG TGA GCA AGG GCG AG-3' and reverse primer 5'- ATG TAT AAA AGC GGC CGC TTA CTT GTA CAG CTC GTC-3'. Citrine-TdTomato was cloned by replacing E^{2}GFP from pMAX-ClopHensorN plasmid with TdTomato by using forward primer 5'- ATG TAT ACC GGA ATT CGG TGG GAG CGG CGG AAG CGG CGG TAA GCT TAT GGT GAG C-3'and reverse primer 5'-ATG TAT ACG CGG ATC CCT TGT ACA GCT CGT CCT T-3'. Citrine-TagRFP-T was cloned by amplifying TagRFP-T with forward primer 5'-ATG TAT ACG CAC CGG TAT GGT GTC TAA GGG CGA A-3' and reverse primer 5'- ATG TAT ACC GCT CGA GTT ACT TGT ACA GCT CGT C-3'. mt-ClopHensorN (Q69M) was cloned by amplifying mt signal sequence with forward primer 5'-ATG TAT ACG GGG TAC CGC CAC C ATG TCC GTC CTG ACG CCG-3' and reverse primer 5'-ATG TAT ACC GGA ATT CCC CCA ACG AAT GGA TCT T-3'.

Human CD8$^+$ T cells

Human VAMP3, VAMP4, VAMP7, and VAMP8 constructs that were used in this study were purchased from Addgene (42310, 42313, 42316 and 42311). VAMP7 coding sequence was amplified from pEGFP-VAMP7 plasmid (42316; Addgene) with forward primer 5′-ATA TAC GGG GTA CCG CCG CCA CCA TGG CGA TTC TTT TTG CT-3′ and reverse primer 5′ ATA TAC CGG AAT TCT TTC TTC ACA CAG CTT GG-3′ and inserted in frame with C-terminal mCherry with forward primer 5'- ATA TAC CCA AGC TTA TGG TGA GCA AGG GCG AG-3' and reverse primer 5'- ATA TAC GCG GAT CCT TAC TTG TAC AGC TCG TCC AT-3' or inserted in frame with pHuji with forward primer 5'-ATG TAT ACC CAA GCT TAT GGT GAG CAA GGG CGA G-3' and reverse primer 5'-ATG TAT ACG CGG ATC CTT ACT TGT ACA GCT CGT C-3' in pMAX containing GGSGGSGGS linker. Similarly, human VAMP8-mCherry, GzmB-mCherry, GzmB-mTFP, and msVAMP2-mRFP constructs which have been used for colocalization analysis (Chitirala et al., 2019) and TIRF experiments were previously described (Marshall et al., 2015; Matti et al., 2013a).

2.2.6 Semi-quantitative PCR

The total RNA from primary cells was extracted with TRIzol (Thermo Fisher Scientific) and reverse transcribed (SuperScript II; Thermo Fisher Scientific) using random hexamer primers. Semi-quantitative PCR was performed using specific primers as shown below. Data were normalized to GAPDH.

Mouse $CD8^+$ T cells

Primer name	Sequence (5' to 3')
a1 Forward primer	TCA GTA CCT GAG GAA GAA GC
a1 Reverse primer	CTG GTG GAC CAT GGT GTC GC
a2 Forward primer	CGA GAA GTG ACG TGT GAG GA
a2 Reverse primer	ACT GAA CTT GGA GGA GAG CA
a3 Forward primer	CGA ACC ACC TGA GCT TTC TC
a3 Reverse primer	CCC ATG GAA GAG CAG ATG AT
a4 Forward primer	GCA GTG CAT CAT TGC CGA GAT
a4 Reverse primer	GAA CAT AGG CTG GAC ACT CCA AG
GAPDH Forward primer	ACC ACA GTC CAT GCC ATC AC
GAPDH Reverse primer	TCC ACC ACC CTG TTG CTG TA

Human $CD8^+$ T cells

Primer name	Sequence (5' to 3')
VAMP4 Forward primer	CCT TCG AAG TTG TTT GGA TC
VAMP4 Reverse primer	GGA CCA AGA TTT GGA CCT AG
GAPDH Forward primer	ACC ACA GTC CAT GCC ATC AC
GAPDH Reverse primer	TCC ACC ACC CTG TTG CTG TA

2.2.7 PCR protocol

Component	50 µl reaction	Final concentration
H_2O	35.5 µl	
5X Phusion HF Buffer	10 µl	1X
10 mM dNTPs	1 µl	200 µM each
Forward primer	1 µl	0.5 µM
Reverse primer	1 µl	0.5 µM
Template DNA	1 µl	50-100 ng
Phusion DNA Polymerase	0.5 µl	0.02 U/µl

Cycle step	Temperature	Time	Cycles
Initial Denaturation	98 °C	30 s	1
Denaturation	98 °C	30 s	35
Annealing	60 °C	30 s	
Extension	72 °C	15-30 s/kb	
Final Extension	72 °C	10 min	1
End	4 °C	∞	

2.2.8 Western blot analysis

After activation, transfection or siRNA treatment, cells were homogenized with a syringe or yellow tip in lysis buffer (50 mM Tris (pH 7.4), 1 mM EDTA, 1% Triton X-100, 150 mM NaCl, 1 mM DTT, 1 mM deoxycholate, protease inhibitors, and PhosSTOP (Roche) on ice. Lysates were rotated on a rocker for 10 min at 4°C, and insoluble material was removed by centrifugation at 10-13,000 RPM. Further,

Quick Start Bradford 1x Dye Reagent (5000205; Bio-Rad) was used to determine the protein concentration. Samples were boiled with 1X loading buffer (Thermo Fischer Scientific) at 98°C for 10-15 min. Later, proteins were separated by SDS-PAGE (NuPAGE; Thermo Fisher Scientific), transferred to nitrocellulose membranes (Amersham), and blocked by incubation with 5% skim milk powder in 1X TBS with 0.1% Tween-20 for 1-2 h and blotted with specific antibodies. Blots were developed using enhanced chemiluminescence reagents (SuperSignal West Dura Chemoluminescent Substrate; Thermo Fisher Scientific). For densitometry analysis, the pixel area and mean fluorescence intensity (MFI) were determined with ImageJ v1.46 (http://imagej.nih.gov/ij, National Institute of Health) (Chitirala et al., 2019).

2.2.9 siRNAs

siRNAs were purchased from QIAGEN.

Mouse CD8$^+$ T cells

siRNA	**Sequence (5' to 3')**	**(cat/order number)**
Control siRNA	UUC UCC GAA CGU GUC ACG UTT	1022076
a1 siRNA	AAG GUC AUU UAC AAU UUG CUA	SI00907249
a2 siRNA	CUG GGU AGA AUU UCA GAA CAA	SI00907270
a3 siRNA1	CAU GCU CAC CCU GAA CCC UAA	SI05141577
a3 siRNA2	CUG GCC AUG GUC CUC ACU UGA A	SI05141570

Human CD8$^+$ T cells

siRNA	**Sequence (5' to 3')**	**(cat/order number)**
Control siRNA	UUC UCC GAA CGU GUC ACG UTT	1022076
VAMP7 siRNA1	GAU UGG AAU UAU UGA UUG ATT	SI04376134
VAMP7 siRNA2	GGG CAA UCG UGU CGC UAA UTT	SI04212453
VAMP4 siRNA1	AGA UUG CUG CAU AAU UUA ATT	SI03019653

2.2.10 Conjugation of T cell with target cells

Mouse CD8$^+$ T cells

To conjugate mouse primary CTLs with P815 target cells, CTLs were mixed with target cells at a ratio of 10:1 or 20:1 and plated onto poly-L-ornithine coated or CD3ε coated glass coverslips and incubated at 37°C for 15 min. Later, cells were fixed with ice-cold 4% PFA in Dulbecco's 1xPBS (Thermo Fisher Scientific) and stained with respective antibodies.

Human CD8$^+$ T cells

The stimulation of Raji cells was performed in 96-well plates with a maximum of one million cells resuspended in 100 µl AIM V medium. Human primary CTLs were mixed with target cells at a 10:1 ratio and plated on poly-L-ornithine coated or CD3ε coated 12 mm or 25 mm glass coverslips and incubated at 37°C for indicated time points (5, 10 and 15 min) respectively. Cells were fixed with ice-cold 4% PFA in

Dulbecco's 1XPBS (Thermo Fisher Scientific) and stained with respective antibodies.

2.2.11 Structured Illumination Microscopy (SIM)

The SIM setup was a Zeiss Elyra PS1 Zeiss, Oberkochen). We acquired images with a 63x Plan-Apochromat (NA 1.4) with laser excitation at 488, 561, and 635 nm for respective fluorophores and then processed to obtain higher resolution images without background using Zen software (Zen 2012; Carl Zeiss). For co-localization analysis, Pearson's and Manders' overlap coefficients were determined using the JACoP plugin of ImageJ v1.46.

2.2.12 Total internal reflection fluorescence (TIRF) microscopy

Mouse $CD8^+$ T cells

CTLs isolated from granzyme B-mTFP knock-in mice were electroporated with either ns-siRNA or siRNA1 or 2 against the a3 subunit. For some experiments, CTLs were electroporated with a GzmB-mCherry construct. After 12-16 h of transfection, 0.2-0.3 x 10^6 cells were resuspended in 30 µl of extracellular buffer solution (2 mM HEPES, 140 mM NaCl, 4.5 mM KCl, and 2 mM $MgCl_2$) containing no Ca^{2+} and allowed to settle for 1-2 min on anti-CD3ε antibody (30 µg/ml) coated coverslips. Cells were then perfused with extracellular buffer containing 10 mM Ca^{2+} to trigger cytotoxic granule exocytosis. Depending on the constructs used and the experimental conditions, cells were imaged for 7 min at room temperature either 561 nm or 488 nm. Unless specified otherwise, acquisition frequency was 10 Hz and the exposure time was 100 ms (Chitirala et al., 2019).

Human $CD8^+$ T cells

The TIRFM setup from Visitron Systems GmbH (Puchheim, Germany) was custom built based on an IX83 (Olympus) equipped with the Olympus autofocus module, a UAPON100XOTIRF NA 1.49 objective (Olympus), a 488 nm 100 mW laser and a solid-state 100 mW laser emitting at 561 nm, the iLAS2 illumination control system (Roper Scientific SAS, France), the evolve-EM 515 camera (Photometrics) and a filter cube containing Semrock (Rochester, NY, USA) FF444/520/590/Di01 dichroic and FF01-465/537/623 emission filter. Visiview software was used to control the setup (Version: 4.0.0.11, Visitron GmbH). CTLs from different donors were electroporated with the indicated plasmids to image fusion in TIRFM. For some experiments, CTLs were electroporated with GzmB-mCherry or VAMP7-mCherry or VAMP7-pHuji or rab11-mCherry plasmids. After 12-16 h of transfection, 0.2-0.3 ×10^6 cells were harvested and resuspended in 30 µl of extracellular buffer (2 mM HEPES, 140 mM NaCl, 4.5 mM KCl, and 2 mM $MgCl_2$) containing no Ca^{2+} and allowed to settle for 1-2 min on anti-CD3ε antibody (30 µg/ml) coated coverslips. After 1 or 2 min the cells were perfused with extracellular

buffer containing 10 mM Ca^{2+} to induce cytotoxic granule exocytosis. Depending on the constructs and the experimental conditions, cells were imaged for 7 min at room temperature (RT = 22 ± 2°C) either at 561 nm or at 488 nm or alternating between both illuminations. Unless specified otherwise, the acquisition frequency was 10 Hz, and the exposure time was 100 ms. Images and time-lapse series for cytotoxic granule fusion were analyzed using Time Series Analyzer plugin (ImageJ (http://imagej.nih.gov/ij), or the FIJI package of ImageJ)) (Chitirala et al., 2019). A sudden rise in VAMP7-pHuji fluorescence or a sudden drop in VAMP7-mCherry, GzmB-mTFP, GzmB-mCherry or Rab11-mCherry fluorescence occurring within 300 ms (three acquisition frames) was defined as fusion (Ming et al., 2015).

2.2.13 Electron Microscopy

Mouse $CD8^+$ cells isolated from GzmB-mTFP knock-in mouse 5 days after activation by anti-CD3/anti-CD28 beads were treated with siRNA (details Praneeth). After 16 hours of transfection, 4000 CTLs in AIMV media with 30 % FCS were seeded onto Poly-L-ornithine (0.1 mg/ml) coated 1.4 nm sapphire discs in flat specimen carriers (Leica). The cells were allowed to settle for 20 min at 37° C with 5 % CO_2. Samples were vitrified in a high-pressure freezing system (Leica EM PACT2/RTS) in AIMV with 30 % FCS. All samples were further processed in an automatic freeze-substitution apparatus (Leica AFS2) as described in (Matti et al., 2013a). In brief, all samples were transferred into the precooled (-130°C) freeze-substitution chamber of the AFS2. The temperature was increased from -130 to -90° C for 2 h. Cryo-substitution was performed at -90°C to -70° C for 20 h in anhydrous acetone and -70° C to -60° C for 20 h with 0.3 % (w/v) uranyl acetate in anhydrous acetone. The samples were infiltrated with increasing concentrations (30, 60 and 100 % for 1 h each) of Lowicryl (3:1 K11M/HM20 mixture) with 0.3 % uranyl acetate. After 5 h of infiltration with 100 % Lowicryl, samples were UV polymerized at -60° C for 24 h and for an additional 15 h while the temperature was raised linearly to 5° C (Chang et al., 2018).

Ultrathin sections were cut using a Leica EM UC7 and collected on pioloform-coated copper grids after contrasting with uranyl acetate and lead citrate sections were analysed with a Tecnai12 Biotwin electron microscope (FEI).

2.2.14 Correlative fluorescence electron microscopy

Cells were prepared for high pressure freezing as described before, but samples were vitrified in a high high-pressure freezing system (Leica EM PACT2/RTS) 5 min after addition of CellMask deep red (Invitrogen, 1:2000) in AIMV for plasma membrane staining. In contrast to the described freeze-substitution protocol, the samples for correlative microscopy were infiltrated with increasing concentrations

(30, 60 and 100 % for1 h each) of Lowicryl (3:1 K11M/HM20 mixture) without 0.3 % uranyl acetate, to avoid background fluorescence during high resolution SIM. After freeze-substitution the samples were kept in the dark at 4° C until further processing. 100-120 nm ultrathin sections were cut by using an EM UC7 (Leica). The sections were collected on carbon-coated 200 mesh copper grids (Plano). Fluorescence analysis was performed within 1 d after sectioning to avoid loss of fluorescence signals.

For correlative fluorescence and electron microscopy, the grids were placed in a drop of water between two coverslips, sealed with silicone (picodent twinsil®). High-resolution SIM (ELYRA PS.1; Zeiss) images were acquired by using the 63x Plan-Apochromat (NA 1.4) with excitation light of 488 nm and 642 nm wavelengths and processed. After imaging in the bright-field mode for grid orientation, CellMask deep red image (642 nm) was recorded to identify both the image plane and the outline of CTLs by plasma membrane staining. In a z-stack analysis, 3-8 anti-RFP488 images (488 nm) and CellMask deep red images (642 nm) were recorded with a step size of 100 nm to scan the cells of interest. For data acquisition and image processing for higher resolution ZEN 2010 software (Carl Zeiss Microscopy GmbH) was used.

After fluorescence analysis, the very same grids were stained with 2% uranyl acetate and lead citrate and analysed with a Philips Tecnai12 Biotwin electron microscope (FEI). Only CTLs with well-conserved membranes, cell organelles and nuclei were analysed and used for correlation.

For correlation, the CellMask deep red image, which shows the labelled plasma membrane of the cells, was used to find the optimal overlay with the EM image. The final alignment with the anti-RFP488 image defines the position of the fluorescent signal within the cells of interest. Images were overlaid in Corel Draw (Chang et al., 2018).

2.2.15 Analysis of cytotoxic granule accumulation in the TIRF plane

ImageJ v1.46 software was used to determine the number of CGs that appeared at the TIRF plane. The background was subtracted from the raw data stacks and a threshold value was set for all cells to mark the CGs specifically. For every frame of the time-lapse movie, the value of the pixel defined as the threshold area was obtained from each cell. The ratio between the threshold area and the number of vesicles from three frames from every cell was calculated. To obtain the number of vesicles appearing in each frame, the area threshold was divided by the ratio from all the time frames. The average number of vesicles or CGs from the indicated number of cells were plotted against frames or time in seconds.

2.2.16 Calcein-AM killing assay

Raji cells were pulsed with SEA (1 µg/ml) for 30 min at 37°C and cells after washing with 1XPBS were loaded with calcein-AM (500 nM; Thermo Fisher Scientific) in serum-free AIMV media for 15 min at RT. Cells were washed with 1XPBS once and plated onto 96-well black plates with clear bottoms (BD Falcon). One well of the target cells was lysed with Triton X-100 (0.1%) to calculate maximum target cell lysis as control. CTLs were electroporated with ns-siRNA or siRNA1 or 2 against VAMP7. After 16-18 h, CTLs (0.2×10^6 cells/well) were added to target cells in 10:1 or 20:1 ratio to measure killing at 37°C for 4 h. Readings were measured at 485 nm excitation wavelength and 535 nm emission wavelength by GENios Pro plate reader. The fluorescence for the experimental conditions was adjusted by the parameter γ according to the live target cell control fluorescence. The γ value was measured at time zero by using the formula,

$$\gamma = F_{(live)\,(0)}/F_{(exp)\,(0)}$$

$F_{(live)}$ = fluorescence of target cells only

$F_{(exp)}$ = fluorescence of target cells + CTLs

The cytotoxicity was calculated from the loss of calcein fluorescence in target cells using the following equation,

$$\%\ \text{target cell lysis} = (F_{(live)} - \gamma \times F_{(exp)})/(F_{(live)} - F_{(lyse)}) \times 100\%.$$

$F_{(lyse)}$ = maximum target lysis

For details see (Kummerow et al., 2014). All experiments were performed in duplicates from 3-4 donors.

For mouse primary CTLs, p815 target cells were incubated with anti-CD3ε antibody (30 µg/ml) for 30 min and then the killing assay was carried out as described (Chitirala et al., 2019).

2.2.17 Estimation of ERK phosphorylation

1 x 10^6/ml primary human $CD8^+$ T cells were activated for the appropriate time with anti-CD3ε (125 ng/ml) and anti-CD28 (250 ng/ml) antibodies in a volume of 1 ml. Cells were washed in cold PBS and lysed in lysis buffer (50 mM Tris (pH 7.4), 1 mM EDTA, 1% Triton X-100, 150 mM NaCl, 1 mM DTT, 1 mM deoxycholate, protease inhibitors, and PhosSTOP; Roche) on ice. After sonication, proteins were separated by SDS-PAGE and were analyzed by Western blotting (Chitirala et al., 2019).

2.2.18 Twin-Strep-tag pulldown assay

20-50 x 10^6 of primary, human $CD8^+$ T cells were electroporated with either Twin-Strep-tag (used as control), VAMP7-Flag-Twin-Strep-tag or Twin-Strep-tag-Stx11 constructs and incubated at 32°C for 12-16 h. Cells were lysed with ice-cold lysis buffer (50 mM Tris (pH 7.4), 300 mM NaCl, 0.5% Triton X-100, protease inhibitor mix (Roche)) and centrifuged at 10-13,000 RPM for 10-15 min at 4°C. After protein quantification with Bradford reagent, 500 µg of cleared lysate was incubated with 125 µg Strep-Tactin-Sepharose beads (IBA Lifesciences) for 1.5-3 h at 4°C on a rotator. After incubation, beads were washed three times with lysis buffer at 2500 RPM. Proteins bound to the beads were eluted with 1x NuPAGE™ LDS sample buffer (Thermo Fisher Scientific) and heated at 98°C for 15 min for Western blot analysis. 50 µg (10%) of protein lysate was loaded as input (Chitirala et al., 2019).

2.2.19 pH and chloride calibration

A pH calibration curve was generated using the ratio of the fluorescence with illumination at 488 nm to that at 458 nm of the E^2GFP moiety of ClopHensorN (Q69M). The AIM-V media was removed and replaced with T cell-extracellular solution and the cells were located under the microscope. The extracellular solution was then replaced with a pH-clamping solution. Solutions with pH values of 4, 4.5, 5, 5.5, 6, 6.5, 7, 7.5, 8 and 8.5 were made as follows. The base solution consists of 30 mM NaCl, 100 mM KCl, 2 mM $MgCl_2$, and 10 mM glucose, as well as 10 µM nigericin, 4 µM valinomycin and 5 µM CCCP. Depending on the target pH, lactate (20 mM, pH4), MES (20 mM, pH5 and pH6), or HEPES (20 mM, pH7–9) were included. After allowing equilibration of the intracellular pH (>5 min), the images were acquired with sequential illumination at 488 nm, 458, and 561 nm with open pinhole. The whole-cell was considered for ratiometric calibration. Ratios of fluorescence vs pH values were fit using a sigmoidal curve (SigmaPlot 13). For pH measurements, the coverslips were placed in the observation chamber, filled with extracellular solution, and imaged at room temperature. Images were acquired at 488, 458, and 561 nm. Ratios of fluorescence at 488 and 458 nm were calculated and the pH was interpolated from the calibration curve fit. The desired $[Cl^-]_i$ and pH_i were controlled by equilibrating extra and intracellular ion concentrations using the nigericin (K^+/H^+ exchanger) (5 µM), the protonophore carbonyl cyanide p-chlorophenylhydrazone (CCCP) (5 µM), the valinomycin (K^+ ionophore) (5 µM) and tributyltinchloride (Cl^-/OH^- exchanger) (10 µM) in the presence of high-K^+ 20 mM HEPES buffer containing 0.6 mM $MgSO_4$, 38 mM sodium gluconate and 100 mM potassium gluconate. The specified amount of gluconate anion was replaced by Cl^-, and pH was adjusted with small aliquots of NaOH (Arosio et al., 2010).

2.2.20 Generation of granzyme B-mTFP knockin mice

Gzmb-mTFP KI mice were generated with the help of hCas9-D10A-mRNA (nickase) using a guide RNA 5'-GTCCAGGATTGCTCTAGGAC-3' (PAM = AGG). Stop codon in the 5th exon of granzyme B was removed and replaced with mTFP in frame with a flexible linker sequence GGSGGSGGS. A Homology Directed Repair (HDR) fragment was designed to introduce mTFP in the genome. To confirm the correct location of the HDR fragment, sense 5'-ATC AAA GAA CAG GAG AAG ACC CAG-3' (upstream HDR to mTFP) and sense 5'-ACC GCA TCG AGA TCC TGA ACC-3' primers were used. For PCR, sense wt primer 5'-CAA CAG CTC AGT GCC TTG TAT CCA-3' and sense KI primer 5'-ACC GCA TCG AGA TCC TGA ACC-3' and Antisense wt primer 5'-TTC ACA AGG ACC AGC TCT GT-3' were used. This work has been done by Fritz Benseler (in collaboration with Niels Brose, Max-Plank-Institut für Experimentelle Medizin, Göttingen). Heterozygous animals were transported to the animal facility in the Physiology department, Universitätsklinikum des Saarlandes, Homburg and mouse line was maintained as homozygous GzmB-mTFP (308).

2.2.21 Synaptobrevin2 knock-in mice generation

2.2.21.1 Cloning of Targeting vectors

pSP73-Synaptobrevin2-mRFP targeting vector (Matti et al., 2013a) was used as a background vector for cloning. Synaptobrevin2-mRFP was replaced with Synaptobrevin2-mTFP or TagRFP-T or pHluorin2. mTFP was amplified using NPY-mTFP vector as a template with forward primer 5'-ATG TAT ACG GGG TAC CAT GGT GAG CAA GGG CGA GGA G-3' and reverse primer 5'- ATG TAT ACC CAA GCT TTT GCG GCC GCT TAC TTG TAC AGC TCG TCC AT-3'. TagRFP-T was amplified using pCR259-TagRFP-T vector as a template with forward primer 5'- ATG TAT ACG GGG TAC CAT GGT GTC TAA GGG CGA AGA G-3' and reverse primer 5'- ATG TAT ACC CAA GCT TGA AGC GGC CGC CAG TGT GAT G-3'. pHluorin2 was synthesized using IDT custom gene synthesis tool from protein sequence (Mahon, 2011) which was codon optimized for Mus musculus.

2.2.21.2 Genomic DNA isolation from tail samples

Stock	For 5 ml
100 mM Tris-HCl, pH 8.5	500 µl
5 mM EDTA, pH 8.0	50 µl
200 mM NaCl	200 µl
0.2% (W/V) SDS	100 µl
20 µg/ml Proteinase K	5 µl/tube

1. Tail samples were lysed with 500 µl tail lysis buffer (with 5µl proteinase K)
2. Tubes were incubated overnight at 55 °C in heat block or oven.
3. After digestion samples were centrifuged at 13000 rpm for 10 min at 4 °C

4. Supernatant was transferred into another eppendorf (by tumbling or with blue 1ml tip which is cut)
5. 3 volumes of cold 100% ethanol was added to the tubes and inverted 5-6 times till you see the DNA precipitation
7. The precipitated DNA was transferred to another eppendorf, which has 1 ml 70% ethanol in it
8. Tubes were centrifuged at 13000 rpm for 10 min at 4 °C
9. Pellet was dried at RT for 30 min
10. 80-100µl of TE buffer was added and incubate at 37 °C for 3-4 h.
11. DNA was mixed by tapping and was run at 90V, 0.7% Agarose gel, 2X TAE

2.2.21.3 Genomic DNA isolation from Embryonic Stem (ES) cells

ES cell lysis buffer

Stock	Working	For 50 ml
1 M Tris-HCl, pH 7.5	10 mM Tris-HCl, pH7.5	0.5 ml
0.5 M EDTA, pH 8	10 mM EDTA	1 ml
5 M NaCl	10 mM NaCl	0.1 ml
20 % Sarcosyl	0.5 % Sarcosyl	1.75 ml
20 mg/ml Proteinase K	1 mg/ml Proteinase K	2.5 ml (added later)
Water	Water	46.65 ml

To isolate genomic DNA from one 96 well plate, 12 ml of lysis buffer was taken in a falcon tube and 600 µl of Proteinase K was added. Vortexed briefly and sarcosyl was added followed by short vortexing.
1. 96 well plate was thawed at RT for 10-15 min.
2. 100 µl of lysis buffer was added with multichannel pipette.
3. Plate was wrapped with parafilm and closed the lid.
4. Plate was kept in a box with wet paper towels inside and incubated 60 °C overnight.
5. Plate was centrifuged at 1500 rpm/2 min at RT and 50 µl was transferred to new plate.
6. 100 µl of pre-cooled (-20 °C) 100 % ethanol + NaCl (1.5 µl of 5 M NaCl per 100 µl ethanol).
7. Incubated at RT for 30 min (DNA precipitation was observed under the microscope).
8. Plate was centrifuged at 2500 rcf at 4 °C. Supernatant was discarded by tumbling the plate upside down.
9. Washed 2 times with 70 % ethanol and centrifuged at 2500 rcf at 4 °C. One plate was stored at 4 °C and another were dried for 30-45 min at RT.

Digestion:

Water	39 x 110 = 4290 µl

Buffer O	4.5 x 110 = 495 µl
Fermentas ASP718I enzyme	1.5 x 110 = 165 µl

Mixed well and added 45 µl to each well (no need to mix after adding). Plate was incubated at 37 °C / overnight in a shaker incubator (50 rpm) in a box with wet paper towels inside.

Boast up digestion:

Water	3.5 x 110 = 385 µl
Buffer O	0.5 x 110 = 55 µl
Fermentas ASP718I enzyme	1x 110 = 110 µl

Mixed well and added to each well and plate was incubated at 37 °C / 1-2 h in a shaker incubator (50 rpm) in a box with wet paper towels inside.

0.7 % Agarose gel:

5.6 gm of agarose was added in 800 ml of 2 x TAE buffer with EtBr and gel was made using a big caster.

Sample preparation:

6 µl of 6 x loading buffer was added to each well and loaded on the gel.

Transfer:

After running, the gel was washed 3 times with denaturation buffer at 35 rpm for 45 min (15 min each). Followed by rinsing with water and washed 3 times at 35 rpm for 45 min (15 min each) with neutralization buffer. DNA was transferred to Hybond N^+ nylon membrane for 36 to 48 h.

Buffers:

Denaturation buffer: (0.5 N KOH and 1.5 M NaCl) /1 L	500 ml 1 M KOH, 300 ml 5 M NaCl and 200 ml water
Neutralization buffer: (0.5 M Tris-HCl, pH 7.5 and 1.5 M NaCl) /1 L	500 ml 1 M TRIS-HCl, 300 ml 5 M NaCl and 200 ml water
20 X SSC buffer: 1L (pH 7)	3 M NaCl (175.3 g), 300 mM Tri-sodium-citrate-dihydrate (88.23 g),
Wash Buffer A: 1L	20 X SSC (100 ml), 10 % SDS (50 ml) and 850 ml water
Wash Buffer B: 1L	20 X SSC (10 ml), 10 % SDS (10 ml) and 980 ml water
Speed hybrid buffer: 1L	70 g SDS, 100 g PEG 6000 (calbiochem), 75 ml 20 X SSPE, 175.3 g NaCl + 27.6 g $NaH_2PO_4.H_2O$ + 7.4 g EDTA (pH adjusted to 7.4 and autoclaved)

Church buffer:

For 1L	Substance	Working	For 500 ml (in ml)	For 250 ml (in ml)	For 100 ml (in ml)
500 ml	Na-Phosphate Buffer (387 ml 1M	0.5 M	193.5 + 56.5	96.75 + 28.25	38.7 + 11.3

	Na_2HPO_4 + 113 ml 1M NaH_2PO_4				
350 ml	20%SDS	7 %	175	87.5	35
110 ml	10%BSA	1 %	55	27.5	11
2 ml	0.5M EDTA	1 mM	1	0.5	0.25
10 ml	Salmon Sperm DNA (10mg/ml)(Denaturate at 95°C for 10 min and cool for 3 min	0.1 mg/ml			
Till 1L	Water	-	19	9.5	3.75

Labeling of the probe:

200-500 ng of DNA (8 µl) + Water (22 µl) was heated at 95 °C for for 5 min and cooled for 2-3 min

Reaction buffer	10 µl
BSA	2 µl
dNTPs	2 µl
^{32}P dCTP	5 µl
Enzyme (Klenow)	1 µl

Above mixture was added to the DNA (final volume of 50 µl) and incubated at 37 °C for 90 min.

Elution:

1. For column equilibration, bottom cap was removed & loosened the upper cap that allows removing the buffer by gravity flow.
2. Column was filled with TE buffer and let it flow through the column
3. DNA sample was added to the column followed by the addition of 400 µl of TE
4. Flow through was collected in tube 1
5. 200ul of TE was added and flow through was collected in tube 2 and repeated the 5th step and collected in around 6 tubes.
6. Counts were measured using Gamma counter (Protocol: 2, P32, 60 s).

Prehybridizytion:

Blot was incubated for 2 h at 60 °C with 15-20 ml church buffer + denatured Hering sperm DNA (200 µl (100 µl / ml concentration))

6. 2 million counts / ml was used (15-20 ml church buffer + denatured Hering sperm DNA (200 µl (100 µl / ml concentration)). Incubate overnight at 65 °C (rotating rocker).

Washing the blots:

1. 3 times washed with wash buffer A (30' each)
2. 3 times washed with wash buffer B (30' each)
3. Exposed to screen for 4 h or overnight.

2.2.22 Data analysis

For data analysis and to calculate statistical significance ImageJ v1.46 (Rasband, W.S., ImageJ, U. S. National Institutes of Health, Bethesda, Maryland, USA, https://imagej.nih.gov/ij/, 1997-2018), Microsoft Excel (Microsoft) and SigmaPlot 13 were used. Figures were generated using Affinity Designer Software (Serif Ltd).

3. Results

Role of the V-ATPase in maturation and fusion of cytotoxic granules in mouse CTLs

3.1 Designing a ratiometric pH sensor for measuring pH in CGs

In order to measure pH inside and outside of CGs from primary mouse $CD8^+$ T cells, we tried different pH-sensitive fluorophores. We expressed Citrine (non-ratiometric), GzmB-Citrine, ClopHensorN (ratiometric, containing E2GFP + TdTomato), GzmB-ClopHensorN, Citrine-Td-Tomato (ratiometric) and Citrine-TagRFP-T (ratiometric) constructs in CTLs. After 12-16 h of transfection cells were used for measurements. pH calibration was done using pH buffers ranging from pH 4 to pH 8.5 and protonophores for H+-permeabilisation of the membranes. For non-ratiometric fluorophores, at the end of each pH buffer measurement (Fx), NH_4Cl (dequenches the fluorophore) was added to the coverslip/cells to get the maximum fluorescence (Fmax). The ratio of Fx/Fmax was calculated for each measurement and plotted in sigma plot using appropriate equations (Figure 10A & B). For Citrine-TdTomato and Citrine-TagRFP-T (ratiometric measurements), the ratio of F515 / F558 was calculated for each buffer condition and plotted in sigma plot (Figure 10D & E). In pH measurement using ClopHensorN, the ratio of F488 / F458 was taken for calibration curve generation (F458 indicates the isosbestic point of the E^2GFP of ClopHensor) (Figure 10C).

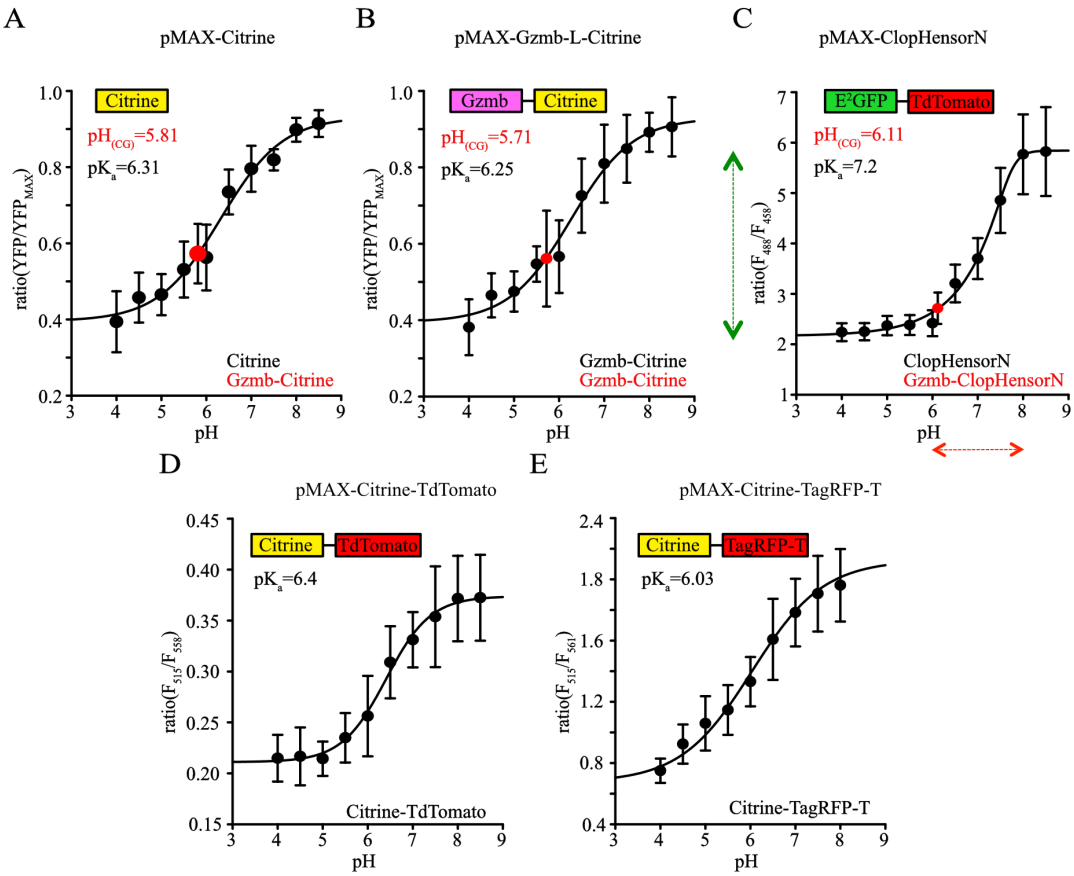

Figure 10: Generation of a ratiometric pH sensor for pH measurements in cytotoxic granules.
(A-E) Primary mouse CD8$^+$ T cells were electroporated with indicated fusion constructs. After 12-16 h of transfection, calibration curve related to pH_{CG} to the pH sensitive excitation fluorescence ratio (Fx/Fmax for citrine and GzmB-Citrine, F488/F458 for ClopHensorN, F515/F561 for Citrine-TdTomato and Citrine-TagRFP-T). pH_{CG} was manipulated by adjusting extracellular pH in the presence of an H^+ permeable ionophore, data were fit using established equations in sigma plot and pKa values were with a fitted 95% confidence interval. Bars indicate ± Stdev.

3.2 The ratiometric pH sensor ClopHensorN (Q69M) measures pH inside CGs quantitatively

From all ratiometric and non-ratiometric pH sensors tested in our hands, we selected ClopHensorN, a genetically encoded ratiometric pH and Cl^- sensor (Raimondo et al., 2013), for our pH measurements because of its dynamic range from 2 to 6 (see Figure 10C on the Y axis) compared to other sensors. Cytotoxic T lymphocytes containing CGs have been reported to be acidic (pH 5.5 ± 0.2 (Kataoka et al., 1996). The pKa value of ClopHensorN (pKa: 7.2; see Figure 10C) results in poor resolution in the expected pH range so we mutated the glutamine at 69th position in E^{2}GFP to methionine in order to lower the pKa value of the sensor (Griesbeck et al., 2001) (Figure 11A). We then tested for correct targeting of the sensor to CGs after expression in mouse CD8$^+$ T cells using ClopHensorN (Q69M) tagged to GzmB (a CG marker) at the C-terminus with flexible GGSGGSGGS

linker. We also stained the cells with Alexa647 conjugated anti-GzmB antibody (Figure 11B) and analysed Pearson's coefficient of correlation and Manders' overlap coefficients (0.53 ± 0.04 and 0.65 ± 0.04 for GzmB to ClopHensorN (Q69M); 0.84 ± 0.02 for ClopHensorN (Q69M) to GzmB), which were significant indicating the correct localization of the sensor to CGs (Figure 11C & D). From this sensor we were able to determine pH and Cl^- concentrations quantitatively as pH 6.11 ± 0.13 and 73.78 ± 3.87 mM respectively (Figure 11E & F).

From these data, we conclude that ClopHensorN (Q69M) can measure the pH inside CGs of CTLs *in-vivo*.

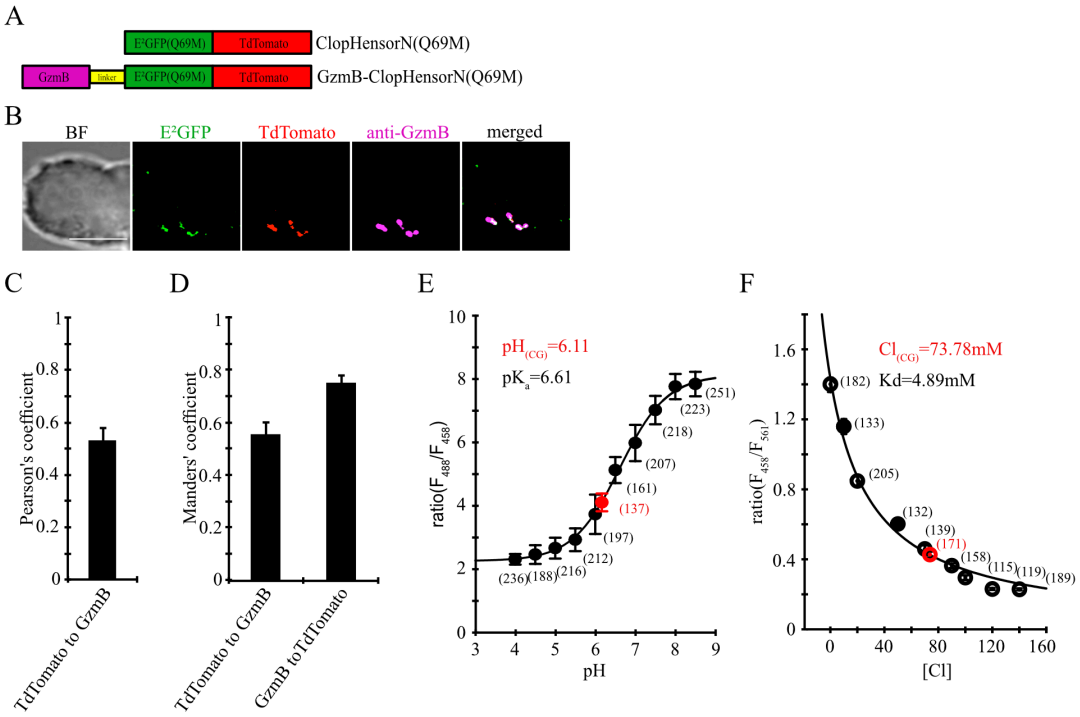

Figure 11: Measurement of the pH in cytotoxic granules using ClopHensorN and ClopHensorN (Q69M)

(A) Schematic showing the design of ClopHensorN (Q69M) and GzmB-ClopHensorN (Q69M). A flexible (GGS)x3 linker (yellow) used between GzmB and ClopHensorN (Q69M). (B) SIM images of fixed primary mouse $CD8^+$ T cells electroporated with GzmB-ClopHensorN (Q69M) and immunostained with Alexa647 conjugated anti-GzmB antibody. (C, D) Pearson's and Manders coefficients of co-localization between GzmB-ClopHensorN (Q69M) and GzmB (n = 16). (E) ClopHensorN (Q69M) calibration curve related to $[pH]_{CG}$ to the pH-sensitive excitation fluorescence ratio (F488/F458). $[pH]_{CG}$ was manipulated by adjusting extracellular pH in the presence of a H^+-permeable ionophore. The pKa was found to be 6.61 with a fitted 95% confidence interval and $[pH]_{CG}$ was measured to be 6.11 ± 0.13 . (F) ClopHensorN calibration curve relating $[Cl^-]_{CG}$ to the Cl^--sensitive excitation fluorescence ratio (F458/F561). $[Cl^-]_{CG}$ was systematically varied by controlling extracellular Cl^- in the presence of a Cl^--permeable ionophore. The estimated Kd was 4.89 mM with a fitted 95% CI between 11.7 and 66.7 mM and $[Cl^-]_{CG}$ was measured to be 73.78 ± 3.87 mM (protocol as described in Raimondo et al., 2013). Bars indicate mean ± SEM. Scale bar, 5 µm.

3.3 Mitochondrial signal sequence targets the ClopHensorN (Q69M) to mitochondria

To ensure the specificity of the sensor, ClopHensor was targeted to mitochondria by adding mitochondrial signal sequence (29 amino acids of human cytochrome oxidase (COX) subunit 8a) at the N-terminus of ClopHensorN (Q69M). CTLs were electroporated with mt-ClopHensorN (Q69M) and immunolabeled with anti-mt antibody to verify the colocalization with the inner mitochondrial membrane specifically (Figure 12B) (Manders' overlap coefficient 0.78 ± 0.02 for ClopHensorN to inner membrane 0.77 ± 0.02 for inner membrane to ClopHensorN). From this data, $[pH]_{mt}$ was measured to be 7.57 ± 0.87 (Figure 12D) (as described in the literature (Porcelli et al., 2005)).

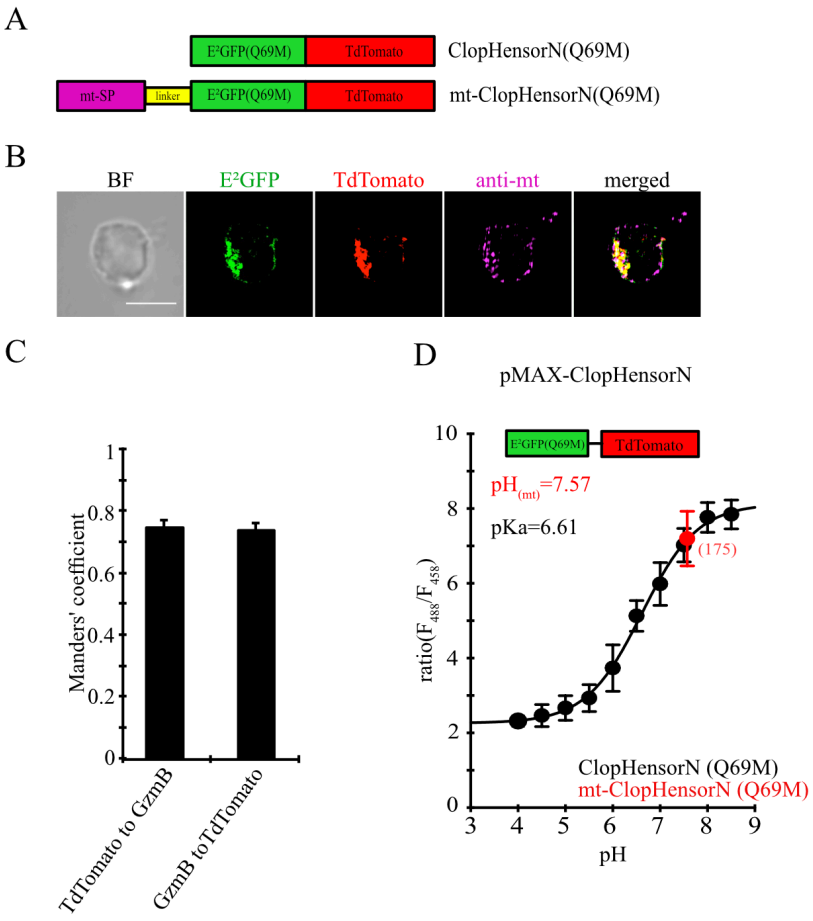

Figure 12: Measuring pH in mitochondria using mt-ClopHensorN (Q69M).
(A) Schematic showing the design of ClopHensorN (Q69M) and mt-ClopHensorN (Q69M) constructs. A flexible (GGS)x3 linker (yellow) used between mitochondrial signal peptide and ClopHensorN (Q69M). (B) Representative SIM images of fixed primary mouse $CD8^+$ T cells electroporated with mt-ClopHensorN (Q69M) and immunostained with anti-mt antibody. (C) Manders coefficients of co-localization between mt-ClopHensorN (Q69M) and anti-mt antibody (n = 8). (D) ClopHensorN (Q69M) calibration curve related to $[pH]_{mt}$ to the pH-sensitive excitation fluorescence ratio (F488/F458). $[pH]_{cytosol}$ was systematically varied by controlling extracellular pH in the presence of an ionophore. $[pH]_{mt}$ was measured to be 7.57 ± 0.87. Bars indicate mean ± SEM. Scale bar, 5 µm.

3.4 Knockdown of a3 isoform of vATPase increases the pH inside the lumen of CGs

After measuring the $[pH]_{CG}$ and $[pH]_{mt}$ in CTLs, we aimed to identity the mechanism of acidification in CGs. To this end, we searched for a candidate for granular acidification. From the literature, in addition to a function in acidifying various intracellular compartments in eukaryotes, the membrane domain (V_0) of the vATPase has been shown to contribute to the Ca^{2+}-dependent transmitter release via a direct role in vesicle membrane fusion (Giovanni et al., 2010). The V_0 domain is a 260 kDa complex composed of six different subunits (a, c, c, c, d, and e) (Xiao et al., 2008). Subunit 'a' is a 116 kDa protein that contains four isoforms, namely a1, a2, a3, and a4. 'a'-subunit isoforms confer organelle specificity (see Figure 6). RT-PCR analysis of a-subunit isoforms revealed that a1, a2 and a3 subunits are expressed in mouse CTLs (Figure 13A). Further, to know which a-subunit isoform is located on CGs, siRNA-mediated knockdown of a1, a2 and a3 subunits was performed (Figure 13B-D). Primary mouse $CD8^+$ T cells were electroporated with siRNAs against a1, a2 or a3 together with a pH sensor GzmB-ClopHensorN (Q69M). After 12-16 h of transfection, $[pH]_{CG}$ was measured with reference to calibration curve shown in (Figure 11E). a3-subunit Knockdown alone increased the pH inside CGs to 6.8 ± 0.08 compared to ns-siRNA treated cells (5.9 ± 0.08). Whereas, in the case of a1 or a2 knockdown, $[pH]_{CG}$ was unchanged (5.97 ± 0.05 and 6.08 ± 0.02 for a1 and ns-siRNA; 6.06 ± 0.07 and 6.06 ± 0.02 for a2 and ns-siRNA, respectively) (Figure 13E).

From this data we conclude that the a3-subunit of V-ATPase is localized on CG membrane and might play a role in pH regulation of CGs.

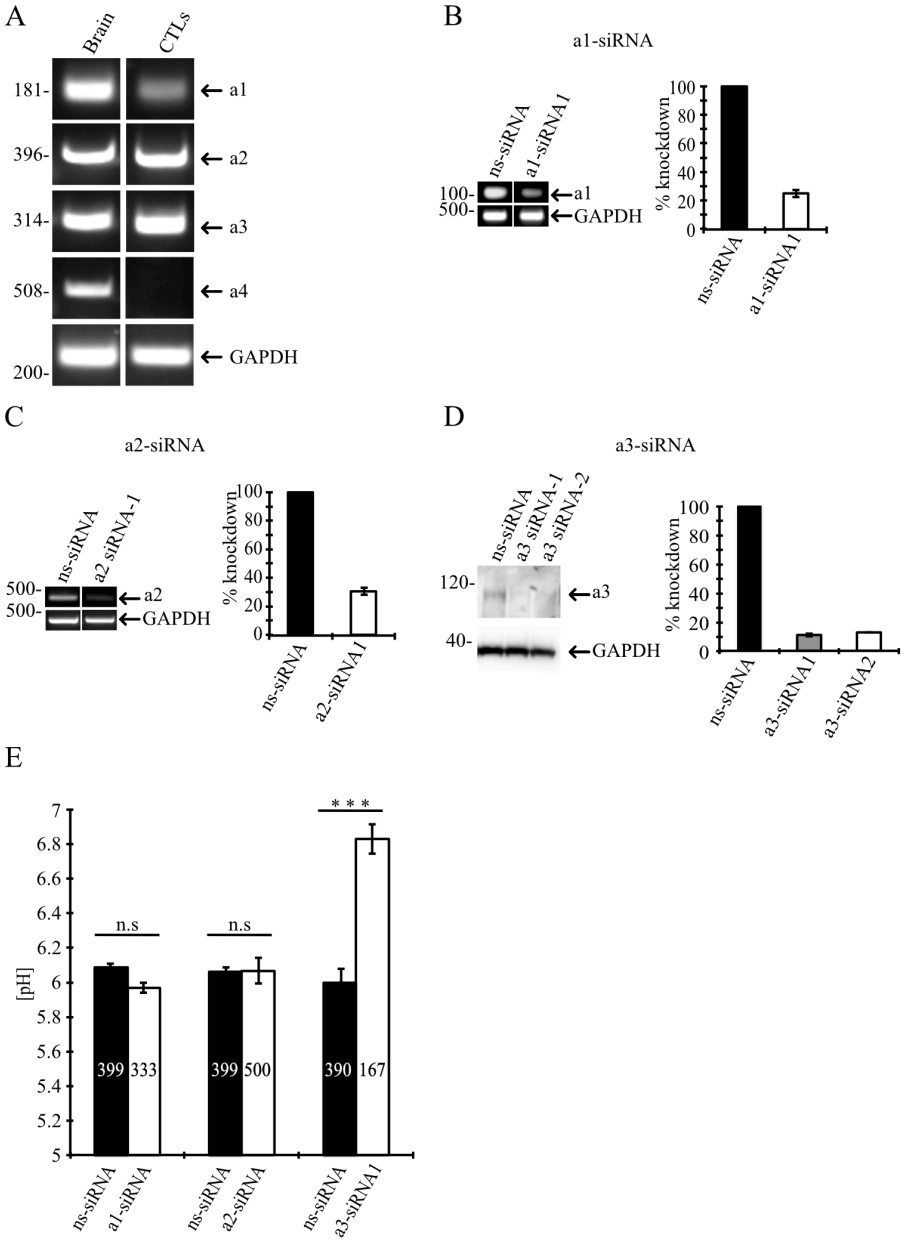

Figure 13: Expression of vATPase a-subunit isoforms in mouse CTLs.
(A) PCR showing the expression of a-subunit isoforms from brain and CTLs. GAPDH was used as loading control. (B-C) Densitometric quantification of cDNA levels from a1 and a2-subunits knockdown by semi-quantitative PCR. (D) Lysates from CD3/CD28 bead stimulated primary mouse CTLs electroporated with either control or a3-siRNA1 or 2 respectively and blotted for a3 (top) and GAPDH (bottom) as loading control. Quantification of a3 protein expression levels (in % normalized to control siRNA-treated CTLs) by densitometry. (a3-siRNA1, N = 3; ***p < 0.001 and anti-a3 siRNA2, N = 3; ***p < 0.001 (t-test)). (E) Stimulated mouse CTLs were co-transfected with ns-siRNA (control) or anti-a1, anti-a2 or anti-a3 siRNA1 along with GzmB-ClopHensorN (Q69M). After 16-18 h of transfection $[pH]_{CG}$ was measured in reference to calibration curve (**Figure 11**E) from the ratio (F488/F458) (N = 3, n = 167 for a3-siRNA1; n = 333 for a1-siRNA1; n = 500 for a2-siRNA respectively). Data indicate mean ± SEM.

3.5 a3-subunit of vATPase is localized on cytotoxic granules

Further, with SIM microscopy we checked the localization of a3 subunit by immunostaining with anti-a3 antibody (gift from Thomas J. Jentsch, FMP, Berlin) in mouse CTLs isolated from synaptobrevin2-mRFP knock-in mice where

synaptobrevin2 was fused to a red fluorescent protein, mRFP (Matti et al., 2013b). a3-subunit showed significant co-localization with cytotoxic granule marker GzmB with Pearson's coefficients of correlation of 0.64 ± 0.08 (Figure 14B). This confirms the presence of a3 isoform containing V-ATPase on cytotoxic granules.

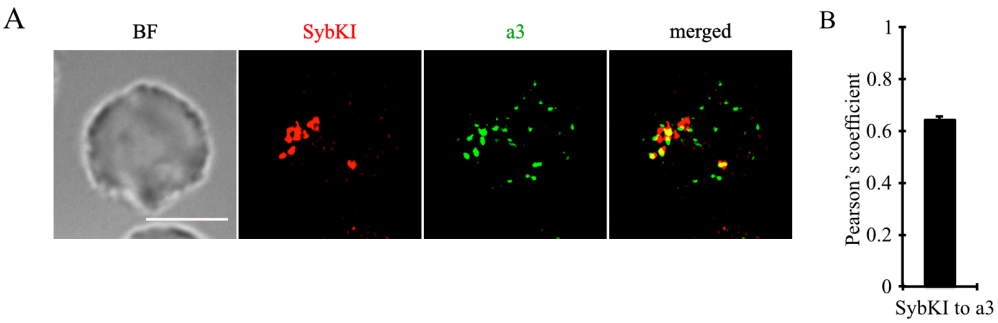

Figure 14: Localization of a3 subunit in mouse CTLs.
(A) Representative SIM images from stimulated SybKI CTLs immunostained with polyclonal anti-a3 antibody (B) Pearson's overlap coefficients of co-localization of SybKI with a3 are given in the text (N = 3, n = 25). Scale bar, 5 µm.

3.6 The killing capacity of CTLs is reduced upon a3 subunit knockdown

It has been shown that the loading of synaptic vesicles with neurotransmitters in neurons requires V-ATPase dependent acidification (Amara and Kuhar, 1993). (Hiesinger et al., 2005), moreover they showed that the a1-subunit of the V_0 domain is required for functional synaptic vesicle exocytosis in *Drosophila* v100 mutant synapses (a1-subunit isoform in *Drosophila*) the size of mEPSCs were smaller due to a lower concentration of neurotransmitter in the synaptic vesicles. These findings led us to examine the transport of GzmB to the CGs upon a3-knockdown. For that purpose, we electroporated SybKI CTLs with ns-siRNA or a3-siRNA1 and stained CGs with Alexa 647 conjugated anti-GzmB antibody after 16hr of transfection. We observed no significant difference between the localization of GzmB in cells treated with either ns-siRNA or a3-siRNA1 which gave a Pearson's coefficients of correlation of (0.71 ± 0.072 and 0.66 ± 0.08; A & B). As a functional assay to check the killing capacity of CTLs after down-regulating the a3-subunit by siRNAs, we did a calcein-AM based killing assay. After a3-subunit knockdown, there was a reduction in target cell lysis (12.8 ± 0.67 % and 9.46 ± 1.18 for (20:1 and 10:1 (CTL:target cell ratio)); for a3-siRNA1, 10.66 ± 3.01 % and 9.02 ± 1.41 for (20:1 and 10:1 (CTL:target cell ratio)); for a3-siRNA2) compared to (35.78 ± 1.2 % and 30.09 ± 1.63 for (20:1 and 10:1 (CTL:target cell ratio)); for wt, 33.57 ± 1.81 % and 31.1 ± 0.98 for (20:1 and 10:1 (CTL:target cell ratio)); for ns-siRNA, 31.60 ± 1.16 % and 28.7 ± 0.82 for (20:1 and 10:1 (CTL:target cell ratio)); for a1-siRNA1), and 30.37 ± 2.51 % and 27.67 ± 1.26 for (20:1 and 10:1 (CTL:target cell ratio)); for a2-siRNA1) (Figure 15C).

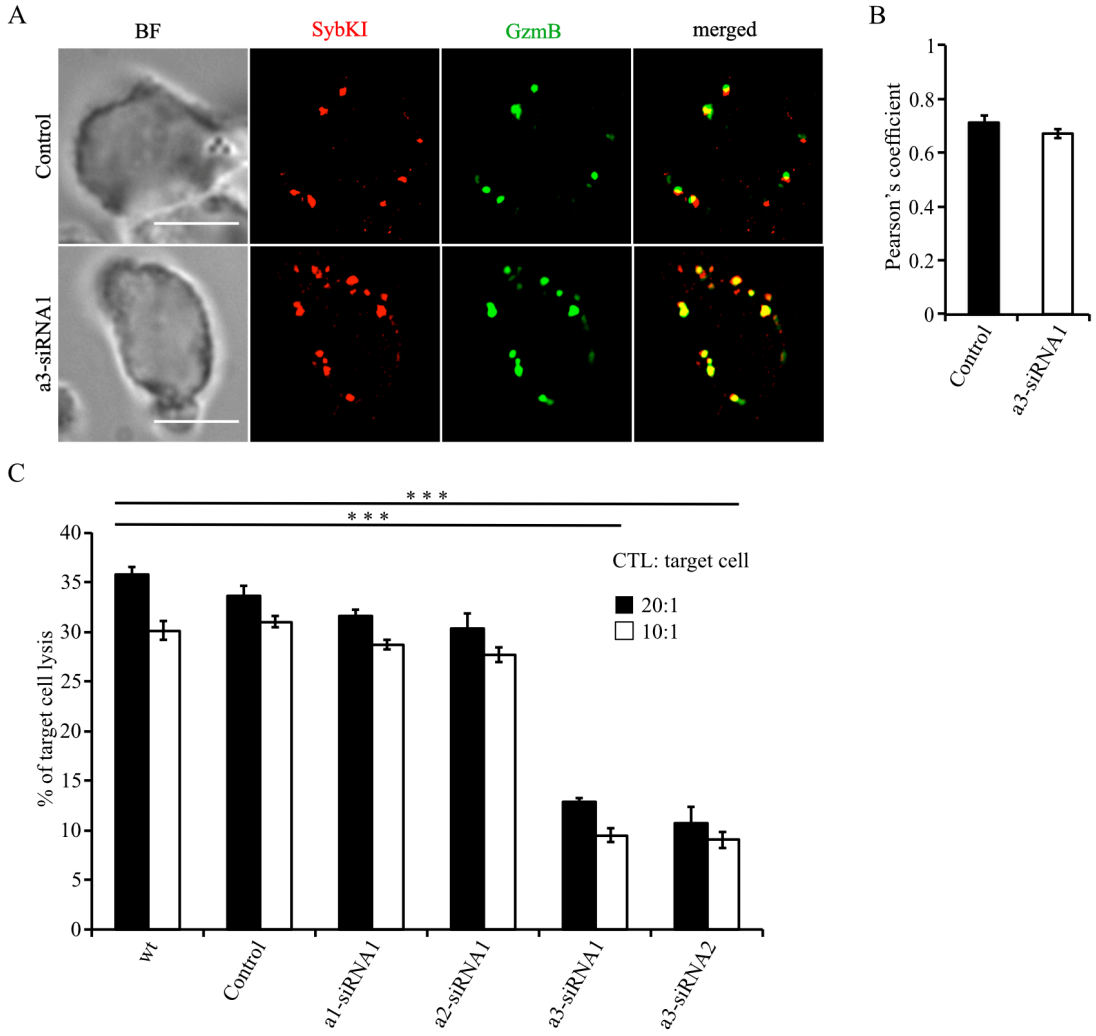

Figure 15: The a3-subunit knockdown decreases the killing efficiency of CTLs
(A) Representative SIM images of primary CD8$^+$ T cells isolated from SybKI mice immunostained with an anti-a3 antibody. (B) Pearson's coefficients of co-localization of endogenously labeled synaptobrevin2 and a3-subunit are given in the text (n=11). (C) Calcein-based killing assay for CTLs electroporated with either ns-siRNA, a1-siRNA1, a2-siRNA1, a3-siRNA1 or a3-siRNA2 18 h after transfection. Experiments were carried out in duplicates (N = 3; ***p < 0.001 (t-test)). Data are shown as mean ± SEM. Scale bar, 5 µm.

3.7 GzmB-mTFP knock-in mice as a tool for studying v-ATPase function in mouse CTLs

GzmB-mTFP knock-in mouse was generated by using CRISPR-cas9 technology with the help of guide RNA directly in embryonic stem cells (ES) from C57BL6/N mouse strain. Before using this knock-in mouse as a tool for studying the v-ATPase function in the present study we verified the localization of GzmB-mTFP by immunostaining with Alexa 647 conjugated GzmB antibody. SIM analysis showed significant co-localization of GzmB with endogenous mTFP-tagged GzmB protein (Figure 16B) with Pearson's coefficients of correlation of (0.67 ± 0.016) and

Manders' overlap coefficient of (0.75 ± 0.012 for GzmB-mTFP to GzmB and 0.76 ± 0.012 for GzmB to GzmB-mTFP; Figure 16C & D). We also validated the function or activity of GzmB tagged to mTFP at the C-terminus by performing a live-cell killing assay. We incubated GzmB-mTFP expressing $CD8^+$ T cells with p815 target cells stably expressing an inverse FRET construct called Casper3-GR. This construct has a DEVD sequence interspaced between the FRET pair Tag-GFP and Tag-RFP. This side can be cleaved by caspase-3, which is indicated by a reduction in FRET between the fluorophore-partners; hence an increase in green and decrease in red fluorescence results. As shown in (Figure 16F) we observed an increase in donor fluorescence intensity (Figure 16F, Tag-GFP channel) over time, demonstrating that the GzmB protein was functional and its release leads to apoptosis by activating caspase-3 in target cells. After demonstrating that GzmB is active and localized to CGs, we tested the fusion of GzmB-mTFP containing vesicles at the plasma membrane in an independent assay by Total Internal Reflection Fluorescence Microscopy (TIRFM). After seeding GzmB-mTFP expressing CTLs on CD3-coated coverslips the IS was formed quickly and we observed a rapid accumulation of CGs, indicated by individual green (GzmB-mTFP) puncta (Figure 16E). The Individual fusion events were quantified by a sudden drop in the mean fluorescence intensity of GzmB-mTFP caused by the release and subsequent diffusion of the soluble GzmB-mTFP (compare frame 4 and 5 upper and lower panel of (Figure 16E).

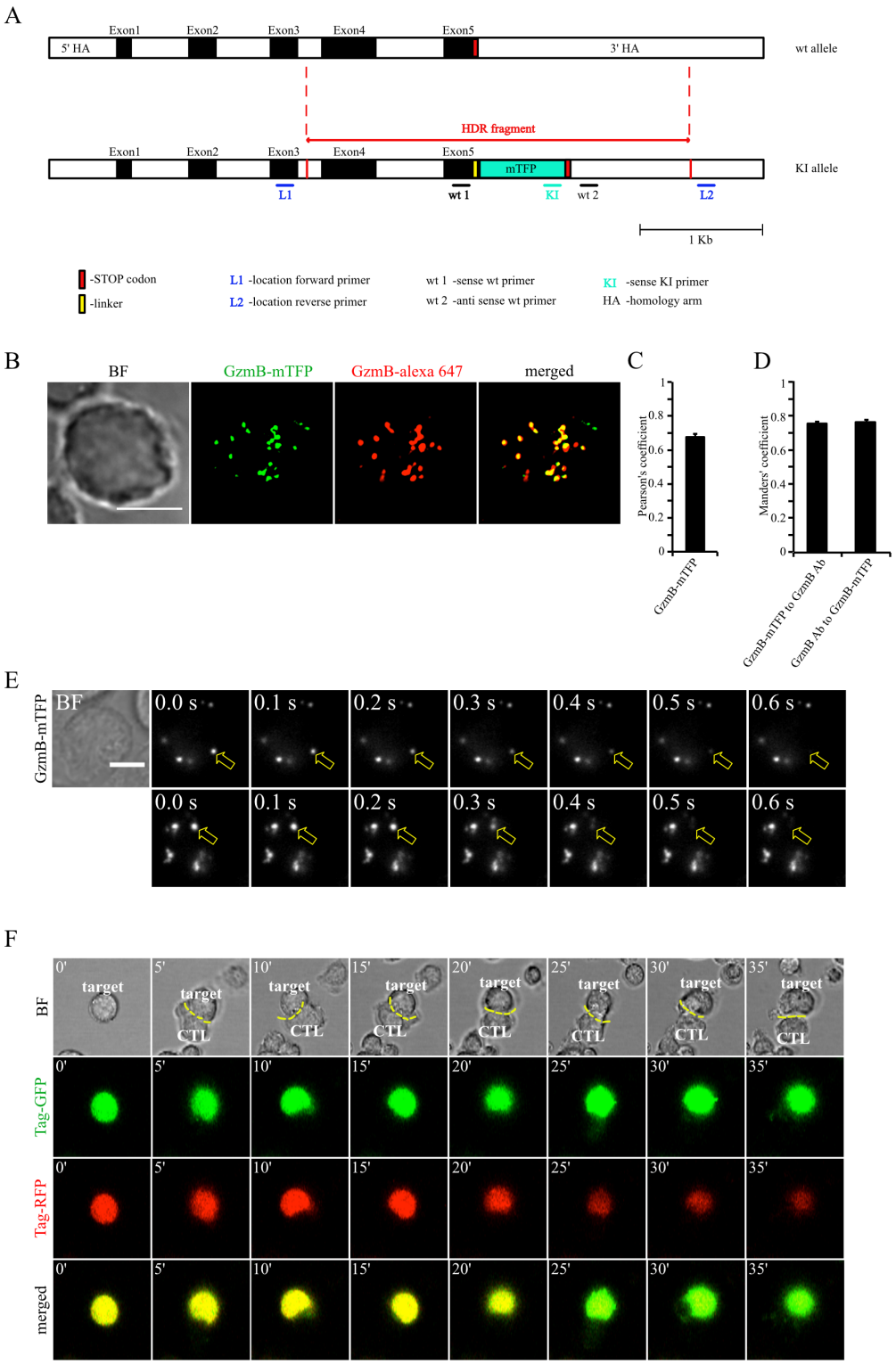

Figure 16: GzmB-mTFP Knockin mice.
(A) CRISPR cas9 mediated knockin strategy for generating GzmB-mTFP knock-in mice. (B) Bead stimulated primary CD8$^+$ T cells isolated from GzmB-mTFP KI mouse on day 5 were fixed and stained with Alexa647 conjugated anti-GzmB antibody. (C, D) Pearson's and Manders coefficients of co-localization between GzmB-mTFP and endogenous GzmB are given in the text (n=10). (E) Selected live-cell TIRF microscopy images of GzmB-mTFP in a CTL in contact with an anti-CD3 coated coverslip. Fusion events are indicated with open arrows (seven frames shown per granule fused). (F) Live cell killing assay showing a mouse CTL in contact with p815 target cell stably expressing Casper3-GR (FRET construct containing Tag-GFP and Tag-RFP

with a target cleavage site DEVD of Caspase 3 (activated via GzmB). LSM images at indicated time points showing a reduction in FRET signal, indicating the killing of the target cell. Bars show mean ± SEM. Scale bar, 5 µm.

3.8 Knockdown of a3-subunit strongly reduces the fusion of cytotoxic granules at the IS

Our data demonstrate that v-ATPase a3-subunit co-localizes with the CG marker GzmB and its knockdown increases the pH specifically inside the CGs. To investigate whether the a3 subunit is involved directly in the fusion of CGs with the plasma membrane, we performed TIRFM experiments. For that purpose, we electroporated primary mouse CTLs isolated from GzmB-mTFP knock-in mice with two different siRNAs against a3 (siRNA1 and 2) and analysed CG fusion at the plasma membrane on coverslips coated with anti-CD3 antibody. In contrast to scrambled control siRNA, either a3 siRNA reduced the expression of a3 to >10-20 % for a3-siRNA1 and 2 of the original level, respectively. Both siRNAs significantly reduced the number of CGs appearing in the TIRF plane (Figure 17A) and number of CTLs showing CG fusion to less than 60% of the values measured upon transfection of control siRNA (from 47.08 ± 2.86% to 10.09 ± 1.51% for a3-siRNA1, n = 161; and from 47.08 ± 2.86% to 10.99 ± 0.67% for a3-siRNA2, n = 143, respectively compared to ns-siRNA; Figure 17B). Simultaneously, the average number of CG fusion events observed in CTLs expressing either a3 siRNA was reduced as well (from 4.24 ± 0.33 to 2.20 ± 0.24 for a3-siRNA1; and from 4.24 ± 0.33 to 2.28 ± 0.23 for a3-siRNA2, respectively compared to ns-siRNA; Figure 17C). The average number of CGs appearing in the TIRF plane per cell was significantly reduced (4.74 ± 2.88 for a3-siRNA1; and 4.61 ± 0.90 for a3 siRNA2, respectively; Figure 17D) compared to (16.1 ± 2.38 for wt; and 15.96 ± 2.88 for ns-siRNA, respectively; Figure 17D).

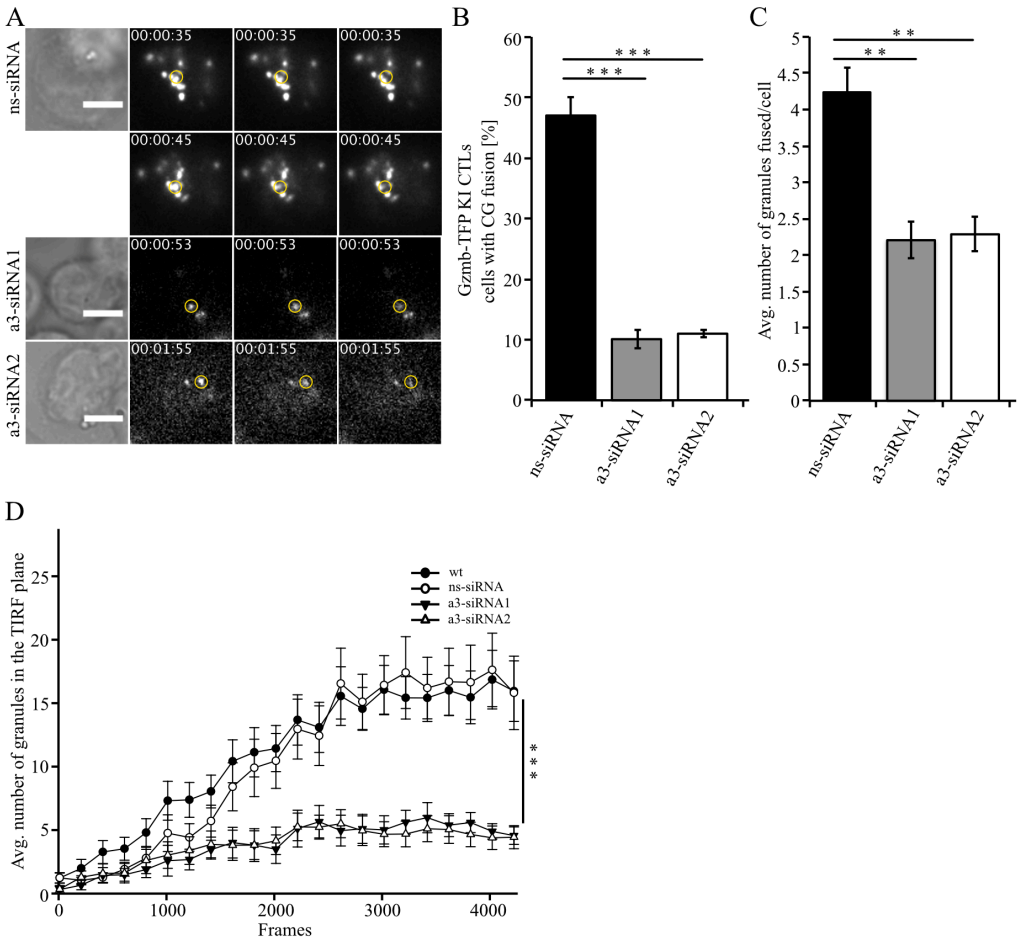

Figure 17: Knockdown of a3 strongly reduces the fusion of cytotoxic granules at the IS. (A) Selected live-cell TIRF microscopy images of GzmB-mTFP in a CTL electroporated with either ns-siRNA or a3-siRNA1 or a3-siRNA2 in contact with an anti-CD3 coated coverslip. Fusion events are indicated with open circles (three frames shown per granule fused). (B) Mouse primary CD8$^+$ T cells isolated from GzmB-mTFP KI mouse electroporated with either ns-siRNA or a3-siRNA1 or a3-siRNA2 and imaged 16-18 h after transfection. The mean percentage of cytotoxic granule fusion in cells electroporated with either ns-siRNA (N =3 & n = 98) or (N = 3, n = 161, **p = 0.001, t-test; for a3-siRNA1 and N=3, n=143, ***p = 0.001, Holm-Sidak test; for a3-siRNA2 (C) Mean average number of granules fused over time in the TIRF plane per cell (p = **0.004, t-test; for a3-siRNA1 and **p = 0.002, Holm-Sidak test; for a3-siRNA2). (D) The mean average number of GzmB-mTFP containing vesicles in the TIRF plane per cell during 7 minutes of measurements from wt CTLs or cells electroporated with either ns-siRNA or a3-siRNA1 or a3-siRNA2 (N = 3, n = 15, ***p<0.001 (Kruskal-Wallis One Way Analysis of Variance on Ranks). Bars indicate mean ± SEM. Scale bar, 5 µm.

3.9 GzmB levels were increased whereas Perforin levels were decreased in a3 Knockdown

Having (Figure 15A) concluded that there was no defective GzmB transport to the CGs but in spite of a strong reduction in the fusion of CGs from TIRF experiments (Figure 17) we expected an increased intracellular GzmB concentration in the a3 KD cells. As expected, we found an increase in GzmB levels in a3-KD and for control purposes the cells were treated with CMA (V-ATPase inhibitor) for 4 h compared to control (GzmB levels normalized to ns-siRNA treated cells) (100 % for ns-siRNA; 140.3 ± 7.35 % for a3-siRNA1; 179.4 ± 16.82 % for CMA; Figure 18A

& B). However, we observed a reduction in the levels of Perforin in a3-KD and CMA treated cells compared to control (Perforin levels normalized to ns-siRNA treated cells) (100 % for ns-siRNA; 55.46 ± 8.88 % for a3-siRNA1; 38.02 ± 9.11 % for CMA; Figure 18C) by western blot analysis. These findings suggest that after a3-KD, GzmB might not be released possibly due to the neutral pH inside CGs. The neutral pH in CGs may also induce the proteolytic degradation of Perforin.

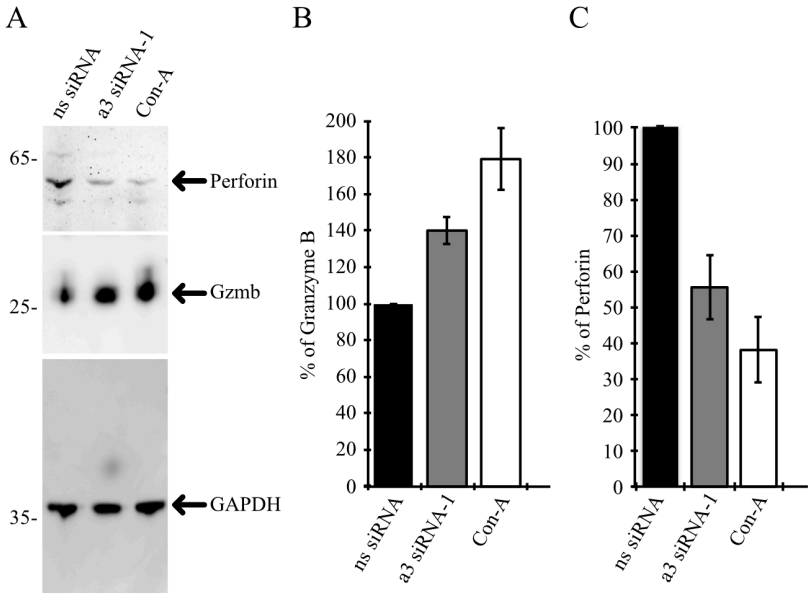

Figure 18: GzmB and Perforin levels after a3 Knockdown.
(A) Lysates from bead stimulated wt mouse CD8$^+$ T cells were electroporated with either ns-siRNA or a3-siRNA1 for 16-18 h or treated with 100 nM concanamycin-A (CMA) for 4 h and blotted for Perforin (top), GzmB (middle) and GAPDH (bottom) as loading control. (B) & (C) Quantification of GzmB and Perforin protein expression (in % normalized to control siRNA-treated CTLs) by densitometry. Bars indicate mean ± SEM. Scale bar, 5 µm.

3.10 The a3 subunit of V-ATPase did not show any interaction with the V-SNARE Synaptobrevin2

Next, we tested the role of the a3 subunit in the fusion of CGs by forming a SNARE complex with the vesicular SNARE VAMP2 being the vSNARE in mouse CTLs (Matti et al., 2013b). It has been shown that the a3 subunit of vATPase is involved in the final step of vesicle fusion by interacting with Synaptobrevin2 (v-SNARE in neuronal cell types and mouse CTLs) (Di Giovanni et al., 2010a). We performed pulldown assays by generating a fusion protein for Synaptobrevin2 (Syb2-Twin-Strep-tag) (Figure 19A) and electroporated mouse CTLs with this construct. Western blots of pull-downs from mouse CTLs expressing tagged synaptobrevin2 did not show any interaction with a3 subunit, however, we could detect SNAP-23, a tSNARE partner for synaptobrevin2 (Figure 19B).

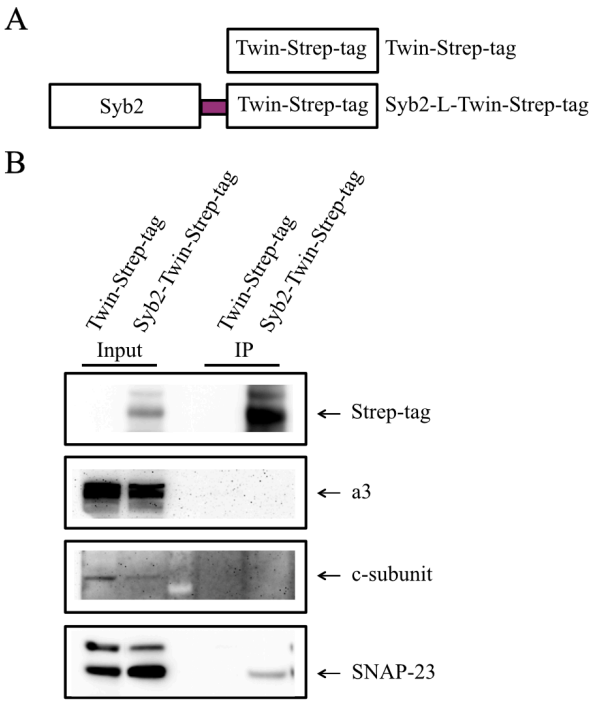

Figure 19: Syb2-Twin-Strep-tag pulldown assays.
(A) Schematic showing the design of Twin-Strep-tag and Synaptobrevin2 fusion constructs used for pulldown assay. The Twin-Strep-tag was fused at the C-terminus of Synaptobrevin2 connected by a (GGS)x3 linker. (B) Bead-activated mouse CTLs electroporated with Twin-Strep-tag-tagged Synaptobrevin2 were lysed and incubated with Strep-Tactin sepharose beads. The precipitates were analyzed with antibodies against Strep-tag, a3-subunit, c-subunit and SNAP-23.

3.11 The a3 subunit did not show any interaction with Rab7a or Rab27a in Strep-tag pulldown assays

In osteoclasts, the a3 subunit of V-ATPase plays a role in trafficking of secretory lysosomes to the plasma membrane by interacting with dominant-negative GDP-bound form of Rab7A and aids in bone resorption by providing optimal conditions. The a3 subunit also interacts with GDP-bound Rab27A, a key player involved in docking and fusion of secretory lysosomes with plasma membrane in CTLs (Matsumoto et al., 2018) (van der Sluijs et al., 2013). We expected a similar scenario in CG transport and fusion with the plasma membrane in mouse CTLs based on previous results from TIRFM. We performed pulldown assays by generating fusion proteins for Rab7A and Rab27A (Twin-Strep-tag-Rab7a, Twin-Strep-tag-Rab7a (T22N), Twin-Strep-tag-Rab7a (Q67L) Twin-Strep-tag-Rab27a, Twin-Strep-tag-Rab27a (T23N) and Twin-Strep-tag-Rab27a (Q68L)) (Figure 20A & B) and electroporated mouse CTLs with these constructs. Western blots of pull-downs from mouse CTLs expressing tagged Rab7A or Rab27A did not show any interaction with a3 subunit (Figure 20C & D).

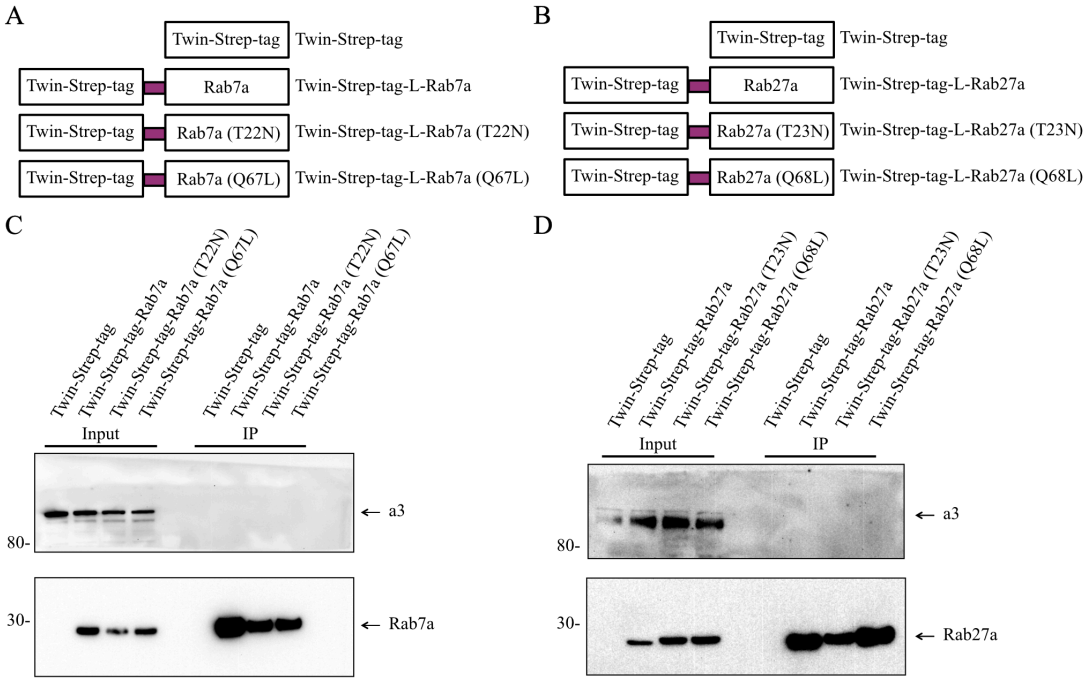

Figure 20: Rab7a and Rab27a pulldown assays.
(A, C) Twin-Strep-tag, Rab7a and Rab27a fusion constructs used for pulldown assay. The Twin-Strep-tag was fused at the N terminus for Rab7a, Rab7a(T22N), Rab7a(Q67L), Rab27a, Rab27a(T23N) and Rab27(Q68L) connected by a (GGS)x3 linker. (B) Bead-activated mouse CTLs electroporated with Twin-Strep-tag-tagged Rab7a constructs (D) or Twin-Strep-tag-tagged Rab27a constructs. Cell lysates were incubated with Strep-Tactin sepharose beads and the precipitates were analyzed with antibodies against Strep-tag and a3-subunit. As control, cells were electroporated with Twin-Strep-tag construct alone. 10% of the lysates were loaded as input.

3.12 Cytotoxic granules from a3-silenced CTLs were away from microtubules

Cytotoxic granules are transported along the microtubular network towards the IS. Though it is not clear which Rab protein mediate this step, if there were no interaction with microtubules in the absence of a3 subunit, the distance between CGs and microtubules would also be more. To quantitatively measure this distance accurately, we took advantage of STED microscopy (X, Y resolution of 50nm and a 100nm Z resolution). CTLs isolated from GzmB-knock-in were transfected with a3-siRNA1 and 2 and stained with SiR-tubulin to visualize the microtubules in live cells. As expected, the average distance between tubules and CGs were significantly higher (470 ± 29.35 nm for a3-siRNA1; 260 ± 28.04 nm for a3-siRNA2) compared to control (117.14 ± 19.58 nm) (Figure 21C).

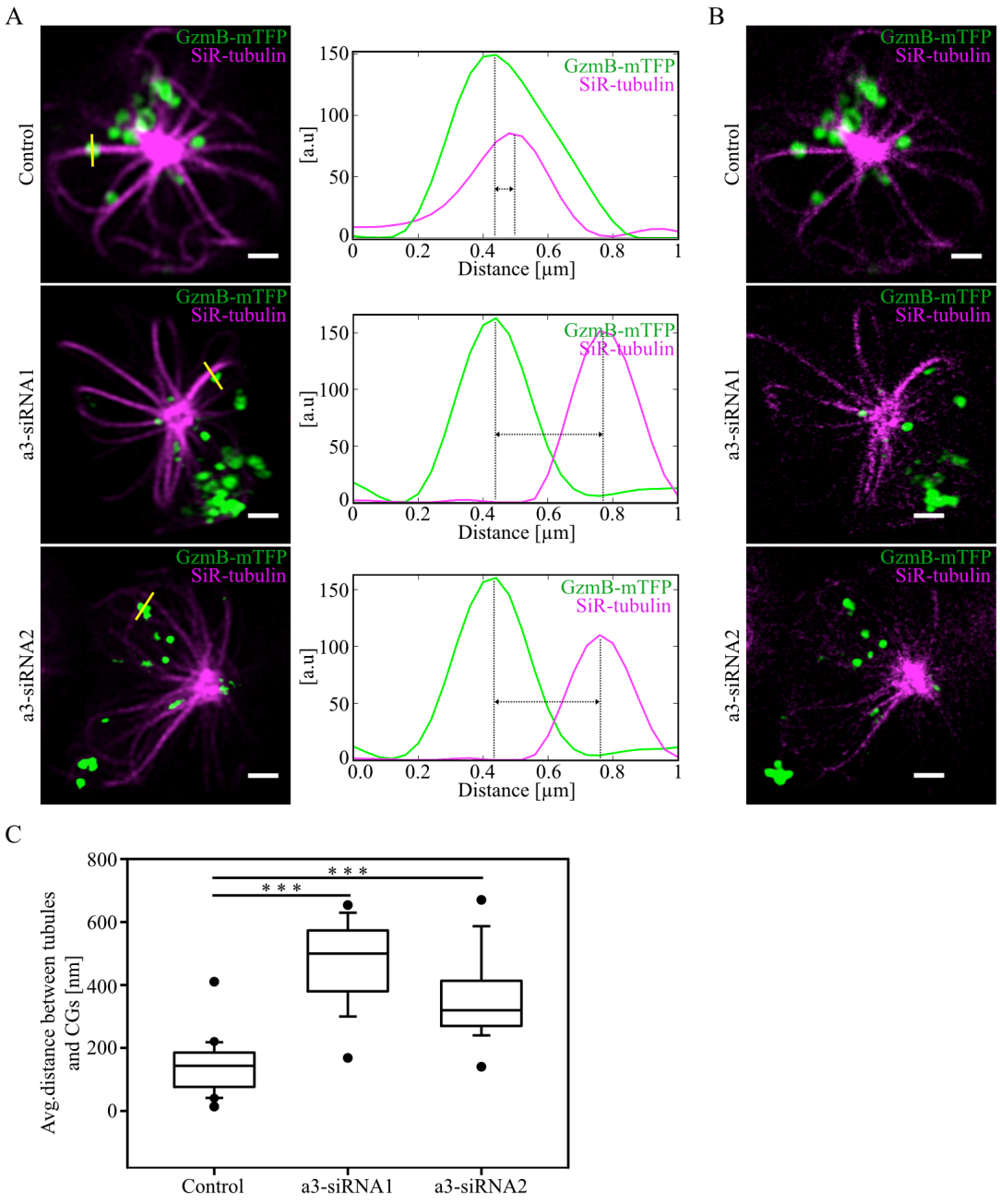

Figure 21: Distance between CGs and microtubules increased upon a3 knockdown. (A) Selected live-cell confocal and (B) STED images from GzmB-mTFP CTLs stained with SiR-tubulin. (C) Box plot demonstrating the mean average distance between microtubules and cytotoxic granules (n=20, ***p = 0.001 for a3-siRNA1 and n=20; ***p = 0.001 for a3-siRNA2 (Holm-Sidak test)) compared to control. Bars indicate mean ± SEM. Scale bar, 1 µm.

3.13 Morphology of cytotoxic granules is altered upon a3 knockdown

Further, we wanted to know whether the reduction in target cell killing is due to impairment in fusion of CGs or the biogenesis itself. Therefore, we analysed the average number of granules per cell after transfecting the day 1 bead stimulated CTLs that were isolated from GzmB-mTFP knock-in mice with ns-siRNA or a3-

siRNA1 or 2 with structured illumination microscopy (SIM) as (12.59 ± 1.08 (n=87); for ns-siRNA, 12.61 ± 1.14 (n=83); for a3-siRNA1 and 12.76 ± 1.25 (n=76); for a3-siRNA2; Figure 22A). These results indicate that a3-subunit of V-ATPase has no role in the biogenesis of CG.

Since there is no biogenesis defect, there are two possibilities that could explain the defective CTL function. First: a3 might play a role in the fusion of CGs by forming a SNARE complex at the IS. Second: a3 might recruit small GTPases that interact with kinesin motor proteins that have been known as key molecular players which help in the trafficking of CGs along the microtubules to the IS (similar to an a3-dependent lysosomal transport mechanism shown by (Matsumoto et al., 2018).

We also performed electron microscopy experiments to visualize the ultrastructural or morphological changes of CGs after a3 knockdown. EM data clearly showed that the avarage greyscale (indication for proteoglycan matrix with serglycin) (0-256) was lesser upon a3-knockdown (shown in open white triangles) (123 ± 4.0 for a3-siRNA1 and 121 ± 5.0 for a3-siRNA2) compared to control (shown in closed dark triangles) (184 ± 6.57 for ns-siRNA) (Figure 22C). Also, average diameter of the CGs was significantly increased (353.45 ± 14.62 nm for a3-siRNA1 and 350.5 ± 19.77 nm for a3-siRNA2) compared to control (220 ± 12.81 nm) (Figure 22D & E). Further, by performing correlative fluorescence electron microscopy we confirmed that these enlarged granules were indeed GzmB positive (Figure 22B).

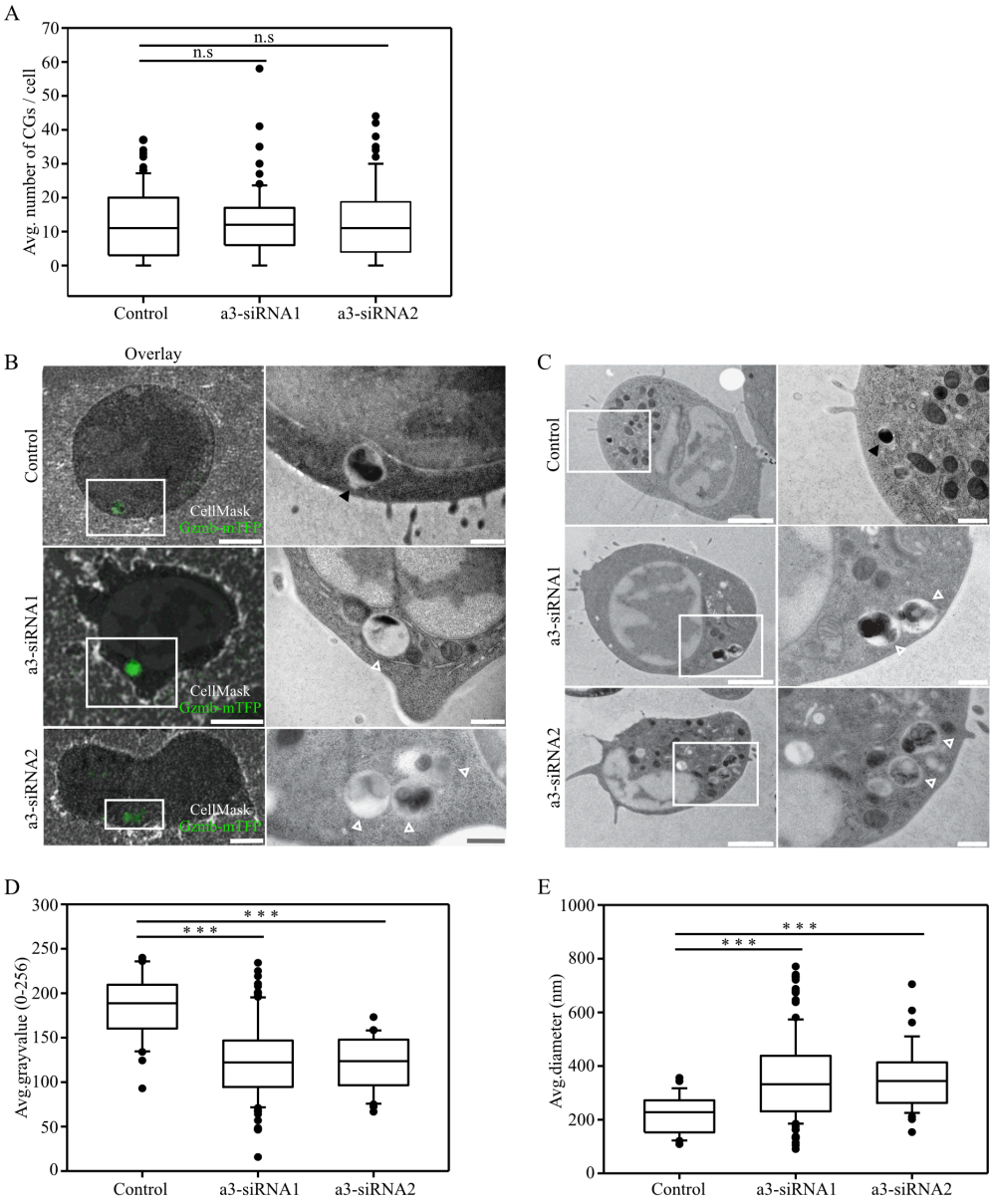

Figure 22: Ultrasturucture of CGs upon a3 knockdown.
(A) The average number of CGs per cells in CTLs isolated from GzmB-mTFP KI mice electroporated with either ns-siRNA (control) or anti-a3-siRNA1 or 2 and fixed after 16-18 h of transfection. (B) Electron micrographs of resting CTLs obtained from GzmB-mTFP knock-in mice treated with ns-siRNA, a3-siRNA1 and 2 (left upper, middle and lower panel). From left to right: TEM image and magnified region of the TEM-image marked with the white frame. The magnified inserts show organelles with electron dense areas, which were used for statistical analysis. Scale bar, 2 µm for the three left images (11.000x magnification) and 0.5 µm for the right images (30.000x magnification). (C) Representative correlative fluorescence electron microscopy images of resting CTLs obtained from GzmB-mTFP knock-in mice treated with ns-siRNA, a3-siRNA1 and a3-siRNA2 (left upper, middle and lower panel). From left to right: SIM (MIP image)/TEM overlay and magnification of TEM image marked with the white frame. The magnified inserts indicate GranzymeB-positive organelles with electron dense areas. Scale bar, 2 µm for the three left images (from top to bottom: magnification 9.300x, 11.000x and 4.800x) and 0.5 µm for the right images (30.000x, 30.000x and 37.000x magnification, respectively). (D) Mean average greyscale values of CGs (p = ***0.001 for a3-siRNA1 and ***p = 0.001 for a3-siRNA2 (Holm-Sidak test) compared to control. (E) Mean average diameter of CGs (p = ***0.001 for a3-siRNA1 and ***p = 0.001 for a3-siRNA2 (Dunn's test) compared to control. Bars indicate mean ± SEM.

vSNARE of human CTLs

3.14 Fusion of cytotoxic granules is insensitive to tetanus toxin

Since in the previous part of the thesis we could demonstrate a major role of the a3-subunit of the V-ATPase for maturation of CGs. We now looked deeper into the next step, namely, fusion of mature CGs with the plasma membrane at the synapse. We particularly asked for the so far unknown vesicular SNARE (vSNARE) of the human SNARE-complex catalysing the fusion of CGs at the IS. In order to investigate the v-SNARE responsible for CG fusion in human CTLs, we used tetanus toxin as a tool to screen different isoforms of v-SNARE family (VAMPs). Tetanus toxin (TeNT) is a zinc-endopeptidase from anaerobic *Clostridia* bacteria that specifically cleaves VAMP1, VAMP2 (synaptobrevin2) and VAMP3 (cellubrevin), but not VAMP4, VAMP7 (TI-VAMP) (Chaineau et al., 2009) or VAMP8 (Humeau et al., 2000; Proux-Gillardeaux et al., 2005). We expressed primary, bead stimulated day 3 human $CD8^+$ T cells with the protease-containing light chain of TeNT and tested its function by western blot to compare the expression levels of VAMP2 and VAMP7 (Figure 23A). As expected, TeNT expression (with 71.8 ± 7.2% transfection efficiency) resulted in effective cleavage of VAMP2 (27.6 ± 1.3% expression) compared to CTLs expressing only GFP (control) (68.5 ± 8.3% transfection efficiency) while the protein levels of VAMP7 was unchanged (92.1 ± 0.9% and; Figure 23B). Further, to visualize and quantify fusion of individual CGs upon TeNT expression we performed total internal reflection fluorescence microscopy (TIRFM) (Figure 23C). Representative still images for individual fusion events from GFP or TeNT electroporated CTLs are represented with open arrows. Five frames were shown for one fusion event. The percentage of CTLs showing fusion events were similar between CTLs expressing TeNT and CTLs expressing only GFP (36.7 ± 4.71 % for TeNT and 39.8 ± 5.9% for GFP; Figure 23D). The average number of granules that fused at the IS was similar in both groups (2.2 ± 0.5 for TeNT and 2.3 ± 0.4 for GFP; Figure 23E). From these data we conclude that CG secretion from primary, human $CD8^+$ T cells is uninfluenced by TeNT, eliminating VAMP1, VAMP2, and VAMP3 as candidates that mediate CG exocytosis.

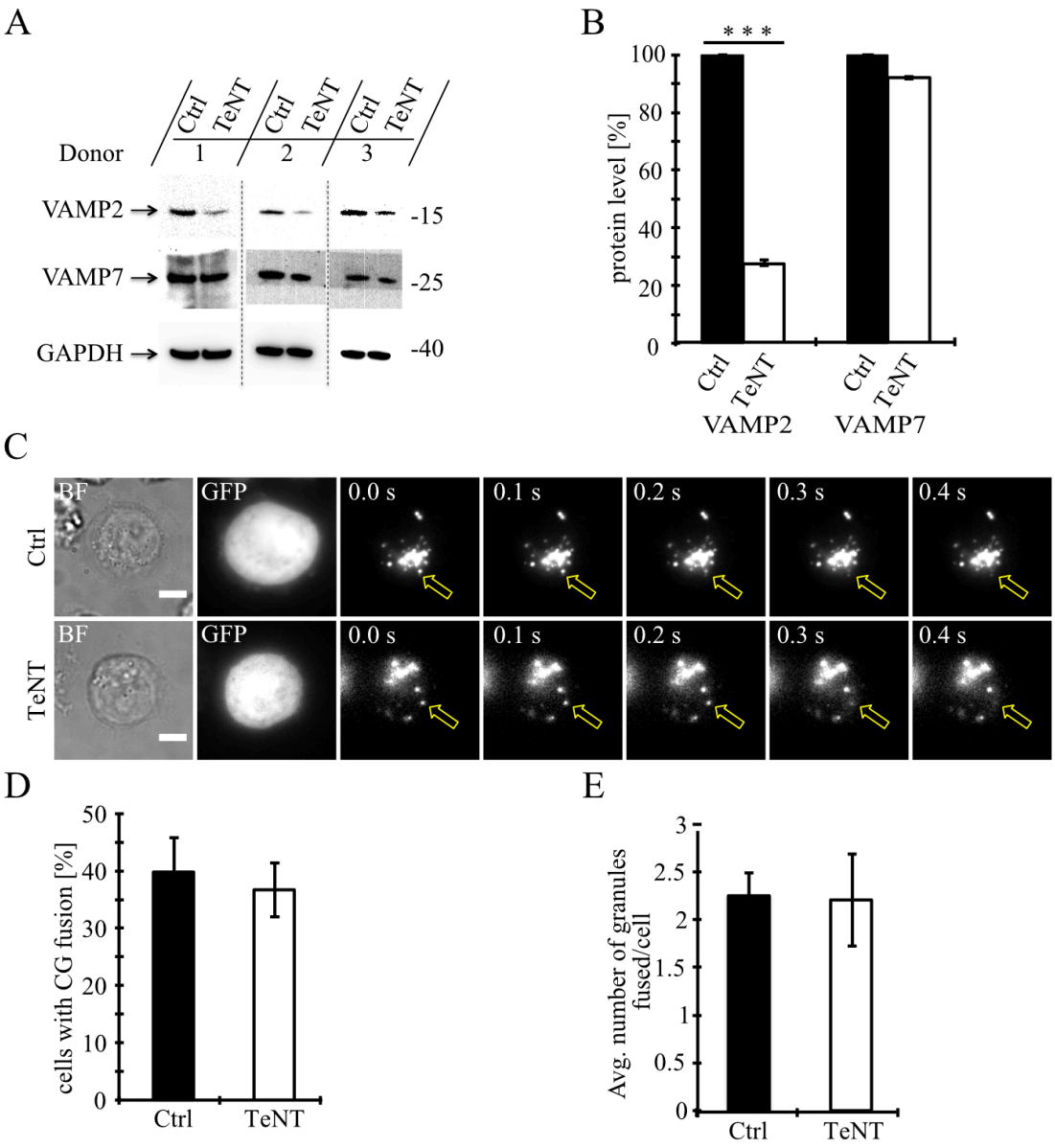

Figure 23: Fusion of cytotoxic granules with the plasma membrane is insensitive to Tetanus toxin.

(A) Bead-activated human $CD8^+$ T cells were electroporated with control GFP or TeNT-GFP constructs as described. Protein levels of VAMP2 and VAMP7 were determined by Western blot analysis after 12-16 h of transfection. (B) Densitometric quantification of VAMP2 and VAMP7 protein levels relative to GAPDH in CTLs that were electroporated with GFP or TeNT-GFP constructs (N=3, ***$p < 0.001$ (Student's t-test)). (C) Human CTLs were co-transfected with either GFP or TeNT-GFP constructs along with granzyme B-mCherry and imaged after 12 h of transfection. Representative live-cell TIRFM images of CTLs that were in contact with anti-CD3 coated coverslips. Fusion events indicated with open arrowheads. (D) Mean percentage of cytotoxic granules fused in cells electroporated with either GFP (n=50) or TeNT-GFP (n=40), $p = 0.704$ (Student's t-test)). (E) Mean average number of granules fused per cell over time in the TIRF plane in cells electroporated with either GFP (n=20) or TeNT-GFP (n=15), $p = 0.939$ (Student's t-test)). Bars indicate mean ± SEM. Scale bar, 5 µm. Adapted from (Chitirala et al., 2019).

3.15 VAMP7 is expressed in CTLs and up-regulated upon activation

All the SNAREs from VAMP1 to 8 were expressed at the mRNA level in primary CD8$^+$ T cells and some VAMPs accumulate at the IS when conjugated with target cells (Pattu et al., 2012). From the TeNT treatment experiment (Figure 23) we could eliminate VAMP1, 2 and 3 as potential v-SNAREs for CG fusion. Further, we activated CTLs with CD3/CD28 beads and checked the expression levels of VAMP2 and VAMP7 proteins with western blot analysis in CTLs from day 0 to day 5. VAMP7 levels were up regulated following activation (N = 3, 100 to 180.08 ± 37.03%), whereas VAMP2 levels were decreased (N = 3, 100 to 46.94 ± 12.83%; Figure 24A & B). Data were normalized to GAPDH and set to 100% on day 0. Taken together, this increase in VAMP7 protein levels upon activation of CTLs suggests that VAMP7 might play an important role in CD8$^+$ T cell function.

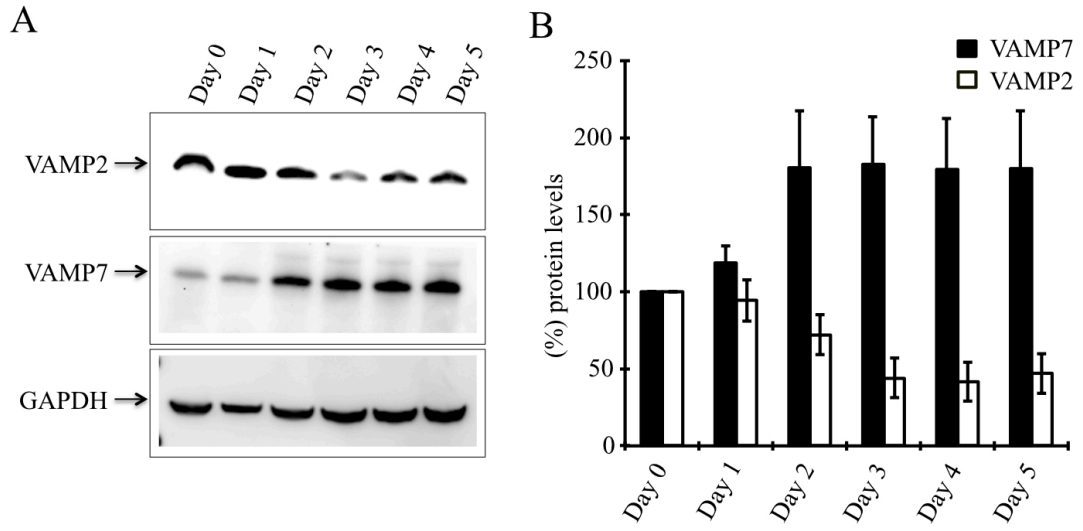

Figure 24: VAMP7 and VAMP2 protein levels after CTL activation over time.
(A) VAMP2 and VAMP7 protein expression in naive and bead-activated CD8$^+$ T cells for the indicated days determined by Western blot analysis. (B) Graphs represent VAMP2 and VAMP7 levels normalized to GAPDH. (N = 3, p = 0.222 (day 1), p = 0.0505 (day 2), p = 0.0142 (day 3), p = 0.0178 (day 4) and p = 0.0274 (day 5); (t-test)). Bars indicate mean ± SEM. Adapted from (Chitirala et al., 2019).

3.16 VAMP7 shows a high degree of co-localization with cytotoxic granules

To examine the localization of VAMPs in primary human CD8$^+$ T cells, we used super-resolution structured illumination microscopy (SIM) with 100 nm resolution in the x, y, and 300 nm in z planes. Because there are only a few paralog-specificvantibodies available, we electroporated EGFP coupled fusion proteins of VAMP3, VAMP4, VAMP7 and mTFP coupled VAMP8 together with the CG marker GzmB coupled with mCherry in primary CTLs derived from human blood (Figure 25A). From the three TeNT-insensitive VAMP isoforms tested, VAMP7 showed the

highest Pearson's coefficient of correlation (0.7 ± 0.02) (Pearson, 1909) and Manders' overlap coefficient (Manders et al., 1993). In contrast, VAMP4 showed little overlap with the CG marker, resulting in Pearson's (0.29 ± 0.02 for VAMP4, 0.22 ± 0.22 for VAMP2 and 0.23 ± 0.02 for VAMP3) and Manders' values (0.4 ± 0.02 for VAMP4 to GzmB, 0.52 ± 0.3 for GzmB to VAMP4, 0.43 ± 0.013 for VAMP2 to GzmB, 0.38 ± 0.026 for GzmB to VAMP2 and 0.33 ± 0.016 for VAMP3 to GzmB, 0.46 ± 0.033 for GzmB to VAMP3) comparable to the TeNT-sensitive VAMP2 and VAMP3 which were used as controls (Figure 25B & C). Previous studies have shown that VAMP8 colocalizes with recycling endosomes and also is responsible for the fusion of Rab11-positive recycling endosomes with the plasma membrane prior to CG fusion (Marshall et al., 2015) and had an intermediate Pearson's coefficient of correlation (0.51 ± 0.033; Figure 25A & B). Since VAMP7 exhibited the highest coefficient of correlation with CGs, we can conclude that VAMP7 is the most likely candidate to mediate CG exocytosis in human $CD8^+$ T cells. To validate this conclusion, we immunostained GzmB with an Alexa 647-conjugated anti-GzmB-specific antibody. This antibody also exhibited a high degree of co-localization with expressed EGFP-VAMP7 or VAMP7-pHuji constructs with a Pearson's coefficient of correlation (0.61 ± 0.02 from EGFP-VAMP7 to GzmB and of 0.62 ± 0.023 from VAMP7-pHuji to GzmB) and a Manders' overlap coefficient (0.70 ± 0.014 from EGFP-VAMP7 to GzmB and 0.75 ± 0.009 from VAMP7-pHuji to GzmB) (Figure 25D-F).

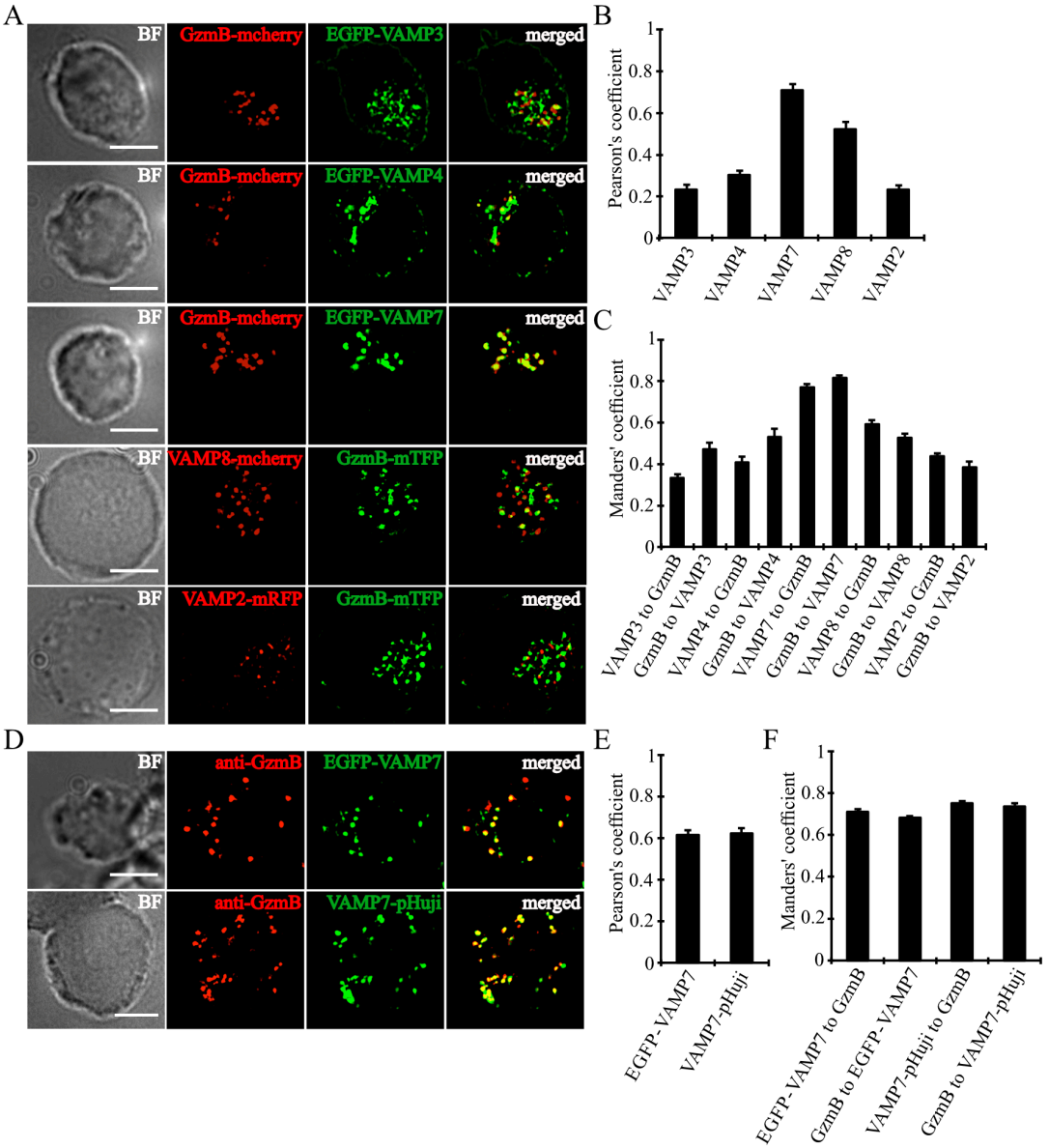

Figure 25: VAMP7 co-localizes with cytotoxic granules significantly.
(A) Bead-activated primry human CD8$^+$ T cells were co-transfected with either GzmB-mCherry or GzmB-mTFP along with the v-SNAREs mVAMP2, VAMP3, VAMP4, VAMP7, and VAMP8 constructs. Representative images from SIM are shown as indicated. Overlay of both channels (red and green) from all VAMPs only VAMP7 showed co-localization with GzmB. (B) Pearson's and (C) Manders' overlap coefficients for co-localization of VAMP3 (n = 16), VAMP4 (n = 14), VAMP7 (n = 13), VAMP8 (n = 9) and VAMP2 (n = 14) with GzmB were given in the text. (D) Bead-activated primary human CD8$^+$ T cells were electroporated with EGFP-VAMP7 or VAMP7-pHuji and immunostained with anti-GzmB antibody conjugated with Alexa647. (E) The corresponding Pearson's and (F) Manders' overlap coefficients for co-localization of EGFP-VAMP7 (n = 12) or VAMP7-pHuji (n = 11) with GzmB were given in the text. Data were from three different donors. Data indicateed were mean ± SEM. Scale bar, 5 µm. Adapted and modified from (Chitirala et al., 2019).

3.17 VAMP7 does not colocalize with Lat-containing vesicles in either activated or resting CTLs

It was shown previously in primary mouse $CD4^+$ T cells that VAMP7 plays an important role in the initial phase of IS formation by regulating the recruitment and phosphorylation of Lat (linker for activation of T cells), a key adaptor protein involved in the T cell receptor signaling pathway. With confocal and TIRF microscopy it was shown that Lat and VAMP7 partially co-localize on vesicles close to the IS. (Larghi et al., 2013a). We, therefore, tested a potential co-localization of Lat and VAMP7 in human primary $CD8^+$ T cells by structured-illumination microscopy (SIM). CTLs were electroporated with VAMP7-mCherry and after 12 h of transfection cells were incubated either on poly L-ornithine or CD3/CD28 coated coverslips and stained with anti-Lat antibody (Figure 26A). We found basically no co-localization either on poly-L-ornithine or CD3 coated coverslips. The Pearson's coefficients of correlation of (0.03 ± 0.006 on poly L-ornithine or 0.08 ± 0.008 on CD3/CD28; Figure 26B) and Manders' overlap coefficients for co-localization (0.20 ± 0.026 for VAMP7 to Lat, 0.06 ± 0.023 for Lat to VAMP7 on poly L-ornithine, 0.19 ± 0.034 for VAMP7 to Lat, 0.11 ± 0.03 for Lat to VAMP7 on CD3/CD28; Figure 26C) rule out that VAMP7 is associated with Lat containing vesicles at resting or activated human primary $CD8^+$ T cells.

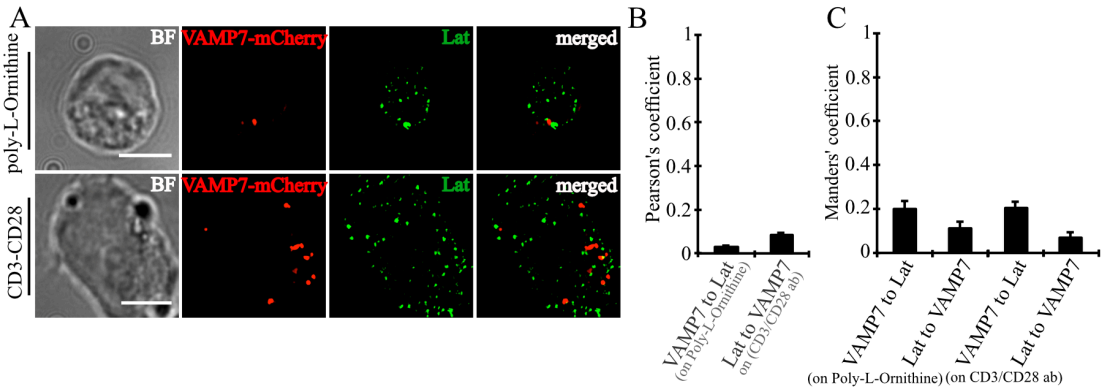

Figure 26: VAMP7 does not localize with Lat-vesicles in $CD8^+$ T cells.
(A) Bead-activated primary human $CD8^+$ T cells expressed with a VAMP7-mCherry construct and incubated either on poly-L-ornithine or anti-CD3 coated coverslips for 15 min. Cells were fixed and immunostained with anti-Lat antibody. (B) The relative Pearson's and (C) Manders' overlap coefficients for co-localization of VAMP7-mCherry with Lat on Poly-L-Ornithine coated coverslips (n=11) or CD3-CD28 coated coverslips (n=10) were given in the text. Data indicated were mean ± SEM. Scale bar, 5 µm. Adapted and modified from (Chitirala et al., 2019).

3.18 Lat-containing vesicles do not show co-localization in primary mouse CD4+ T cells

Further, we also looked at the localization of VAMP7 in CD3/CD28 bead stimulated mouse CD4+ T cells on day 3 by transfecting with huVAMP7-mCherry. Subsequently cells were incubated on poly L-ornithine or CD3-CD28 coated coverslips for 15 min, fixed and immunostained with anti-Lat antibody (Figure 27A). In CD4+ T cells, we did not observe any significant co-localization of VAMP7 with Lat-containing vesicles with Pearson's (0.04 ± 0.01 on poly L-ornithine and 0.02 ± 0.006 on CD3/CD28; Figure 27B) and Manders' co-localization coefficients (0.24 ± 0.02 on poly L-ornithine and 0.24 ± 0.01 on CD3/CD28; Figure 27C).

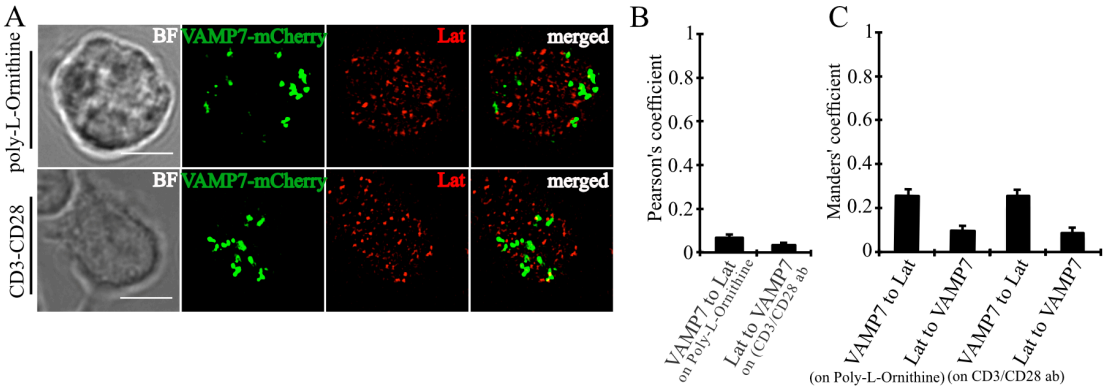

Figure 27: Localization of VAMP7 with Lat-containing vesicles in mouse primary CD4+ T cells.
(A) Bead-activated mouse primary $CD4^+$ cells electroporated with VAMP7-mCherry construct and incubated either on poly-L-ornithine or anti-CD3 coated coverslips for 15 min, fixed and immunolabeled with anti-Lat antibody. (B) The corresponding Pearson's and (C) Manders' overlap coefficients for co-localization of VAMP7-mCherry with Lat on Poly-L-Ornithine coated coverslips (n = 12) or anti-CD3 coated coverslips (n = 11) were given in the text. Data were indicated as mean ± SEM. Scale bar, 5 µm.

3.19 Phosphorylation of the MAP kinases Erk1 and Erk2 is unaltered upon VAMP7 Knockdown

In order to confirm that VAMP7 in primary human $CD8^+$ T cells is not involved in the T cell signaling pathway, we tested the phosphorylation of the kinases Erk1 and Erk2 upon VAMP7 knockdown. In accordance with the lack of co-localization with Lat containing vesicles (Figure 28B & C), we also found no change in the phosphorylation of the microtubule-associated protein (MAP) kinases Erk1 and Erk2 upon VAMP7 knockdown in Western blots with a phospho-specific antibody used at the indicated time points compared to ns-siRNA treated cells (Figure 28A & C). VAMP7 protein levels were decreased >90 % upon VAMP7 siRNA1 and 2 compared to ns siRNA treated CTLs (Figure 28B). We thus conclude that VAMP7 has no influence on the Lat signalosome in primary human $CD8^+$ T cells.

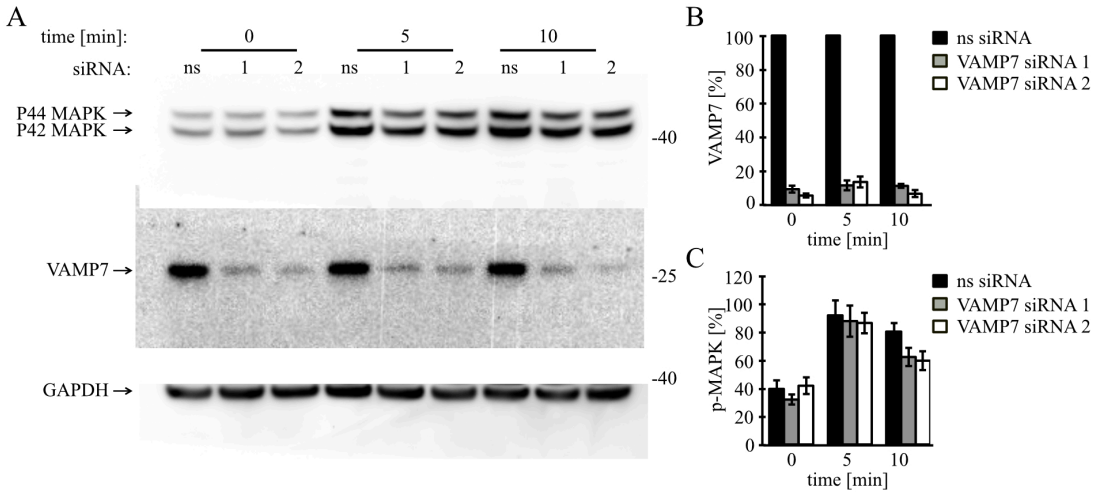

Figure 28: Phosphorylation of MAP kinases Erk1 and Erk2 are unchanged upon VAMP7 knockdown.
(A) Lysates from Bead-activated primary human CTLs electroporated with either control or siRNA1 or siRNA2 against VAMP7 and activated for 0, 5 or 10 min with a monoclonal antibody (mAb) against CD3 and CD28 and blotted for p-MAPK (top), VAMP7 (middle) and GAPDH (bottom) as the loading control. (B) Densitometric quantification of VAMP7 protein levels in % normalized to control siRNA-treated CTLs. Data were obtained from five independent experiments (for siRNA1, N = 5; ***p < 0.001 and for siRNA2, N = 5; ***p < 0.001 (t-test)). (C) The mean intensity values for phosphorylated MAPK were calculated by western blot analysis which were normalized to GAPDH and displayed relative to that of unstimulated cells expressing control siRNA (N = 5; 0 min, p = 0.417; 5 min, p = 0.651; 10 min, p = 0.088 (One-way ANOVA test). Bars indicated were means ± SEM. Adapted from (Chitirala et al., 2019).

3.20 VAMP7 polarizes to the IS on the same granules as granzyme B and Perforin

We performed our initial co-localization analysis on CD3/CD28 bead stimulated primary human CTLs that were not conjugated with target cells. To examine whether VAMP7 co-localizes with GzmB and Perforin at the time of IS formation when contacted with target cells, we performed on the CTLs after electroporating with a VAMP7-pHuji construct and observed them using SIM microscopy. After 12 h of transfection CTLs were incubated with Raji (target cell line) cells for 5, 10 and 15 min respectively. After fixing, the cells were stained with alexa 647-conjugated anti-GzmB (Figure 29A left) or anti-Perforin antibodies (Figure 29A right), respectively. From these experiments, we noticed that CTLs in contact with target cells showed a strong CG polarization towards the IS as expected. Importantly, in both GzmB and Perforin immunostainings we found a highly significant co-localization of VAMP7 puncta with the GzmB or Perforin at each indicated time point measured, with Pearson's coefficients of correlation of 0.58 ± 0.03 (5 min), 0.59 ± 0.03 (10 min) and 0.60 ± 0.02 (15 min) for GzmB (Figure 29B) and 0.46 ± 0.03 (5 min), 0.49 ± 0.03 (10 min) and 0.52 ± 0.03 (15 min) for Perforin (Figure 29C), respectively.

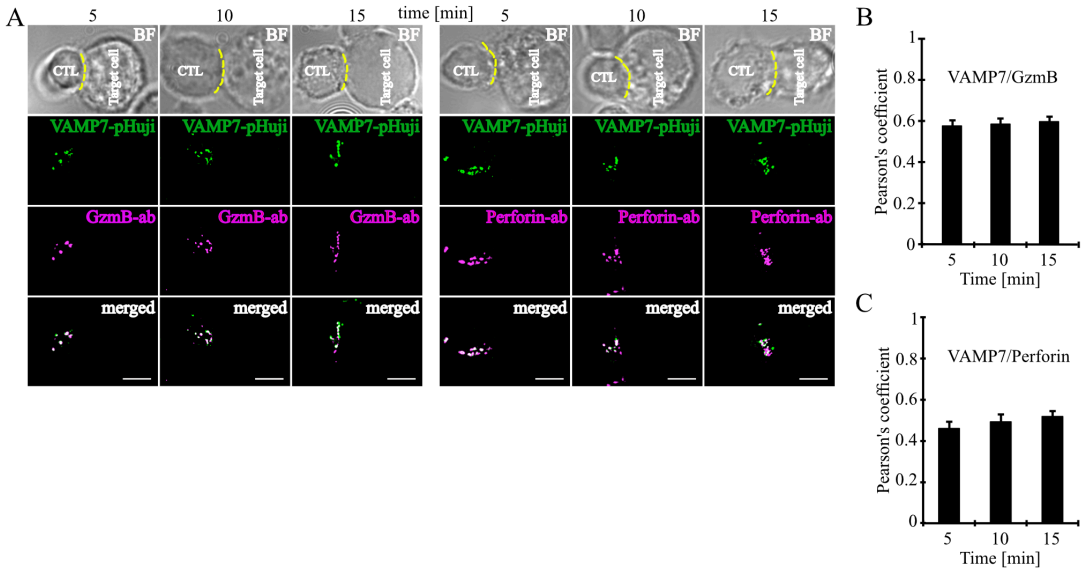

Figure 29: VAMP7 polarizes to the IS along with CG merkers GzmB and Perforin.
(A) Representative SIM images from *staphylococcus* enterotoxin-A (SEA)-pulsed human $CD8^+$ T cells electroporated with VAMP7-pHuji construct (green) and conjugated with SEA pulsed RAJI (target) cells, fixed after indicated time points respectively. CTLs were fixed, permeabilized and immunostained with either Alexa647-conjugated GzmB (magenta) or Perforin (magenta) antibodies. (B, C) The corresponding Pearson's overlap coefficients for co-localization of VAMP7-pHuji with GzmB (n = 12) and VAMP7-pHuji with Perforin (n = 11) were given in the text. Data indicated were means ± SEM. Scale bar, 5 µm. Adapted from (Chitirala et al., 2019).

3.21 VAMP2, VAMP3 and VAMP4 show no co-localization with GzmB and Perforin

We tested the localization of other v-SNAREs such as VAMP2, VAMP3, and VAMP4 in CTLs conjugated with Raji target cells. After SEA pulsation primary CD8+ T cells were electroporated with either VAMP2-pHuji or EGFP-VAMP3 or EGFP-VAMP4 fusion constructs. After 12-16 h of transfection, CTLs were conjugated with SEA pulsed Raji target cells for 15 min at 37° C. After fixation, cells were immunostained with Alexa 647-conjugated GzmB (Figure 30A left) or Perforin (Figure 30A right) antibodies. We did not observe any significant co-localization of VAMP2, VAMP3 and VAMP4 puncta with cytotoxic granule markers at the indicated time point measured, with Pearson's coefficients of correlation of 0.31 ± 0.009 (15 min), 0.20 ± 0.012 (15 min) and 0.27 ± 0.013 (15 min) for GzmB (Figure 30B left) and 0.24 ± 0.009 (15 min), 0.18 ± 0.014 (15 min) and 0.21 ± 0.024 (15 min) for Perforin (Figure 30C right), respectively. In contrast to VAMP7 (see Figure 29), VAMP2, 3 and 4 were not involved in CG polarization during IS formation.

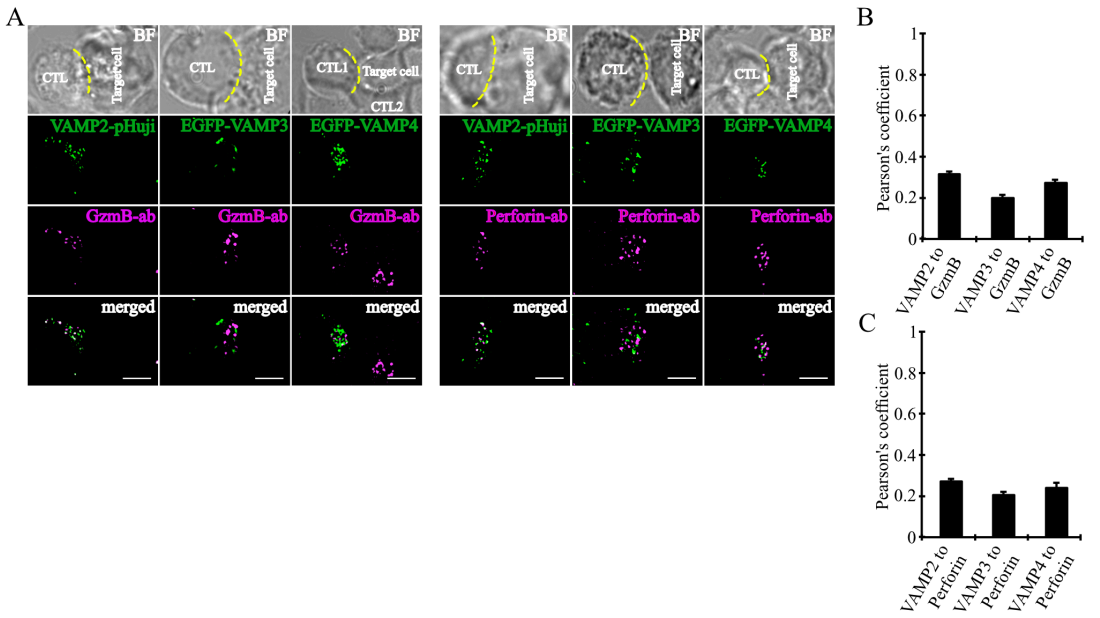

Figure 30: VAMP2, 3 and 4 do not polarize to the IS on the same granules as GzmB and Perforin.
(A) Representative SIM images of SEA-pulsed human CD8⁺ T cells that were electroporated with mVAMP2-pHuji, EGFP-VAMP3, and EGFP-VAMP4 constructs (green) respectively and conjugated with SEA pulsed RAJI (target) cells and fixed after 15 min. Permeabilized cells were further immunostained with either Alexa647-conjugated GzmB (magenta) or Perforin (magenta) antibodies. (B) & (C) The corresponding Pearson's overlap coefficients for co-localization of mVAMP2, VAMP3, and VAMP4 with GzmB (n = 15) or Perforin (n = 16) were given in the text. Data indicated were means ± SEM. Scale bar, 5 µm. Adapted from (Chitirala et al., 2019).

3.22 VAMP7 fuses at the plasma membrane together with GzmB

With the help of immunostainings and SIM microscopy, we demonstrated that VAMP7 is localized on CGs in bead activated and target cell conjugated CTLs. To test whether fusion of VAMP7 occurs concurrently with the release of cytotoxic substances (GzmB and Perforin) from CGs, we next performed TIRFM experiments at high temporal resolution (10 Hz). We co-transfected primary human CD8⁺ T cells with VAMP7 fused to a red fluorophore mCherry and GzmB fused to TFP (teal fluorescent protein) (Ai et al., 2006) constructs. After carefully adding CTLs on CD3-coated coverslips the IS was formed quickly (within 1-2 min) and we noticed a rapid arrival and accumulation of CGs, indicated by individual VAMP7-mCherry (magenta) puncta (Figure 31A upper panel) and GzmB-TFP (green) puncta (Figure 31A middle panel). In conjunction with the data from (Figure 25 & Figure 29), the merged image showed an almost complete co-localization of VAMP7 with GzmB (Figure 31A lower panel). We identified individual fusion events which were analysed by a sudden drop in the mean fluorescence intensity of both VAMP7-mCherry and GzmB-TFP fluorescence simultaneously, due to the release

and followed by diffusion of the soluble GzmB-TFP (compare frame 3 and 4 in the upper panel of Figure 31A). The percentage of cells with fusion events (25.55 ± 6.18 %; Figure 31B) and the average number of fusion events per cell (3.66 ± 0.83; Figure 31C) were calculated from three independent experiments.

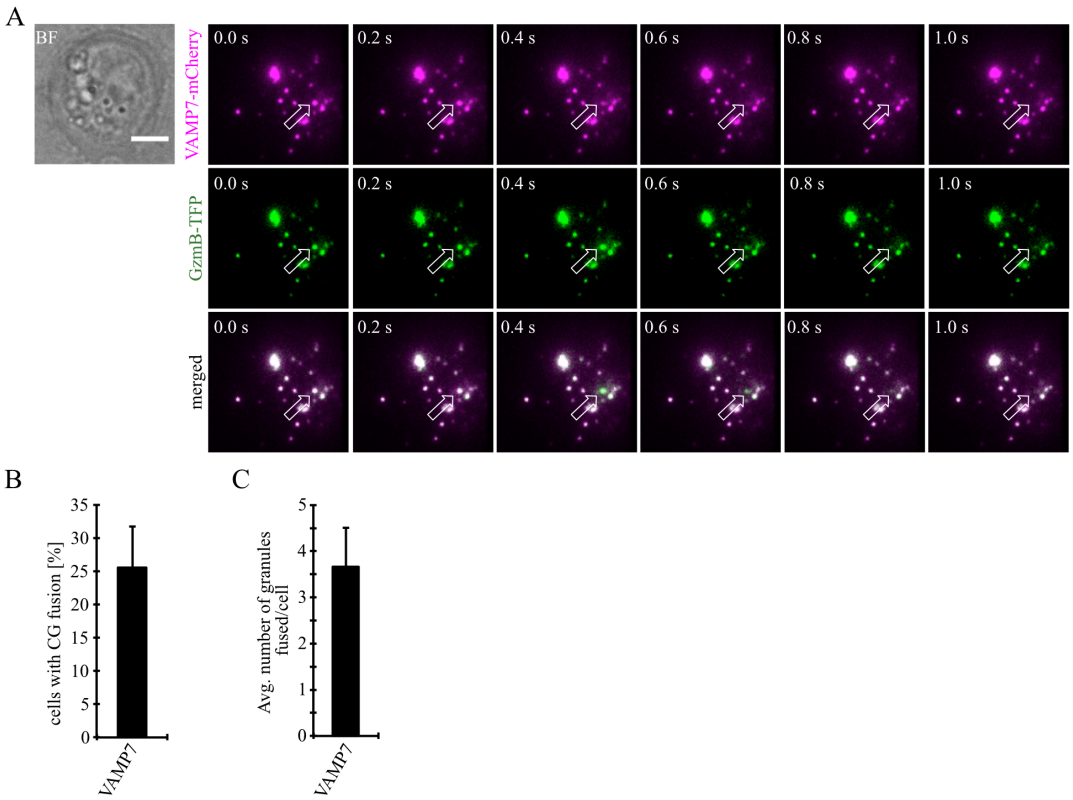

Figure 31: VAMP7 fuses at the plasma membrane together with GzmB.
(A) Bead stimulated human CD8$^+$ T cells were co-transfected with VAMP7-mCherry and GzmB-TFP fusion constructs and imaged after 12 h of electroporation. Selected live-cell TIRF microscopy images of VAMP7-mCherry (magenta) and GzmB-TFP (green) in an electroporated CTL that was in contact with an anti-CD3 coated coverslip was shown. Fusion events were indicated with open arrowheads. (B) Mean percentage of cells with fusion events (n = 29) and (C) Mean average number of granules fused over time in the TIRF plane per cell (n = 29) from three different donors were indicated. Bars indicated were means ± SEMs. Scale bar, 5 µm. Adapted and modified from (Chitirala et al., 2019).

3.23 VAMP7 fuses at the plasma membrane along with GzmB: visualization with pH-sensitive red fluorescent protein pHuji

After demonstrating that VAMP7 ‘’fuses’’ simultaneously with the release of GzmB from CGs, we changed the fluorophore on VAMP7 to a pH-sensitive red fluorescent protein, pHuji (Shen et al., 2014) to distinguish the fusion kinetics of membrane protein (VAMP7) and diffusible cargo protein (GzmB). As previously, we used TIRFM microscopy to perform these experiments. We co-transfected human CTLs with VAMP7 coupled to the pH-sensitive fluorophore pHuji at C-terminus and GzmB coupled to mTFP. CTLs were seeded on anti-CD3 coated coverslips. The IS was formed quickly with a rapid accumulation of CGs that were indicated by individual GzmB-mTFP (green) and VAMP7-pHuji (magenta) puncta (Figure 32A

upper panels). In accordance with the data in (Figure 25 & Figure 29), the merged images showed an almost complete co-localization of vSNARE VAMP7 with the CG marker GzmB (white puncta in Figure 32A lower panel). We identified individual fusion events by a sudden drop in the mean fluorescence intensity of GzmB-mTFP (Figure 32B), caused by the release and subsequent diffusion of the soluble GzmB-mTFP (compare frame 3 and 4 in the upper panel of Figure 32A). Parallel to this, we observed a sudden increase in fluorescence of VAMP7-pHuji that is due to the opening of the fusion pore and subsequent dequenching of the luminal fluorophore (Figure 32A; exemplary trace in Figure 32C). The magenta fluorescence remained after fusion as expected. These data not only showed VAMP7s' selective localization on CGs before their fusion but also verifies the proteins' integration into the CG membrane in the correct direction. From this data, we could distinguish the fusion of VAMP7 and release of GzmB simultaneously with different fusion kinetics.

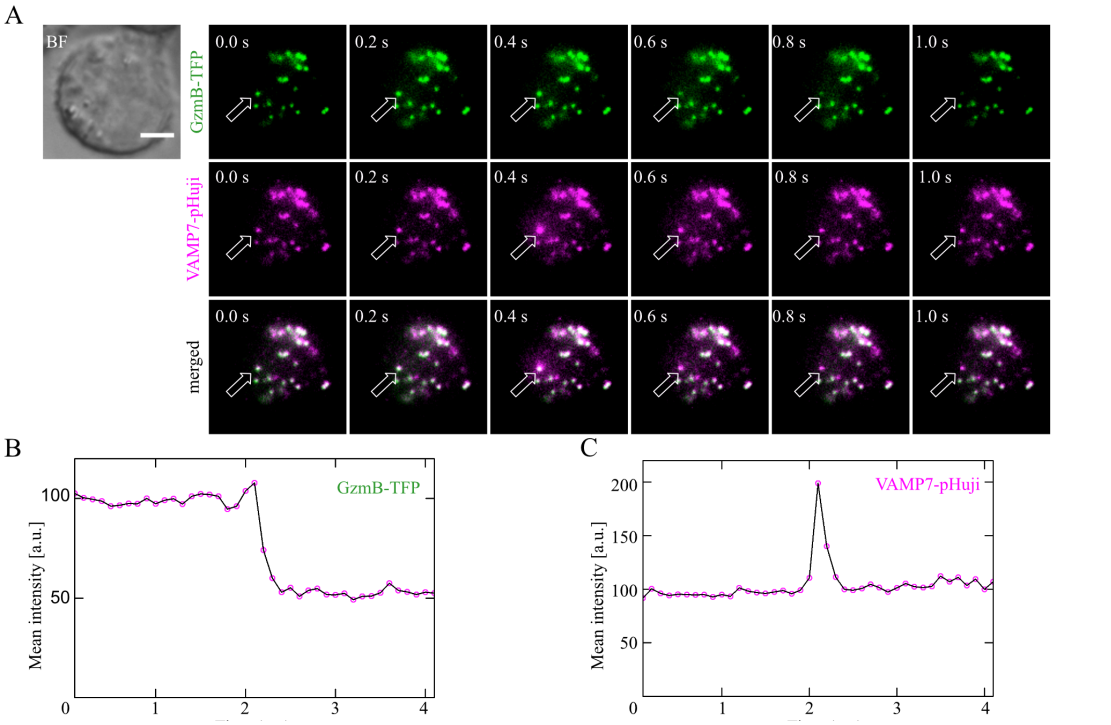

Figure 32: Visualization of VAMP7-pHuji fusion at the plasma membrane together with GzmB-mTFP.
(A) Bead stimulated human CTLs were co-transfected with GzmB-mTFP and VAMP7-pHuji constructs and were imaged after 12 h of transfection. Selected live-cell TIRFM images of GzmB-mTFP and VAMP7-pHuji from an electroporated CTL which is in contact with an anti-CD3 coated coverslip were shown (GzmB, green, upper panel; VAMP7, magenta, middle panel; merged, lower panel). (B & C) Graphs depicted were the mean fluorescence intensity of individual mTFP and pHuji vesicles over time, respectively. Experiments were performed with three individual donors (n = 15 cells). Scale bar, 5 µm. Adapted and modified from (Chitirala et al., 2019).

3.24 VAMP8 mediates recycling endosomal fusion whereas VAMP7 mediates CG fusion

Immunoprecipitations, pulldowns and in-vitro cell fusion assays from primary human $CD8^+$ T cells led to the hypothesis that VAMP8 plays an important role in CTL cytotoxicity by mediating multiple membrane trafficking steps during cytotoxic granule maturation and exocytosis (Spessott et al., 2017b). Our data (Figure 25) also showed an intermediate Pearson's coefficient of correlation of VAMP8 with GzmB and previously, our group showed that VAMP8 is required for fusion of Rab11 containing recycling endosomes with the plasma membrane (the key step before CG exocytosis) in primary human $CD8^+$ T cells. The t-SNARE, Syntaxin11 was deposited at the plasma membrane by recycling endosomes to help assembling SNARE complexes that are required for cytotoxic granule exocytosis at the plasma membrane (Marshall et al., 2015). Thus, we did TIRF experiments after co-transfection of VAMP7-mCherry and VAMP8-mTFP constructs in human $CD8^+$ T cells to verify the role of VAMP8. If VAMP8 is involved in the final fusion step of CGs with the plasma membrane (Dressel et al., 2010; Loo et al., 2009), we expect a co-localization of both VAMP isoforms at the IS. In agreement with the co-localization data of GzmB with different isoforms of VAMP (Figure 25A-C), in which VAMP7 and VAMP8 proteins were localized on different vesicles, there was virtually no co-localization at the IS. During IS formation, VAMP8-containing vesicles arrived much earlier at the IS (green puncta) (Figure 33A) and fused earlier with ten-fold higher frequency than VAMP7-containing vesicles (red puncta) (Figure 33B-D). This result confirmed our earlier findings (Marshall et al., 2015) and rules out a role of VAMP8 in the fusion of CGs with the plasma membrane in primary human $CD8^+$ T cells.

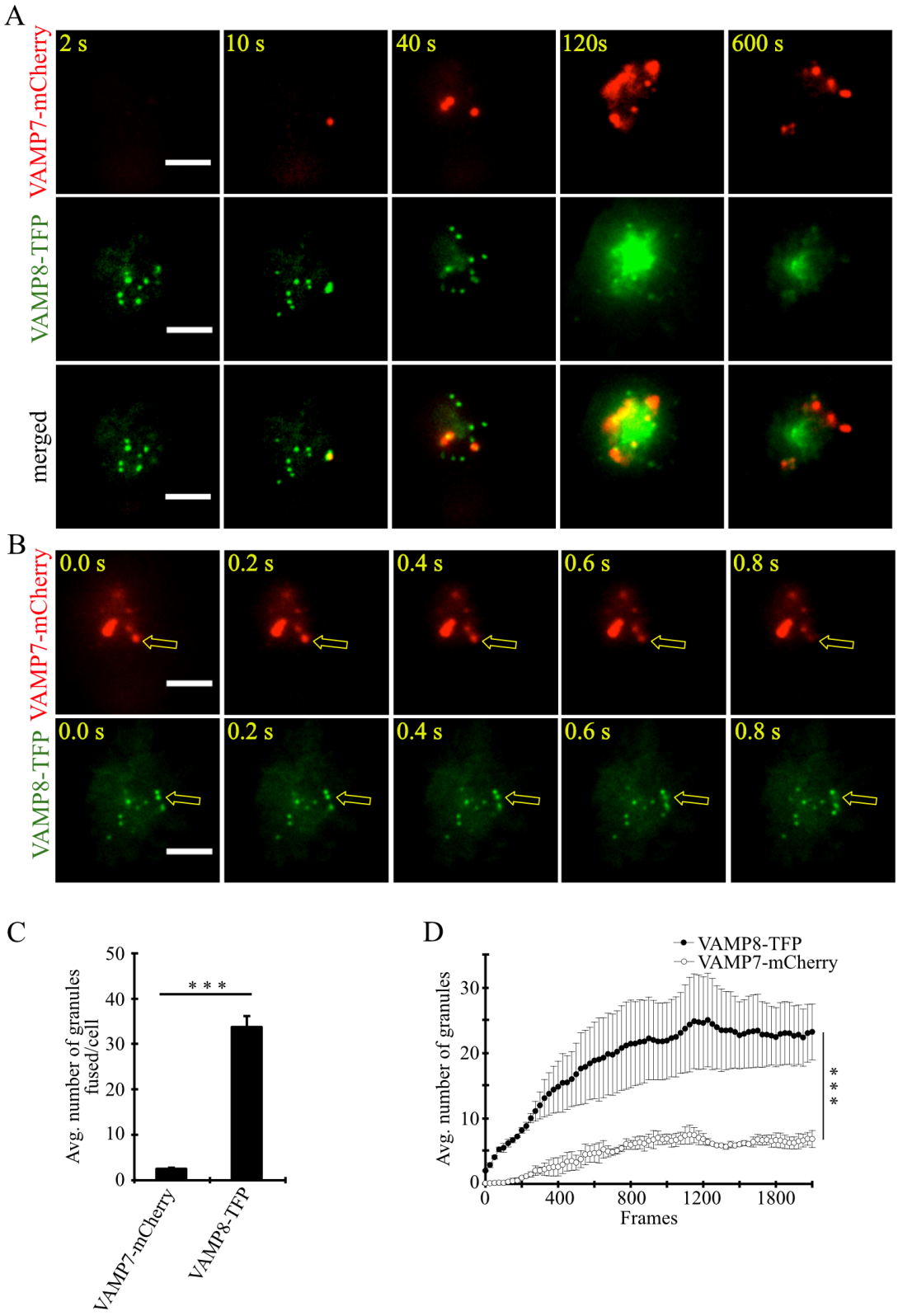

Figure 33: VAMP8 and VAMP7-containing vesicle fusion at the IS.
(A) Bead activated human CTLs were co-transfected with VAMP7-mCherry and VAMP8-mTFP constructs and imaged after 12 h of transfection. Selected live-cell TIRFM images of VAMP7-mCherry and VAMP8-mTFP from an electroporated CTL which is in contact with an anti-CD3 coated coverslip (VAMP7, red, upper panel; VAMP8, green, middle panel; merged, lower panel). (B) Individual fusion events (arrows) of VAMP7- (upper panel) and VAMP8-containing vesicles (lower panel) at the indicated time points of recording were shown from representative cell. (C) Mean cumulative fusion events in the TIRF plane per cell (N = 3, n = 39, ***p < 0.001

(t-test)). (D) Mean average number of VAMP7- and VAMP8-containing vesicles in the TIRF plane per cell in the first 3.5 minutes of measurements were displayed (N = 3, n = 39, ***p < 0.001 (Mann-Whitney U-test)). Bars indicated were means ± SEMs. Scale bar, 5 µm. Adapted and modified from (Chitirala et al., 2019).

3.25 Knockdown of VAMP7 strongly reduces fusion of cytotoxic granules at the IS

Our data demonstrate that VAMP7 co-localizes with the GzmB and Perforin until CGs fuse with the plasma membrane at the IS. To investigate the functional involvement of VAMP7 in the fusion of CGs with the plasma membrane, we carried out TIRFM experiments after down-regulating VAMP7 protein. We electroporated human $CD8^+$ T cells with two different VAMP7 siRNAs (siRNA1 and 2) and with GzmB-mCherry. VAMP7 siRNA1 and 2 reduced the expression of VAMP7 to 10.5 ± 3.9% (VAMP7 siRNA1) and 8.5 ± 1.9% (VAMP7 siRNA2) of the original level, respectively (Figure 34A & B) in contrast to a scrambled control siRNA which had no effect. We observed a reduction in the number of CTLs showing CG fusion to less than 50% of the control after expressing VAMP7 siRNAs (from 57.8 ± 4.8% to 22.2 ± 4.4% for VAMP7 siRNA1 and from 67.1 ± 1.8% to 14.4 ± 3.4% for VAMP7 siRNA2, respectively; Figure 34D). Simultaneously, the average number of CG fusion events observed in CTLs expressing VAMP7 siRNAs was also reduced (from 2.8 ± 0.7 to 1.6 ± 0.4 for VAMP7 siRNA1 and from 3.2 ± 0.2 to 0.9 ± 0.4 for VAMP7 siRNA2, respectively; Figure 34E). As a second independent assay we used recently developed calcein-based killing assay to measure the CG release from CTLs. we used a recently developed, calcein-based killing assay (Kummerow et al., 2014) to measure the CG release from CTLs. For that, we used $CD8^+$ T cells isolated from SEA pulsed PBMCs and SEA pulsed Raji (target) cells that were incubated for 4 h at 37 °C at 1 to 10 (Target to T cell ratio). Prior to the assay, target cells were incubated with calcein-AM dye. In agreement with our TIRF data, after 4 h of incubating T cells with target cells, we observed a significant reduction of killing of targets in CTLs electroporated with VAMP7 siRNA1 (20.7 ± 2.1 %) and VAMP7 siRNA2 (16.6 ± 3.0 %) compared to scrambled siRNA treated cells (52.04 ± 3.6 %) (Figure 34F).

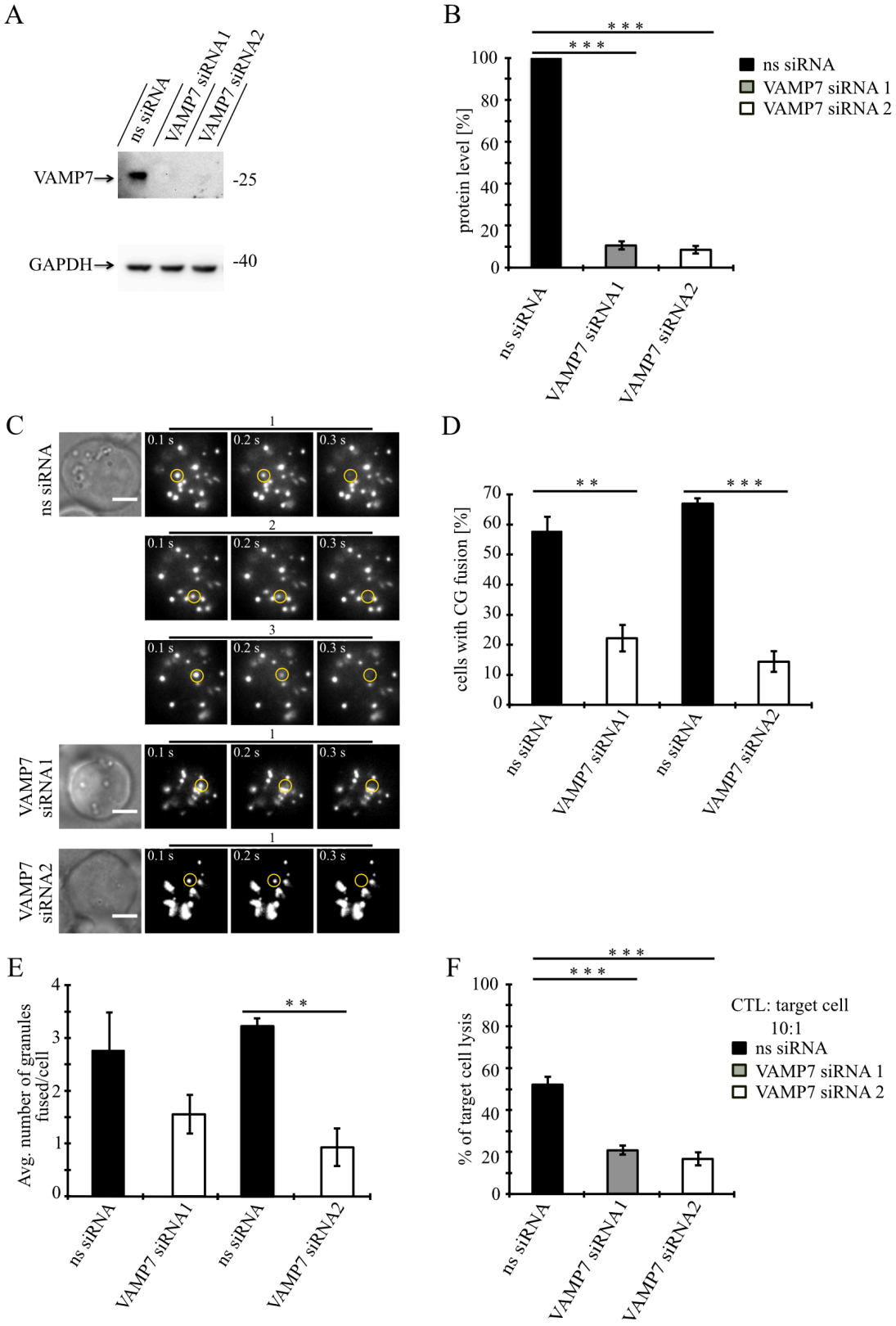

Figure 34: VAMP7 knockdown strongly decreases the cytotoxic granule fusion at the IS. (A) Lysates from bead stimulated human CD8⁺ T cells electroporated with either control or VAMP7 siRNA1 or 2, respectively and blotted for VAMP7 (top) and GAPDH (bottom) as the loading control. (B) Quantification of VAMP7 protein levels (in % normalized to control siRNA-treated CTLs) performed by densitometry (VAMP7-siRNA1, N = 3; ***p < 0.001 and VAMP7-siRNA2, N = 3; ***p < 0.001 (t-test)). (C) Primary human CD8⁺ T cells were co-transfected with

GzmB-mCherry along with either ns-siRNA or VAMP7-siRNA1 or 2 and imaged 12 h after transfection. Selected live-cell TIRF microscopy images of GzmB-mCherry in an electroporated CTL in contact with an anti-CD3 coated coverslip were shown. Fusion events were indicated with open circles (three frames shown per granule fused). (D) Mean percentage of cytotoxic granules fused in cells electroporated with either ns-siRNAs (n=66 and n = 59, respectively) or VAMP7-siRNA1 (n = 91; **p < 0.01 (t-test)) or VAMP7-siRNA2 (n = 72; ***p < 0.001 (t-test)). (E) Mean average number of granules fused over time in the TIRF plane per cell (p = 0.206 (t-test) for VAMP7-siRNA1 and **p < 0.01 (t-test) for VAMP7-siRNA2. (F) Calcein-based killing assay performed in primary $CD8^+$ T cells electroporated with ns-siRNA, VAMP7-siRNA1 or VAMP7-siRNA2. Experiments were carried out in duplicates from four donors (N = 4; ***p < 0.001 (t-test)). Bars indicated were means ± SEM. Scale bar, 5 µm. Adapted from (Chitirala et al., 2019).

3.30 VAMP4 knockdown has no effect on fusion of cytotoxic granules at the IS

In an NK cell line (YTS), it was demonstrated that VAMP4 and VAMP7 were associated with Perforin containing cytotoxic granules when YTS cells conjugated with target cells (Krzewski et al., 2011b). siRNA mediated downregulation of VAMP4 resulted in a significant reduction in degranulation but did not influence IFN-γ secretion. To test the effect of VAMP4 on CG fusion, we observed cytotoxic granule exocytosis. We performed TIRFM in primary human CTLs co-transfected with VAMP4 siRNA together with GzmB-mCherry as CG marker for visualizing exocytosis. Knockdown of VAMP4 was very efficient compared to ns-siRNA treated cells and was confirmed by semi-quantitative PCR, which showed much less expression of VAMP4 cDNA (11.85 ± 2.73 %) compared to ns-siRNA treated cells (Figure 35B). In agreement with the results from (Figure 35A-C), we did not observe any difference in the percentage of cells showing secretion in VAMP4 siRNA treated cells (52.62 ± 1.35 %) in comparison to ns siRNA treated cells (52.61 ± 1.77 %) or in the average number of granules fusing per cell in VAMP4 siRNA treated cells (2.79 ± 0.47) in comparison to ns siRNA treated cells (3.84 ± 0.36) (Figure 35C & D). These results indicate that VAMP4 has no role in CG exocytosis in primary human $CD8^+$ T cells.

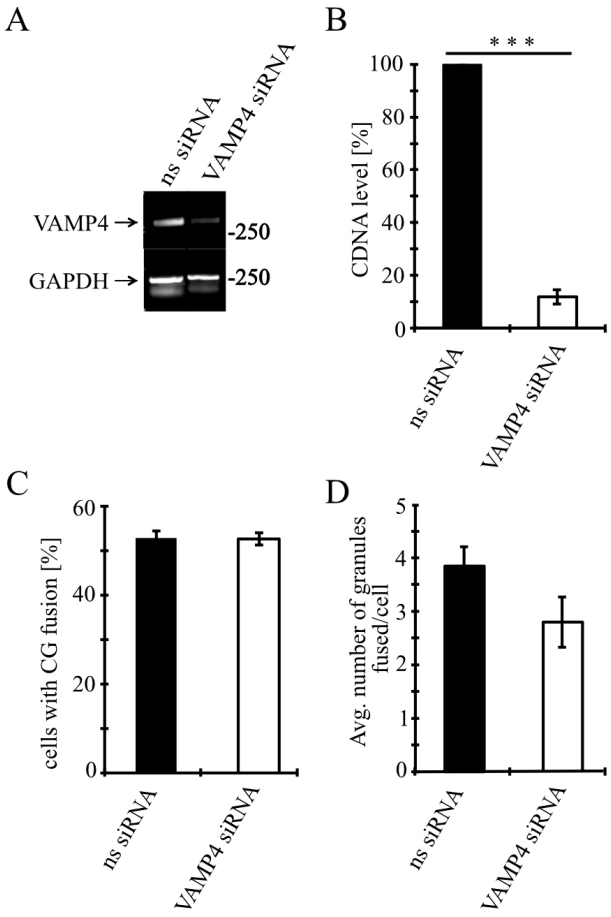

Figure 35: Knockdown of VAMP4 has no effect on the fusion of cytotoxic granules at the IS.
(A) Bead-activated primary human CD8$^+$ T cells electroporated with ns-siRNA or siRNA against VAMP4 as indicated. The bands on agarose gel show VAMP4 cDNA levels after 12 h of transfection by semi-quantitative PCR. (B) VAMP4 cDNA levels quantified by densitometry normalized to GAPDH (N = 3, ***p < 0.001; (t-test)) from three independent experiments. (C) The mean percentage of cytotoxic granule fusion in cells electroporated with either ns-siRNA (n = 82) or VAMP4-siRNA1 (n = 53) (N = 3, p = 0.997; (t-test)) are shown. (D) Mean average number of granules fused over time in the TIRF plane per cell for ns-siRNA (n = 82) and VAMP4-siRNA1 (n = 53) (N = 3, p = 0.154; (t-test)). Bars indicate ± SEMs. Adapted from (Chitirala et al., 2019).

3.31 VAMP7 knockdown has no effect on fusion of recycling endosomes

We then tested recycling endosomes fusion (VAMP8 mediated), which usually occurs before CG fusion at the IS (Marshall et al., 2015) by co-transfecting human CD8+ T cells with siRNA against VAMP7 and Rab11a (a marker for recycling endosomes) fused to GFP. TIRFM analysis of these cells showed no difference in the percentage of CTLs with recycling endosome fusion of VAMP7 siRNA treated CTLs (48.6 ± 4.9 %) or ns siRNA treated CTLs (52.3 ± 3.06 %), nor was there a difference in the average number of recycling endosomal fusion events per cell in

VAMP7 siRNA treated CTLs (9.70 ± 1.88) when compared to ns siRNA (6.9 ± 0.6) (Figure 36A & B).

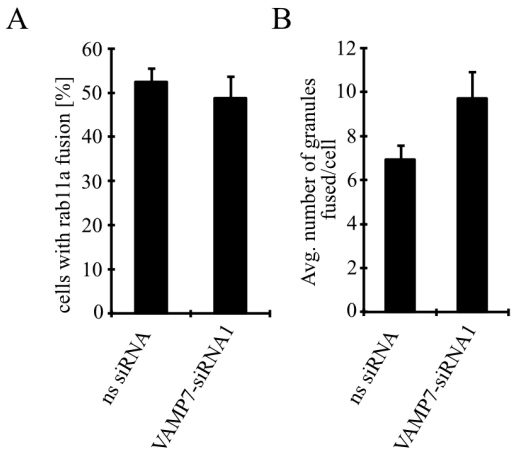

Figure 36: Rab11a fusion at the plasma membrane is unchanged upon VAMP7 knockdown.
(A) Bead stimulated primary human $CD8^+$ T cells co-transfected with mCherry-Rab11a construct either with ns-siRNA or VAMP7-siRNA1 and imaged after 12 h of electroporation. Mean percentage of cytotoxic granules fused in cells electroporated with VAMP7-mCherry for ns-siRNA (n = 44) and VAMP7-siRNA1 (n = 46) (N = 3, p = 0.558; (t-test)) (B) Mean average number of granules fused over time per cell in the TIRF plane for ns-siRNA (n = 44) and VAMP7-siRNA1 (n = 46) (N = 3, p = 0.107; (t-test)). Data were pooled from three different donors. Bars indicated were means ± SEMs. Adapted from (Chitirala et al., 2019).

3.32 VAMP7 forms a SNARE complex with Syntaxin11 and SNAP-23

Having identified VAMP7 as the V-SNARE in the fusion of CGs with the plasma membrane at the IS, we have examined which additional SNAREs are involved in the CG fusion event. In general, fusion processes are mediated by a SNARE complex consisting of a vesicular SNARE (v-SNARE) residing on the vesicular membrane and target SNAREs (t-SNAREs) on the target membrane (
Figure 37A). We attempted to identify the corresponding SNARE partners of VAMP7. For that purpose, we generated Twin-Strep-tag tagged fusion proteins for VAMP7 at the C-terminus (VAMP7-Flag-Twin-Strep-tag) and Twin-Strep-tag tagged Syntaxin11 at the N-terminus (Twin-Strep-tag-Syntaxin11;
Figure 37B) attached with a flexible linker (GGSGGSGGS) and expressed these constructs in human CTLs. Pull-downs assays performed with human CTLs overexpressing tagged VAMP7-Strep-tag identified a specific band for both SNAP-23 and Syntaxin11 proteins. This data indicates that SNAP-23 and Syntaxin11 were the most likely t-SNARE partners for VAMP7 (
Figure 37C). Conversely, lysates of CTLs expressing tagged Syntaxin11 showed SNAP-23 and VAMP7 in pulled down assay (
Figure 37D). Importantly, VAMP2 was not detected in the pull-down assays, demonstrating the specificity of the SNARE complex we identified (

Figure 37D). We also analysed the amount of SNARE proteins pulled down with the respective Twin-Strep-tag pulldown assays (
Figure 37E & F). In conclusion, these results indicate that SNAP-23 and Syntaxin11 are t-SNARE partners for CG fusion mediated by VAMP7 in primary $CD8^+$ T cells.

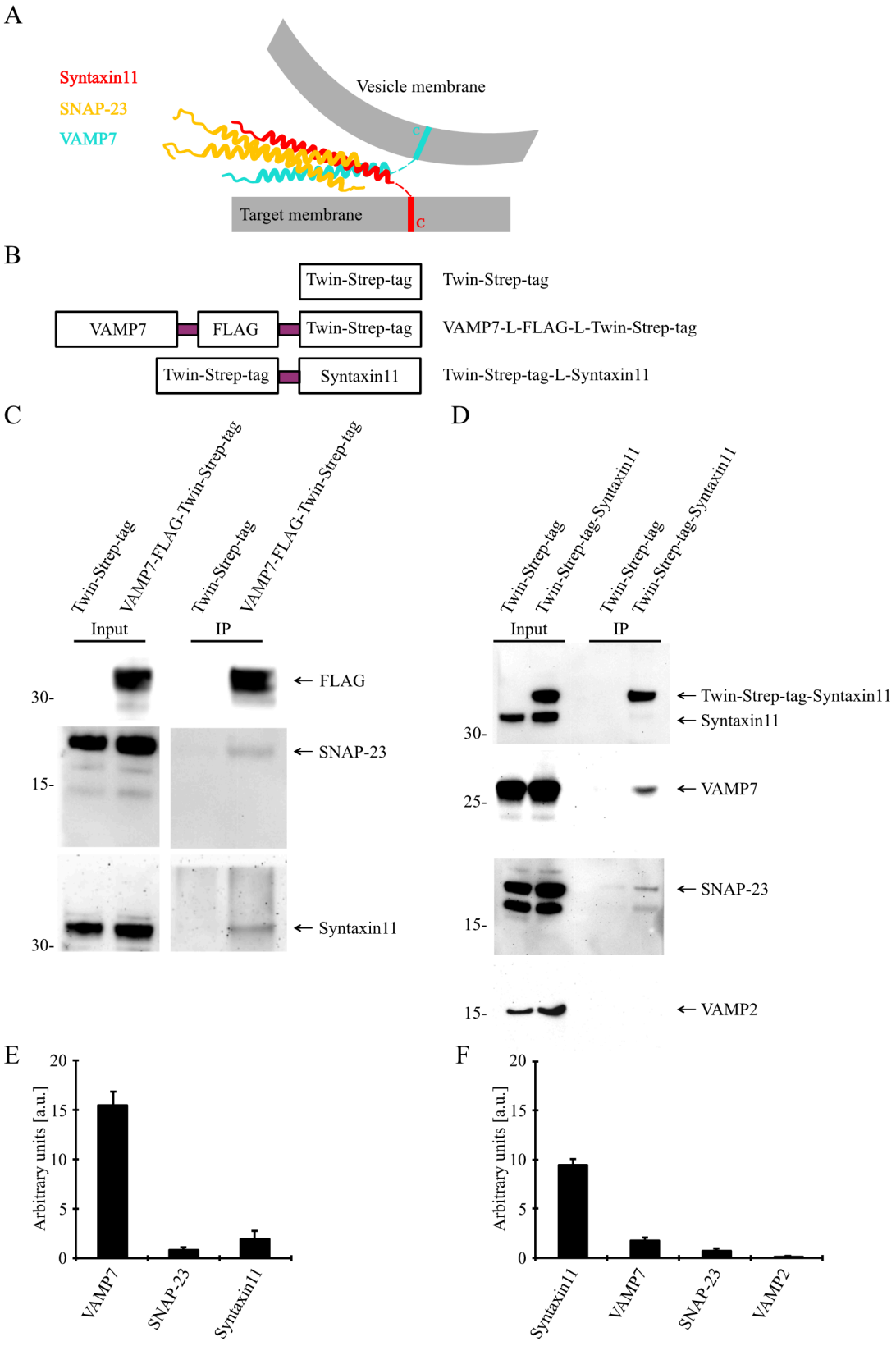

Figure 37: VAMP7 forms a SNARE complex with SNAP-23 and Syntaxin11.
(A) Model illustrates the SNARE complex formation between VAMP7 (v-SNARE), SNAP-23 and Syntaxin11 (t- SNARE) during CG fusion in primary human CD8$^+$ T cells. (B) Various Twin-Strep-tag fusion constructs were used for pulldown assay. For VAMP7, Twin-Strep-tag was

fused at the C terminus and for Syntaxin11; it was fused at the N terminus with (GGSGGSGGS) linker in between. (C) Bead stimulated primary human $CD8^+$ T cells were electroporated with VAMP7-Twin-Strep-tag construct. Cells were lysed after 12-16 h and lysates were incubated with Strep-Tactin sepharose beads. The precipitates were analysed with FLAG, SNAP-23, and Syntaxin11 antibodies respectively. (D) Bead stimulated primary human $CD8^+$ T cells electroporated with Twin-Strep-tag-tagged Syntaxin11. Cells were lysed, and the lysates were incubated with Strep-Tactin sepharose beads. The precipitates were analysed with antibodies against Strep-tag, SNAP-23, VAMP7, and VAMP2. Cells were electroporated with Twin-Strep-tag construct (as a control). 10% of the lysates were loaded as input. (Chitirala et al., 2019)(E) & (F) The relative amount of co-precipitated SNAREs quantified by densitometry. Bars indicated were means ± SEMs. Adapted from (Chitirala et al., 2019).

3.33 Overexpression of VAMP7 longin domain inhibits CG transport to IS

We have shown that VAMP7 silencing leads to a decrease in the percentage of CG fusion at the IS. VAMP7 consists of a long N-terminal domain in comparison to other VAMP isoforms (Figure 38A). Such longin domain overexpression inhibits neurite outgrowth, whereas longin domain deletion activates SNARE-complex assembly and stimulates the growth of neurites in staurosporine-differentiated PC12 cells (Martinez-Arca et al., 2000). We used TIRFM microscopy to investigate the proposed auto-inhibitory mechanism of the longin domain in primary human $CD8^+$ T cells. For that, we generated a VAMP7 longin domain (first 1-110 aa of VAMP7) fusion construct with mCherry and co-transfected with CG marker GzmB-mTFP to visualize the effect of the longin domain on granule polarization and fusion at the IS on CD3 coated coverslips. Interestingly, we observed significant differences both in the percentage of cells showed secretion in VAMP7 (longin domain) electroporated cells (14.07 ± 4.07 %) compared to the cells that are electroporated with GzmB-mTFP alone (45.37 ± 2.44 %) and in the average number of granules fused per cell in VAMP7 (longin domain) electroporated cells (0.44 ± 0.23) compared to the cells that are electroporated with GzmB-mTFP alone (1.69 ± 0.44) (Figure 38C & D). In addition, we also observed fewer CGs appearing in the TIRF field in the case of VAMP7 (longin domain) transfection (Figure 38B) and a three-fold higher frequency of fusion, (Figure 38E) indicating a role of the longin domain in the transport of CGs to the plasma membrane during IS formation.

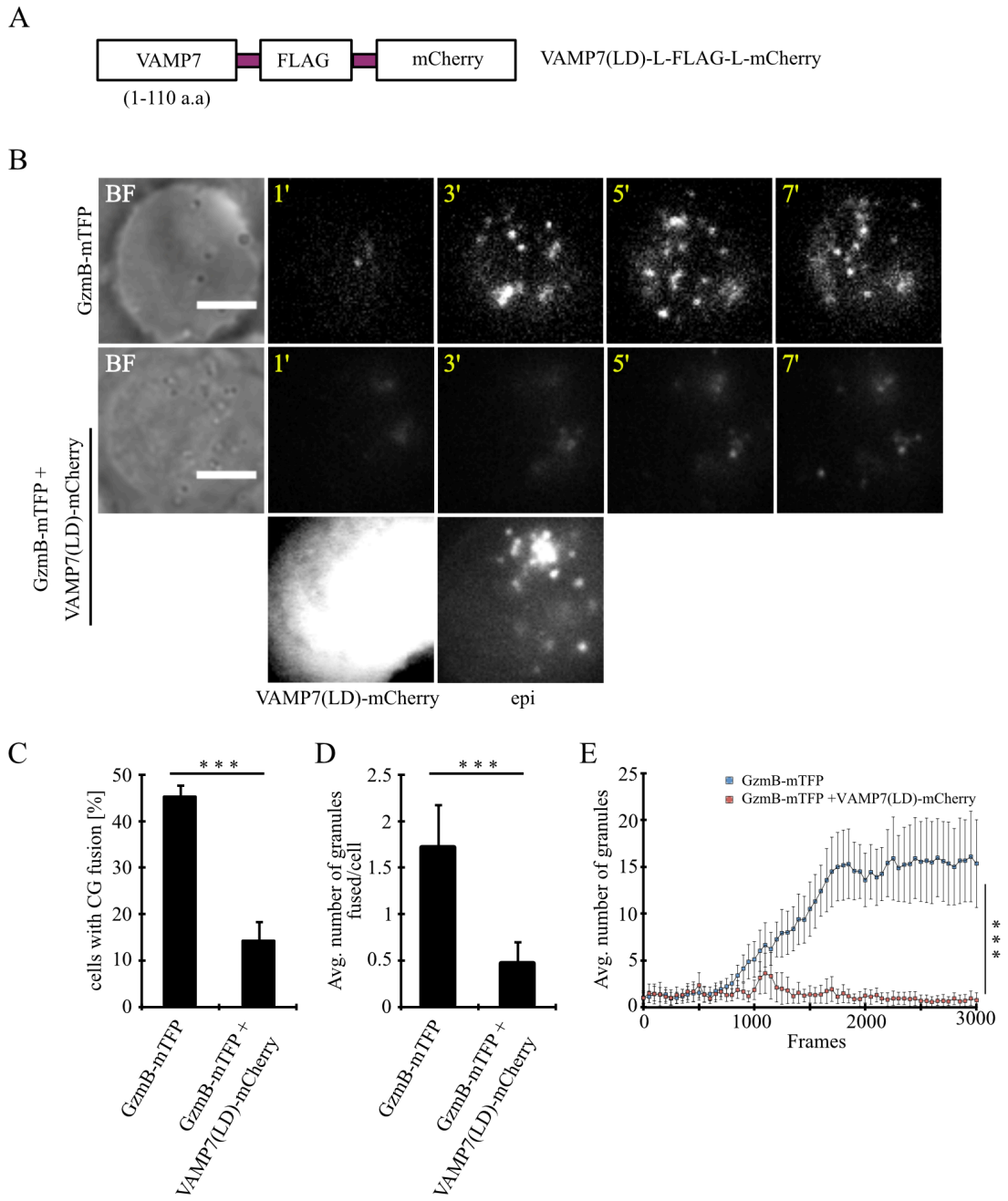

Figure 38: Longin domain affects CG trafficking to the plasma membrane.
(A) A schematic showing the VAMP7 longin domain (LD)-mCherry fusion construct design. (B) Bead stimulated primary human CD8$^+$ T cells electroporated with GzmB-mTFP alone or co-transfected with VAMP7 (LD)-mCherry and GzmB-mTFP constructs and imaged after 12 h of transfection. Selected live-cell TIRFM images of GzmB-mTFP in a electroporated CTL in contact with an anti-CD3 coated coverslip (GzmB, upper panel; GzmB (co-transfected with VAMP7 (LD)-mCherry), middle panel; VAMP7 (LD)-mCherry and epifluorescence image, lower panel). (C) Mean cumulative fusion events in the TIRF plane per cell (N = 3, n = 35 and 48, ***p < 0.001 (t-test)). (D) Mean average number of granules fused per cell (N = 3, n = 35 and 48, ***p < 0.001 (t-test)). (E) Mean average number of GzmB-containing vesicles in the TIRF plane per cell in the first 5 minutes of measurements (N = 3, n = 10 and 13, ***p < 0.001 (Mann-whitney Rank Sum Test)). Data indicated were means ± SEM. Scale bar, 5 µm.

3.34 VAMP7 longin domain does not alter recycling endosomal transport to the IS

We then examined the effect of VAMP7 longin domain overexpression on recycling endosomal transport to the IS. Since we showed (Figure 33) that the recycling endosomal fusion to the plasma membrane is mediated by VAMP8, we expected no difference in the transport of Rab11a containing vesicles to the plasma membrane upon VAMP7 longin domain overexpression. The VAMP7 longin domain fusion construct with mCherry was co-transfected with the recycling endosomal marker EGFP-Rab11a construct to visualize granule polarization and fusion at the IS on CD3 coated coverslips. As expected, we did not observe any significant difference in either the percentage of cells with secretion in VAMP7 (longin domain) electroporated cells (42.22 ± 2.22 %) compared to the cells that are electroporated with EGFP-Rab11a alone (44.85 ± 1.1 %) or in the average number of granules fused per cell in VAMP7 (longin domain) electroporated cells (27.55 ± 2.23) in comparison to EGFP-Rab11a alone (31.37 ± 0.77) (Figure 39B & C). We also observed no difference between the average numbers of granules approaching the TIRF plane in EGFP-Rab11a electroporated cells as compared to VAMP7 longin domain electroporated cells (Figure 39D).

This data confirms our previous and current findings, which strongly indicate that VAMP7 longin domain plays an important role in the function of primary human CD8+ T cells by regulating the transport of CGs and inhibits fusion at the plasma membrane during IS formation.

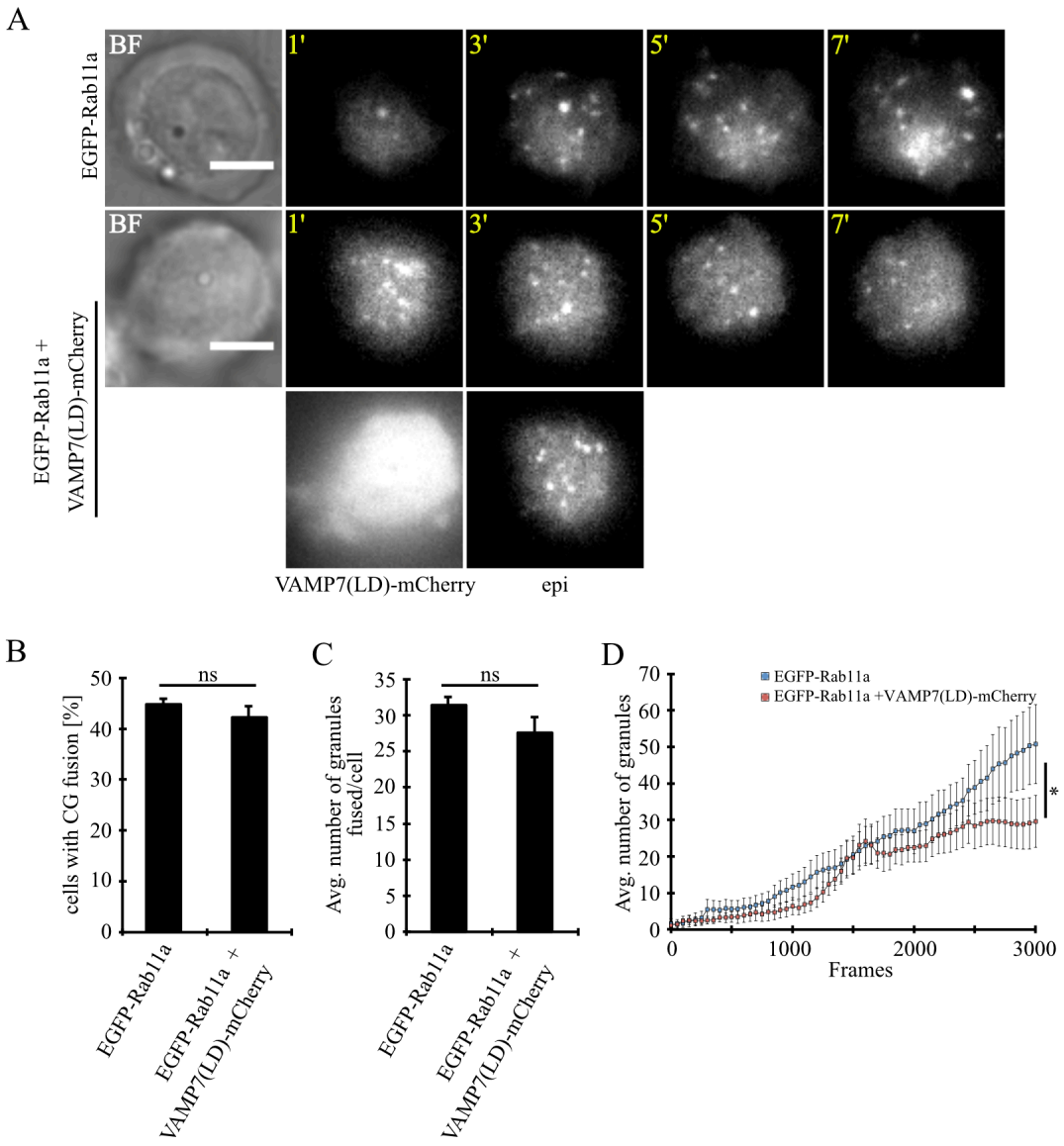

Figure 39: Longin domain has no effect on the recycling endosomal trafficking to the plasma membrane.
(A) Bead activated primary human CD8⁺ T cells electroporated with EGFP-Rab11a construct alone or co-transfected with VAMP7 (LD)-mCherry construct and imaged after 12 h of transfection. Selected live-cell TIRFM images of EGFP-Rab11a from an electroporated CTL which is in contact with an anti-CD3 coated coverslip (Rab11a, upper panel; Rab11a (co-transfected with VAMP7 (LD)-mCherry), middle panel; VAMP7 (LD)-mCherry and epi fluorescence image, lower panel). (C) Mean cumulative fusion events in the TIRF plane per cell (N = 3, n = 49 and 45, p = 0.349 (t-test)). (D) Mean average number of granules that were fused per cell (N = 3, n = 49 and 45, p = 0.182 (t-test)). (E) Mean average number of Rab11a-containing vesicles that appeared in the TIRF plane per cell in the first 5 minutes of measurements (N = 3, n = 10 and 11, *p < 0.035 (Mann-whitney Rank Sum Test)). Data indicated were means ± SEM. Scale bar, 5 µm.

Further, we aim to visualize the fusion of CGs in live mouse using two-photon microscopy. For that purpose, we designed a strategy to replace the monomeric red fluorescent protein mRFP from Syb2-mRFP mice with pH-sensitive, ratiometric fluorophore with high brightness.

Generation of Synaptobrevin2 knock-in mice

3.35 Amplification of mTFP, TagRFP-T and pHluorin2

In parallel to the before described functional projects on isolated CTLs from human and mouse, we also generated several Knock-in mouse lines where Synaptobrevin2 was fused to different fluorescent markers. For that, we selected mTFP (photostable fluorophore), TagRFP-T (10x more photostable than TagRFP) and pHluorin2 (ratiometric pH-sensitive fluorophore). NPY-mTFP plasmid was used as a template for amplifying mTFP. TagRFP-T was amplified from pCR259-TagRFP-T construct (gift from Dr. Peter Lipp, Uniklinik, Homburg). pHluorin2 was synthesized from IDT (IDT custom gene synthesis program). The amino acid sequence from pHluorin2 was codon optimised for Mus musculus.

pHluorin2 amino acid sequence after codon optimization:

MSKGEELFTGVVPILVELDGDVNGHKFSVSGEGEGDATYGKLTLKFICTTGKLPVPWPTLVT
TLSYGVQCFSRYPDHMKQHDFFKSAMPEGYVQERTIFFKDDGNYKTRAEVKFEGDTLVNRI
ELKGIDFKEDGNILGHKLEYNYNEHLVYIMADKQKNGTKAIFQVHHNIEDGSVQLADHYQQNT
PIGDGPVLLPDNHYLHTQSALSKDPNEKRDHMVLLEFVTAAGITHGMDELY-STOP-**Not1 restriction site**

pHluorin2 amino acid sequence after codon optimization:

ATGTCAAAGGGCGAGGAGCTTTTTACAGGTGTCGTTCCCATCCTGGTCGAACTGGACGG
TGACGTGAACGGTCACAAATTCAGCGTCTCCGGCGAGGGGGAAGGTGATGCCACCTAT
GGGAAACTGACACTTAAATTCATATGCACTACGGGAAAACTCCCCGTGCCCTGGCCCAC
CCTTGTGACCACCCTCTCTTATGGTGTGCAGTGCTTCTCCCGCTATCCGGATCATATGAA
ACAGCATGACTTTTTCAAGTCCGCAATGCCTGAGGGATACGTCCAGGAGAGGACCATCT
TCTTCAAAGATGACGGGAACTACAAGACAAGGGCAGAGGTGAAGTTCGAGGGAGATAC
CCTTGGTTAACAGAATTGAACTTAAAGGAATCGACTTCAAGGAAGATGGTAACATCCTGGG
TCACAAACTGGAGTACAACTATAATGAGCACCTCGTATACATTATGGCAGATAAGCAGAA
GAACGGCACAAAGGCTATATTCCAAGTCCACCATAATATCGAGGACGGCTCTGTGCAGC
TGGCTGACCACTATCAGCAGAACACCCCTATCGGCGATGGCCCGGTTCTTTTGCCCGAT
AACCATTACCTCCACACACAAAGCGCTCTTTCCAAGGATCCTAACGAGAAAAGAGACCA
CATGGTGCTCCTGGAGTTCGTCACGGCCGCAGGGATTACCCATGGGATGGACGAGTTG
TACTAA**GCGGCCGC**

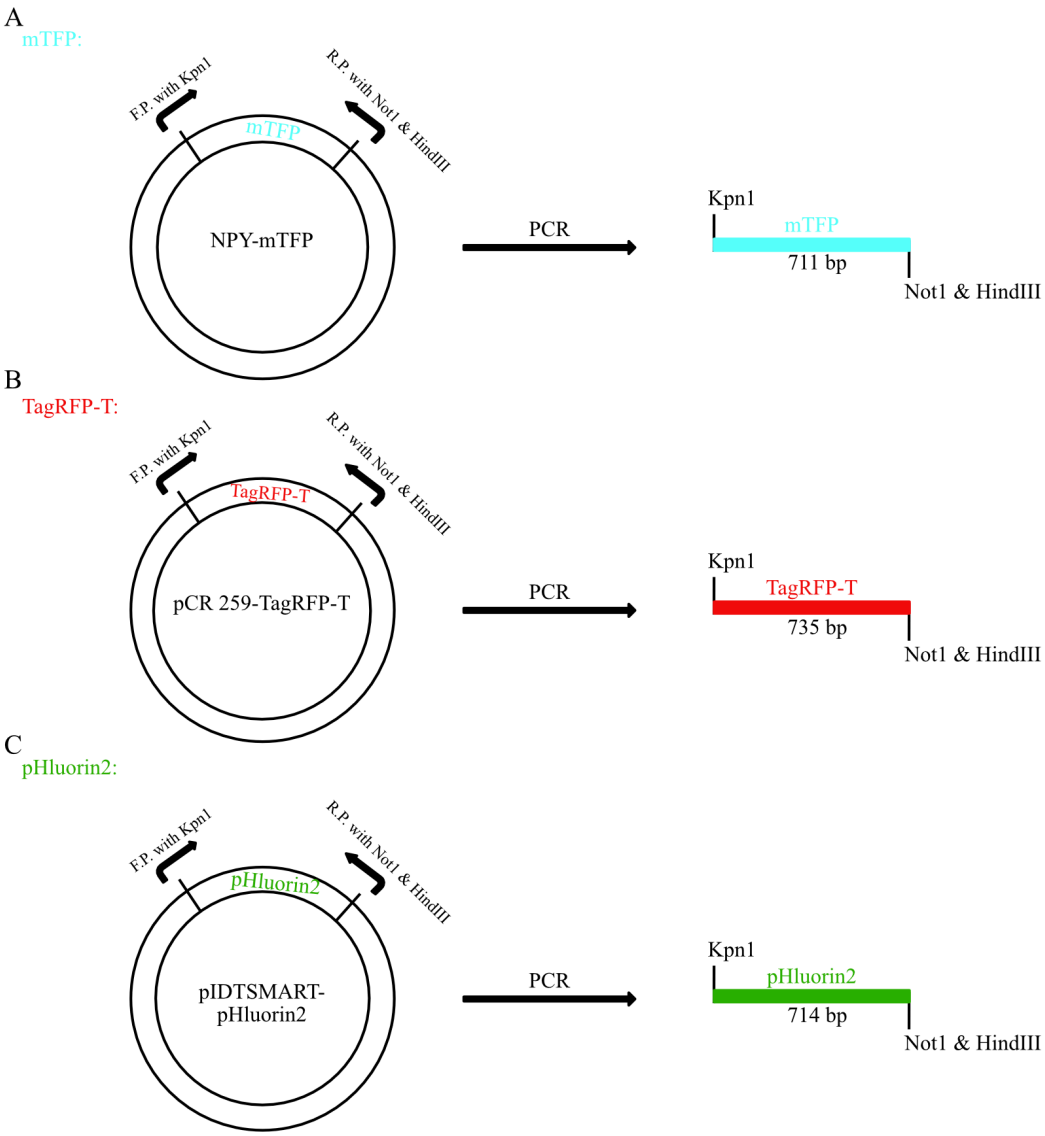

Figure 40: Amplification strategy for mTFP, TagRFP-T and pHluorin2.
(A) Schematic representation of the amplification strategy for mTFP, (B) TagRFP-T and (C) pHluorin2 with forward primer (with kpn1) and reverse primer (with Not1 and HindIII).

3.36 Cloning of targeting vectors

For the generation of Synaptobrevin2-Knock-in mouse, Synaptobrevin-2-mRFP targeting vector (Matti et al., 2013) was used. In the targeting vector, the stop codon in the last coding exon (Exon 5) of the Synaptobrevin2 gene was replaced in-frame by the coding region for mTFP or TagRFP-T or pHluorin2. Targeting vector has a cassette containing the neomycin resistance gene under the control of the CMV promoter and the Cre-recombinase gene under the control of a testis-specific promoter flanked by two loxP sites from plasmid pACN (kindly provided by M. Capecchi) downstream of the mTFP or TagRFP-T or pHluorin2 STOP codon. One copy of the HSV (herpes simplex virus) thymidine kinase gene was present at the 3' end of the targeting vector. Targeting vector was digested with Not1 restriction site to remove the Synaptobrevin2-mRFP and replace with

Synaptobrevin2-mTFP from pCDNA3.1(-) (used as a shuttle vector to clone Synaptobrevin2-mTFP, Synaptobrevin2-TagRFP-T and Synaptobrevin2-pHluorin2 with 5'-Not1 and 3'-Not1 & HindIII restriction sites). Both targeting vector and inserts were ligated and screened for clones with inserts in correct orientation (5' to 3').

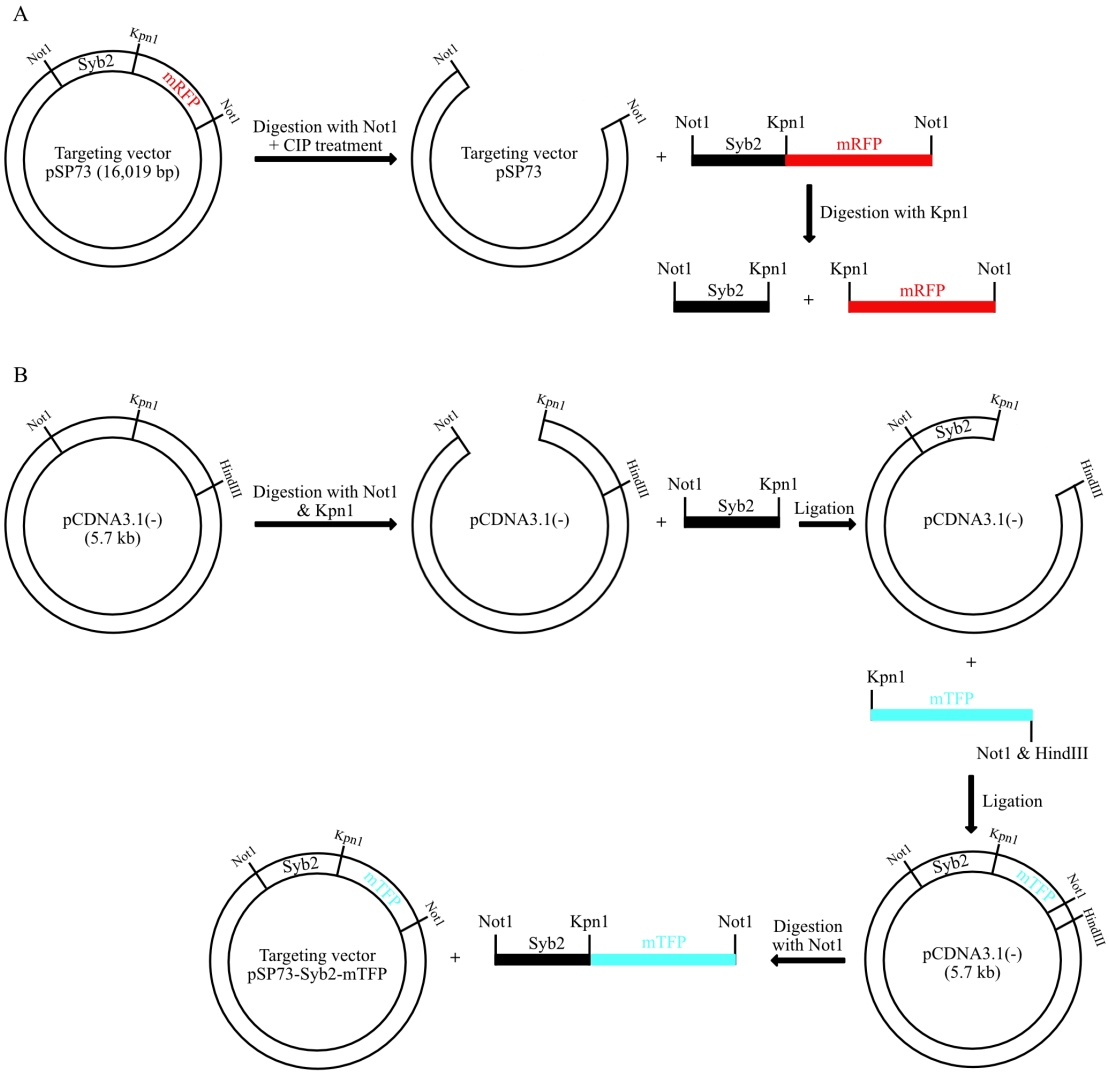

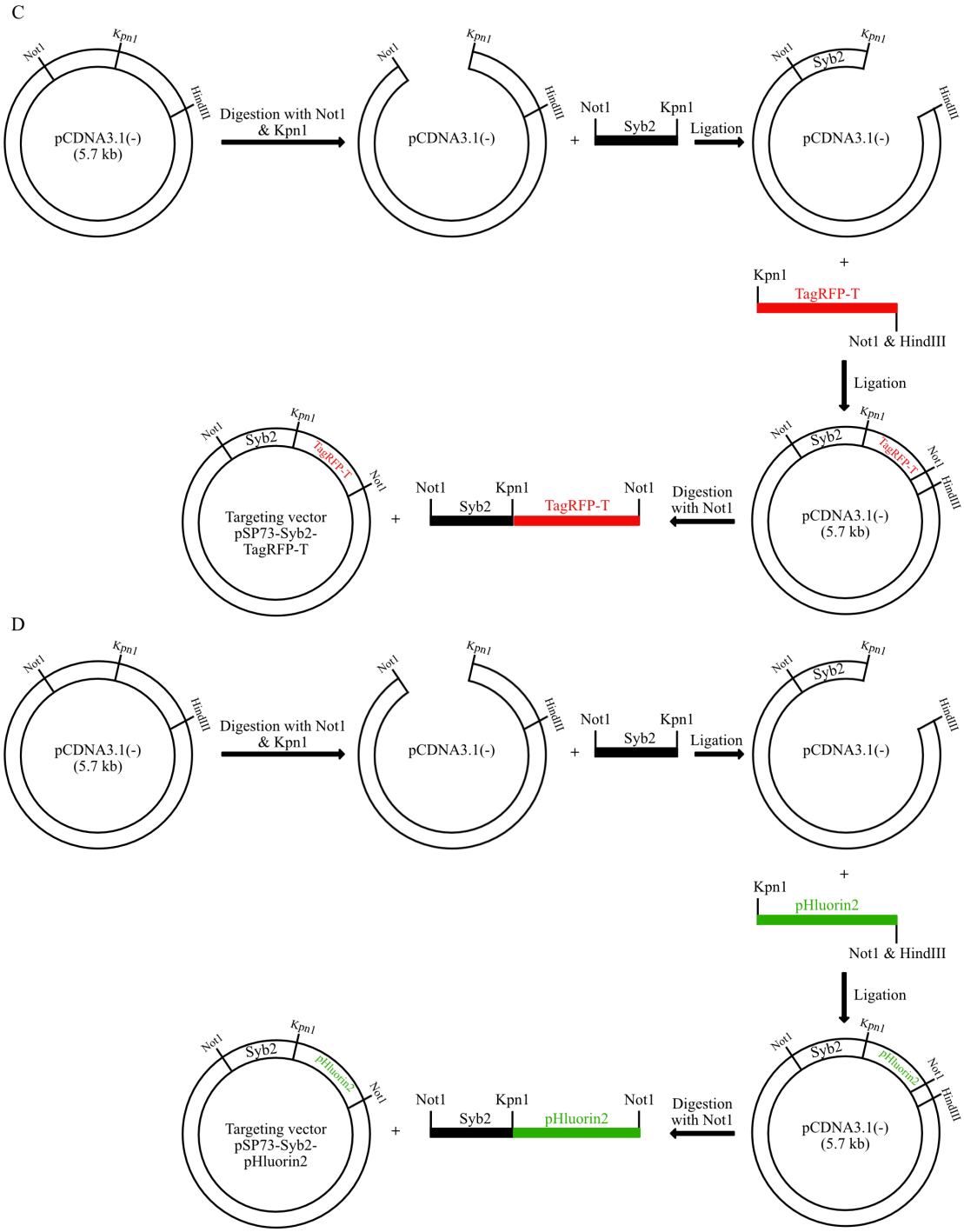

Figure 41: Cloning strategy of Synaptobrevin2 targeting vectors.
(A) Schematic representation of the targeting vector digestion (B) Cloning of Synaptobrevin2-mTFP (C) Synaptobrevin2-TagRFP-T and (D) Synaptobrevin2-pHluorin2 targeting vectors from pCDNA3.1 (-) shuttle vector.

3.37 Electroporation of Embryonic Stem (ES) cells and generation of Synaptobrevin2 knock-in offspring

Successful homologous recombination results in the insertion of this construct into the endogenous Synaptobrevin2 locus on chromosome 11. The construct was

linearized using the Swa1 restriction enzyme and then the purified linearized construct was sent to Dr. Ectors at the GIGA institute at the University of Liège, for electroporation into R1 embryonic stem (ES) cells. Following targeting, one 96 well plate containing individual ES cell clones were sent to us for analysis. We performed Southern blot analysis using the enzyme Kpn1 and a ^{32}P-labelled 900 bp probe, which anneals 5' to the 5'-most extreme of the targeting construct. This allows us to distinguish between the wild type allele, producing a 17.4 Kb band and the correctly targeted Synaptobrevin2-mTFP or TagRFP-T or pHluorin2-Cre-containing knock-in allele which gives an 11.3 Kb band (Figure 42D).

Following Southern analysis, DNA from 96 clones (from Synaptobrevin2-TFP) could be visualized upon the membrane of which 55 were positive, giving a targeting frequency of 57.29 %. Clone B06 was injected and chimeras were obtained. After reaching adulthood, 3 males with 100 % chimerism were crossed with C57BL/6 females and the resulting offspring were genotyped by PCR for the presence of the Synaptobrevin2-TFP allele. These heterozygous mice were then imported into the animal facility in Homburg where they are now maintained as a heterozygous line and being backcrossed to with C57BL/6N mouse strain.

DNA from 96 clones (from Synaptobrevin2-TagRFP-T) could be visualized upon the membrane of which 36 were positive, giving a targeting frequency of 37.5 %. Clone D01 was injected and chimeras were obtained. After reaching adulthood, 3 males with 100 % chimerism were crossed with C57BL/6 females and the resulting offspring were genotyped by PCR for the presence of the Synaptobrevin2-TagRFP-T allele. These heterozygous mice were then imported into the animal facility in Homburg where they are now maintained as a heterozygous line and being backcrossed to with C57BL/6N mouse strain.

DNA from 86 clones (from Synaptobrevin2-pHluorin2) could be visualized upon the membrane of which 13 were positive, giving a targeting frequency of 13.54 %. Clone C06 was injected and chimeras were obtained. After reaching adulthood, 3 males with 100 % chimerism were crossed with C57BL/6 females and the resulting offspring were genotyped by PCR for the presence of the Synaptobrevin2-pHluorin2 allele. These heterozygous mice were then imported into the animal facility in Homburg where they are now maintained as a heterozygous line and being backcrossed to with C57BL/6N mouse strain.

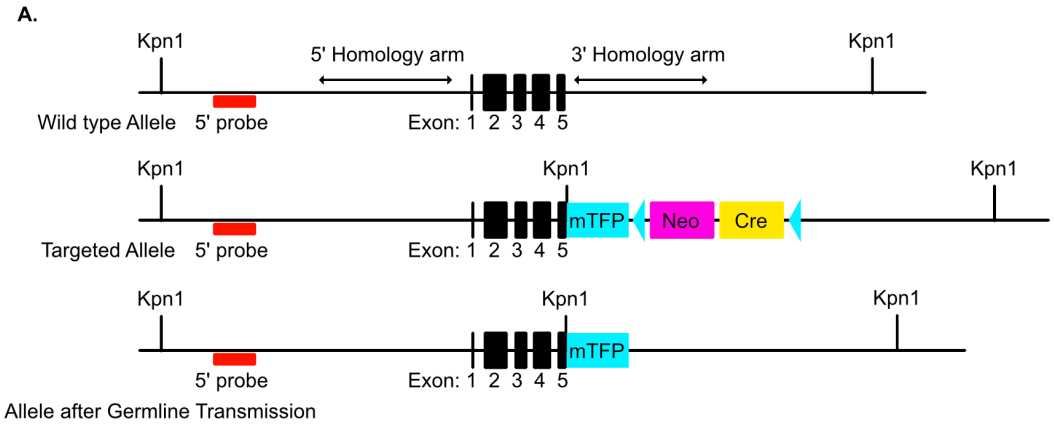
A.
Kpn1
5' Homology arm
3' Homology arm
Kpn1
Wild type Allele
5' probe
Exon: 1 2 3 4 5
Kpn1
Kpn1
Kpn1
mTFP
Neo
Cre
Targeted Allele
5' probe
Exon: 1 2 3 4 5
Kpn1
Kpn1
Kpn1
mTFP
5' probe
Exon: 1 2 3 4 5
Allele after Germline Transmission

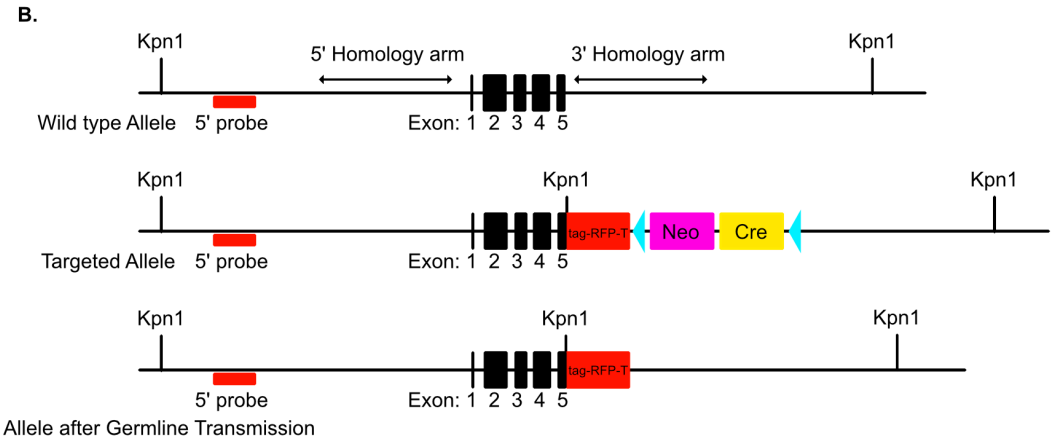
B.
Kpn1
5' Homology arm
3' Homology arm
Kpn1
Wild type Allele
5' probe
Exon: 1 2 3 4 5
Kpn1
Kpn1
Kpn1
tag-RFP-T
Neo
Cre
Targeted Allele
5' probe
Exon: 1 2 3 4 5
Kpn1
Kpn1
Kpn1
tag-RFP-T
5' probe
Exon: 1 2 3 4 5
Allele after Germline Transmission

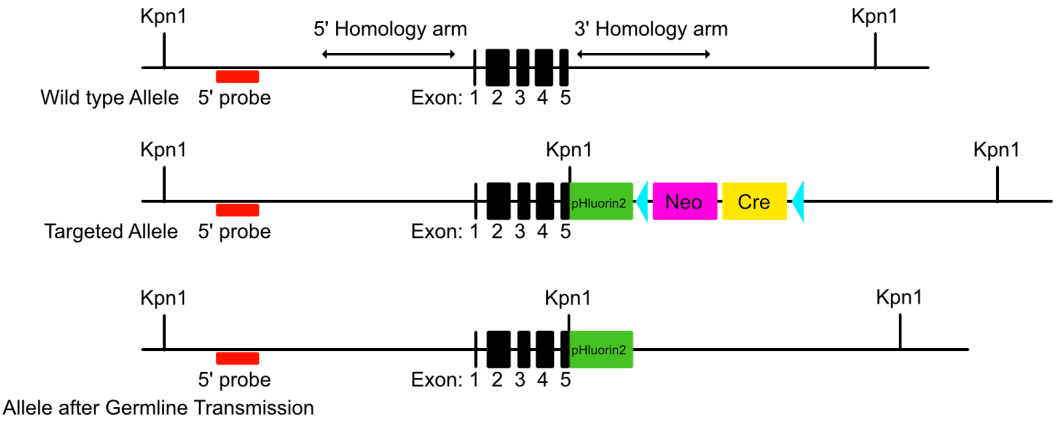
C.
Kpn1
5' Homology arm
3' Homology arm
Kpn1
Wild type Allele
5' probe
Exon: 1 2 3 4 5
Kpn1
Kpn1
Kpn1
pHluorin2
Neo
Cre
Targeted Allele
5' probe
Exon: 1 2 3 4 5
Kpn1
Kpn1
Kpn1
pHluorin2
5' probe
Exon: 1 2 3 4 5
Allele after Germline Transmission


D.
pSP73-Syb2-TFP
pSP73-Syb2-TagRFP-T
pSP73-Syb2-pHluorin2
λ 1Kb
21 Kb
10 Kb
-17.4 Kb
-11.3 Kb

Figure 42: Generation of Syb2 knock-in mouse.
(A) Targeting strategy of Synaptobrevin2-mTFP (B) Synaptobrevin2-TagRFP-T & (C) Synaptobrevin2-pHluorin2 knock-in mouse leaving the synaptobrevin2 gene locus intact except for the addition of the coding sequence for GGSGGSGGT linker and TFP. (D) Southern blot analysis for ES cell targeting. Both 17.4kb and 11.3kb bands confirm Knock-in.

3.37 Expression and Fusion of CGs from Synaptobrevin2-mTFP (+/-) knock-in

Unfortunately, we could not get any homozygous animals from all three knock-in mice even after backcrossing the mice with C57BL/6N mice strain for 10 generations. Among all the three mouse lines, only Syb2-mTFP (+/-) knock-in mouse showed expression in primary $CD8^+$ T cells. SIM images showed relatively bright puncta (Figure 43A) and we were able to visualize the fusion of CGs in the TIRF plane on an anti-CD3 coated coverslip with the addition of 10 mM calcium-containing extracellular solution (Figure 43B).

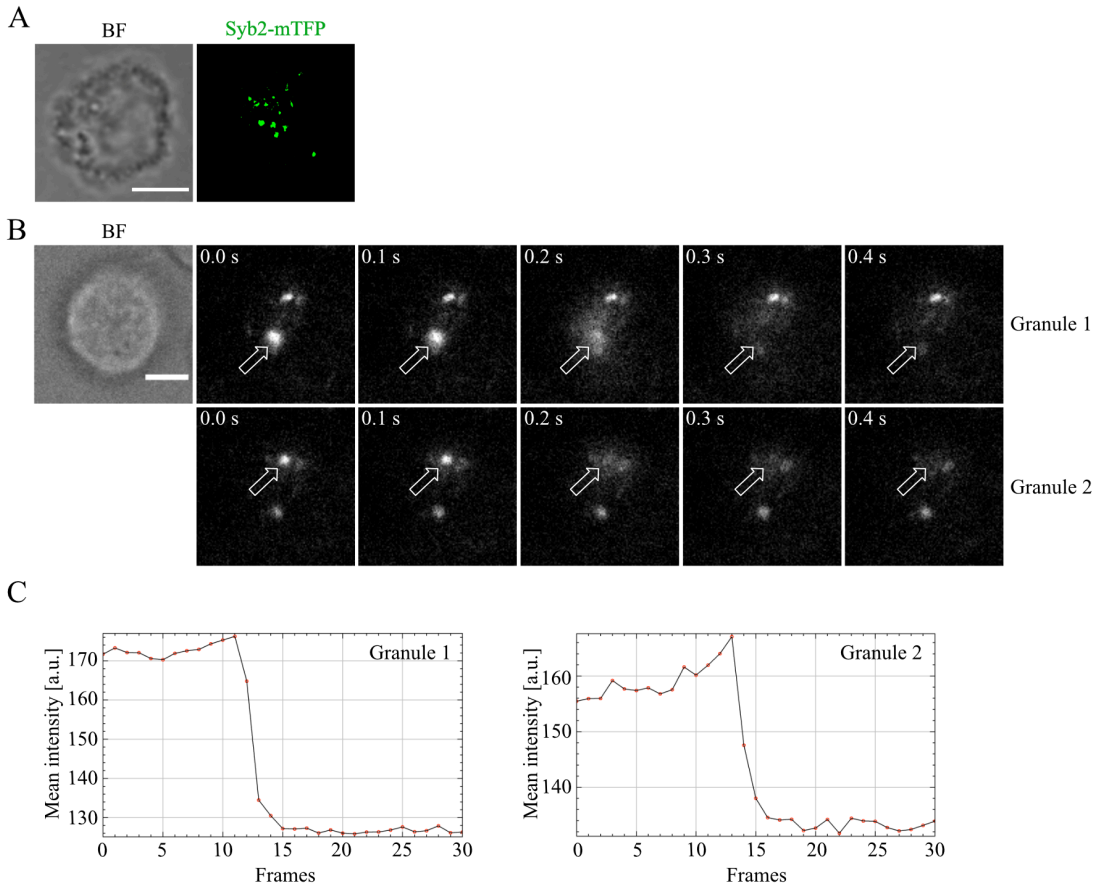

Figure 43: Visualization of CG fusion from Syb2-mTFP (+/-) CTLs.
(A) Representative SIM images from day 5 Syb2-mTFP heterozygous mouse $CD8^+$ T cell. (B) TIRF images shows the individual fusion events (granule 1; upper panel and granule 2; lower panel). Individual fusion events were depicted with open arrows. (C) Graphs depicted were the mean fluorescence intensity of individual mTFP vesicles over time, respectively. Experiments were performed with three individual donors (n = 7 cells). Scale bar, 5 µm.

4. Discussion

Our findings define a major role of the a3-subunit in mouse primary $CD8^+$ T cells. a3-subunit downregulation inhibits the acidification of CGs thus, affecting the morphology of CGs. This leads to a defect in trafficking of cytotoxic granules toward the IS affecting the main function of CTLs. We showed that among four 'a' subunit isoforms, three were expressed in CTLs. We demonstrated that downregulation of the a3 isoform resulted in a reduced number of CGs approaching the TIRF plane followed by a strong reduction in CG secretion compared to control cells. The knockdown of a1 and a2 subunits did not alter the pH of CGs.

We also showed that the a3 subunit is co-localized with the CG marker GzmB using a polyclonal antibody against a3. We could not detect any interaction of 'c' or 'a' subunits with synaptobrevin2 indicating that in mouse primary CTLs a3 is not involved in the fusion mechanism of CGs.

Finally, by using electron microscopy we demonstrated that a3 knockdown changes the morphology of CGs thus affecting the transport and fusion of CGs at the IS. We also observed that upon a3 down-regulation the dense core of the CGs less matrix than those of control cells. This presumably resulted in the inactivation of GzmB inside CGs and degradation of Perforin which are crucial for CTL function.

4.1 Expression of the a3 isoform

In mice, Northern blot analysis of the a3-subunit isoform shows its ubiquitous expression in all tissues such as heart, brain, spleen, lung and kidney but majorly in the liver (Toyomura et al., 2000). TCIRC7, an alternative splice variant lacking first 217 aa in the hydrophobic region of a3 was shown to have a major role in T cell activation *in vitro* and *in vivo* (Susani et al., 2004) (Heinemann et al., 1999). In mouse endocrine cells (pancreatic β-cells), the a3 subunit localizes on insulin-containing secretory granules and regulates insulin secretion. Though mutant mice with defective V-ATPase subunits produced insulin in mature form, they were less competent for hormone secretion. Thus, indicating a specific role of a3 in membrane fusion (Sun-Wada et al., 2006).

The a3-isoform is also highly expressed in adrenal, parathyroid, pituitary and thyroid glands indicating its functional relevance in various exo- and endocytic pathways and mammalian hormone secretion (Sun-Wada et al., 2007).

We could demonstrate that immunostaining of a3 subunit with a polyclonal antibody showed punctate staining in mouse CTLs that co-localized significantly with CGs with Pearson's colocalization coefficients above 0.5 with endogenous synaptobrevin2 (Figure 14). Many puncta did not colocalize with CGs that might be due to a3 localized on lysosomes (Toyomura et al., 2003). We also checked the expression of 'a' subunit isoforms in CD3/CD28 bead stimulated CTLs that showed

expression of a1, a2 and a3 (highly expressed compared to other isoforms) but not a4 (Figure 13A).

4.2 Functional diversity of a3-subunit

The V-ATPase is essential for vesicular trafficking during the early stages of development. From yeast to mammals lack of V-ATPase subunits lead to lethal developmental abnormalities. In *Caenorhabditis elegans* silencing three of four a-subunit isoforms leads to death during early developmental stages (Oka et al., 2001). The a3 isoform is also involved in bone homeostasis by providing an acidic environment in lacuna (compartment formed between the plasma membrane and bone surface) for bone matrix degradation. Similarly, in humans, mutations in a3 isoform (Tcirg1) results in lethal autosomal recessive osteopetrosis (Frattini et al., 2000) (Kornak et al., 2000) and is also co-localized with d2 subunit in human osteoclasts. Whereas, knockout of d2-subunit in mice leads to defective osteoclast function resulting in increased bone mass (Lee et al., 2006).

In a macrophage cell line (RAW264.7), a3 is localized on lysosomes and found along with other lysosomal enzymes on the plasma membrane upon stimulation. This confirms its targeting from lysosomes to the plasma membrane suggesting its role in lysosomal exocytosis. Similarly, lysosomal exocytosis from phagocytes, neutrophils and monocyte-derived cells including osteoclasts and macrophages requires the V-ATPase subunit indicating its important role in fusogenic activity in general. However, the role of other V-ATPase subunits in vesicular trafficking cannot be ignored.

Since the a3 knockout mice die within four weeks due to severe osteopetrosis, we used specific siRNAs against the a3 protein in our studies. After 12 h of transfection, we observed an efficient decrease in a3 protein levels verified by western blot analysis (Figure 14D). The pH measurements conducted with a pH-sensor inside the CGs revealed that upon a3 knockdown alone the pH inside CGs was altered (raised from pH 6.1 to pH 7) (Figure 14E). We also showed by electron microscopy that a3 knockdown CTLs displayed changes in the morphology of CGs compared to control cells (Figure 22). This is on par with observations from (Kataoka et al., 1994) demonstrating the effect of concanamycin-A (CMA: V-ATPase inhibitor) on OE4 cells (special $CD8^+$ clone). CMA treated OE4 cells showed CGs with irregular shapes, empty, swollen, fused and divided granules devoid of small vesicles with impaired killing efficiency when conjugated with (p815) target cells. However, CMA treatment did not alter the surface expression of TCR, CD3, CD8 and CD11a.

We took the advantage of GzmB-mTFP knockin mice, which express a GzmB-mTFP fusion protein endogenously (see Figure 16A-D). Even though mTFP is cleaved off inside the CGs with an unknown mechanism (verified by western blot),

we checked the activity of the remaining GzmB. By using Casper3-GR reverse fret construct with DEVD (target cleavage site for active GzmB), we proved that the GzmB inside CGs was active (Figure 16F) and also showed that it is released upon stimulus on anti-CD3 coated coverslips performed with TIRFM (Figure 16E). siRNA mediated downregulation of a3 combined with TIRFM studies in primary CTLs revealed that cells devoid of a3 show reduction in the average percentage of CTLs with secretion (Figure 17A-C) and importantly, the average number of CGs appearing in the TIRF plane were drastically reduced (Figure 17D). These results led us to investigate the role of a3 in the transport of CGs along the microtubules (a prerequisite for granule polarization).

4.3 V-ATPase interaction with small GTPases: Functional significance

Acidic pH is crucial for vesicular trafficking in all cell types. The tightly regulated processes such as multi-vesicular body (MVBs) or endosomal carrier vesicles (ECVs) and exosome formation and secretion is dependent upon acidification in early endosomes in BHK cells (Clague et al., 1994). It has been shown in the recruitment of coatomer proteins and Arf1 (small GTPase) onto early endosomes in an acidification-dependent manner (Aniento et al., 1996). In kidney epithelial cells, intra endosomal acidic pH drives the recruitment of ARNO (ADP-ribosylation factor nucleotide site opener)/Arf6 and their interaction with V-ATPase c-subunit is important for protein trafficking between early and late endosomes during protein degradation pathway (Hurtado-Lorenzo et al., 2006). Recently, using a3-KO mice, it was shown that V-ATPase a3-subunit has a dual function in acidifying lacunae and secretory lysosome trafficking via Rab7 recruitment (Matsumoto et al., 2018). These biochemical interaction assays were performed in HEK293T cells and we have carried out similar experiments in primary activated CTLs. Other reports showed that V-ATPase can directly interact with the actin-microfilament cytoskeleton and that it requires an intact microtubular network to detach between V_0V_1 domains (Forgac, 2007a). These molecular interactions between V-ATPase and small GTPases indicate that GTPases might function as on/off switches for the V-ATPase function.

These studies encouraged us to examine the role of the a3-subunit in mouse $CD8^+$ T cells. We show that a3 knockdown by gene silencing using siRNAs leads to a strong reduction in the average number of CGs appearing in the TIRF plane (see Figure 17D) a similar phenotype to the reported defective secretory lysosomal trafficking in osteoclasts. We also performed Twin-Strep-tag pulldown assays with Rab7a and Rab27a (both dominant negative and dominant active forms) fusion constructs expressed in primary mouse CTLs. We did not detect any interaction of GTPase with a3-subunit (Figure 19& Figure 20). This indicates that there might be

other Rabs interacting with a3 in mouse CTLs or that the interaction might be transient and not detected with our pulldown assay.

Taken together, in agreement with the above-described findings and based on our results, it is evident that a3 plays a major role in mediating CG fusion in primary, mouse CTLs. siRNA mediated knockdown in CTLs isolated from GzmB-mTFP knockin mice endogenously expressing fluorescent CG marker GzmB, allowed us to detect defective CG transport and fusion. With the help of electron microscopic observation on CTLs in which a3 was knocked down, we could study the morphology of CGs. We were unable to discover the molecular mechanism behind the reduced granule polarization towards the IS. Interestingly, using super-resolution STED microscopy we could demonstrate that defective polarization of CGs might be due to lack of interaction between a3 on the CGs with other Rab proteins, which in turn interacts with kinesins for the transport of vesicles along with the microtubule network (Figure 21). Since the human isoform of the a3-subunit leads to 50% of osteopetrosis cases, a3 might serve as a major target for the development of innovative drugs for improving the life span in the affected population.

vSNARE of human CTLs

In this study, we also have examined the role of VAMP7 in CTL function. In primary $CD8^+$ T lymphocytes, our findings identified VAMP7 as the vSNARE required for fusion of CGs with the plasma membrane at the IS. We showed that the downregulation of VAMP7 expression by siRNA led to a significant reduction in CG fusion at the IS followed by a reduction in target cell killing *in vivo*. We also showed that VAMP7 interacts with the SNARE proteins Syntaxin11 and SNAP-23 in an in vitro binding assay showing its possible involvement in the human disease Familial Haemophagocytic Lymphohistiocytosis (FHL).

We finally showed that VAMP7 longin domain plays an important role in the trafficking and fusion of CGs at the IS. Whereas, recycling endosomal transport or fusion at the IS prior to CG fusion was unaltered.

4.4 Differences in the vSNAREs mediating CG fusion in human and mouse cells

SNAREs are the central components of membrane fusion. With the help of synaptobrevin2 knock-in mice and by using correlative light-electron microscopy (CLEM) it was previously reported that in primary mouse $CD8^+$ T cells cytotoxic granule fusion is mediated by VAMP2 in mice (Matti et al., 2013b). In that report, it was also shown that syb2 co-localized with the CG marker GzmB. By using immunoelectron microscopy and coimmunoprecipitation studies (Mollinedo et al., 2003) showed that VAMP2 also plays a role in the exocytosis of specific and

tertiary granules in human neutrophils. The Q-SNARE/R-SNARE complexes containing VAMP2 and syntaxin-4 were involved in the exocytosis of neutrophil granules. Our findings uncover an important difference in the mechanism of cytotoxic substances released between humans and mice. Even after tetanus toxin treatment, CG fusion was normal in human CTLs (Figure 23D). From this data, we could rule out an involvement of VAMP2 in CG fusion from human $CD8^+$ T cells. This conclusion is further supported by our data that showed a lack of co-localization of the CG marker GzmB or Perforin with VAMP2 in activated CTLs conjugated with target cells (Figure 25). We also found a decrease in VAMP2 protein levels upon T cell activation in contrast to VAMP7 levels, which were upregulated (Figure 24).

4.5 Expression of VAMP7

Previous results indicate that in mice, the VAMP7 shows a ubiquitous expression and localizes to various intracellular organelles, most predominantly to late endosomes and lysosomes. VAMP7 localization on late endosomes is mediated by its longin domain interaction with the delta subunit of the adaptor protein AP-3 (Kent et al., 2012). VAMP7 also forms a SNARE complex with SNAP-23 and Syntaxin4 as shown with an in vitro interaction assays in HeLa cells (Martinez-Arca et al., 2003). Similarly, it was demonstrated that VAMP7 is localized on late endosomal compartments and that it is required for heterotypic fusion of late endosomes with lysosomes in rat liver cell-free systems (Pryor et al., 2004b). In macrophages, VAMP7 mediates the fusion of late endocytic vesicles that results in early blockade of pseudopod extension (Braun et al., 2004a). These reports showed diverse roles of VAMP7 in various fusion processes and its ability to interact with various SNARE partners including Syntaxin1, Syntaxin3, Syntaxin4, Syntaxin7, Syntaxin8, SNAP-23 and SNAP-25.

Our findings with the help of super-resolution microscopy and overexpression of VAMP7 fusion constructs (either N or C terminus) demonstrate that VAMP7 is co-localized to a higher degree with GzmB and Perforin proteins on CGs from human CTLs as compared to other VAMPs (VAMP2, VAMP3, VAMP4 and VAMP8) (Figure 25A). This might be because CGs are lysosome-related organelles and VAMP7 also in other systems shows affinity to lysosomes. Similarly, in cultured primary astrocytes, VAMP7 is localized to lysosomes and acts as a vSNARE mediating secretory lysosome exocytosis, leading to release of ATP and cathepsin B from glial cells (Verderio et al., 2012). This suggests a potential role of VAMP7 in exocytosis of CGs in CTLs too.

In contrast to the “brevin” family of VAMPs like synaptobrevin 1 or 2, VAMP7 has an additional N-terminal domain called longin domain (first 6-110 aa of VAMP7), which is involved in controlling the SNARE complex assembly through interaction

with coiled-coil domains of several proteins (Martinez-Arca et al., 2003; Vivona et al., 2010). For example VAMP7, through its longin domain interaction with AP-3 (clathrin adaptor), Varp (guanine exchange factor) and Hrb (endocytic protein) determines its subcellular localization in various cell types (Burgo et al., 2009; Chaineau et al., 2008; Martinez-Arca et al., 2003; Pryor et al., 2008). Because of its diverse subcellular localization, VAMP7 has been associated with several membrane trafficking steps that include fusion of late endosomes to lysosomes, Golgi apparatus to plasma membrane exocytosis, and autophagosomal and lysosomal exocytosis (Advani et al., 1999; Braun et al., 2004b; Fader et al., 2012; Oishi et al., 2006; Pocard et al., 2007; Pryor et al., 2004a).

By using siRNA mediated knockdown of VAMP7 or VAMP7 KO mice it was shown (Larghi et al., 2013b) that VAMP7 is involved in the recruitment of vesicular Lat to the TCR-activation sites that is required for the Lat phosphorylation and T cell activation in primary CD4+ T cells. They also showed that VAMP7 knockdown resulted in a decrease in phosphorylation signaling molecules (PLC-γ1, SLP-76 and MAP kinases Erk1 and Erk2 along) indicating a defective signalosome formation during T cell activation if VAMP7 is missed. In contrast, using SIM we found no co-localization with Lat containing vesicles either in resting or activated human CD8 and mouse CD4 positive CTLs (Figure 26 & Figure 27) excluding its role in T cell signaling pathway in primary human CD8+ T cells.

4.6 Functional diversity of VAMP7

VAMP7 is involved in various cellular processes including cell polarization through apical transport (in epithelial cells), neuronal outgrowth (in PC12 cells and cultured neurons), synaptic transmission, lysosomal secretion (fibroblasts), membrane repair, cell migration, mitosis, and phagocytosis (formation of plasma membrane extensions at the sites of phagocytosis) (Chaineau et al., 2009; Daste et al., 2015a). In dendritic cells, VAMP7 regulates the secretion of IL-12, induced by contact with a cognate antigen-specific CTL (Chiaruttini et al., 2016). In rat enterocytes, VAMP7 is expressed in the endoplasmic reticulum (ER) but it is not present in the ER of kidney or liver. It plays an important role in the transport of triacylglycerol from ER to cis Golgi in the form of pre-chylomicron transport vesicles (PCTVs) (Siddiqi et al., 2006).

From all reported studies, it appears that VAMP7 localizes mainly in Golgi and late endosomes/lysosomes in most cell types. VAMP7 may have a role in anterograde and retrograde trafficking from Golgi and endocytosis as well. The mammalian post-Golgi network involves the v-SNAREs VAMP2 and VAMP3 (localize to early and recycling endosomes, respectively) (Das et al., 2004), VAMP4 (localizes to TGN) (Mallard et al., 2002), and VAMP7 and VAMP8 (involved in trafficking of recycling endosomes) that play a role in many intracellular trafficking steps from

various specialized cells (Lippert et al., 2007). Moreover, VAMP7 regulates the fusion of lysosome-associated membrane protein carriers that are derived from the trans-Golgi network with late endosomes (Pols et al., 2013). In addition it was suggested from in vitro studies that VAMP7 mediates heterotypic fusion between endosomes and lysosomes, whereas VAMP8 mediates homotypic fusion (Pryor et al., 2004a).

In polarized Caco-2 (heterogeneous human epithelial colorectal adenocarcinoma) and MDCK (Madin-Darby Canine Kidney) epithelial cells VAMP7 forms a SNARE complex with Syntaxin3 and SNAP-23 (tSNARE partners) that helps in TeNT resistant apical exocytosis (Galli et al., 1998).

4.7 Role of VAMP7 in immune cells

Multiple roles of VAMP7 in different cell types have been demonstrated by using siRNA mediated gene silencing or by overexpressing its longin domain to induce a dominant negative effect.

In human immune cells, both VAMP isoforms (VAMP7 and VAMP8) have been shown to translocate to the plasma membrane, forming a SNARE complex with Syntaxin4 and SNAP-23 which mediates activation-induced mast cell degranulation (Liu et al., 2018; Sander et al., 2008). From subcellular fractionation, flow cytometry and antibody inhibition studies in human eosinophils and neutrophils, VAMP7 also interacts with the tSNAREs Syntaxin4 and SNAP-23, enabling the release of eosinophil peroxidase and eosinophil-derived neurotoxin, myeloperoxidase, lactoferrin and matrix metalloprotease-9 (mediators) in a dose-dependent manner (Logan et al., 2006; Mollinedo et al., 2006). In B-cells, VAMP7 mediates the fusion of lysosomes at the IS. Thus, VAMP7 plays a critical role in antigen extraction and presentation (Obino et al., 2017). Finally, in both human primary NK cells and in NK-like cell lines (YTS cells) VAMP7 was shown to be involved in CG fusion (Krzewski et al., 2011a; Marcet-Palacios et al., 2008). VAMP7 and VAMP4 co-localized with Perforin in the CGs, and their siRNA mediated knockdown led to a strong reduction in degranulation activity. VAMP7 was also shown to be involved in interferon-gamma (IFN-γ) (cytokine) release, indicating an indirect effect on CG fusion (Krzewski et al., 2011a). Since these studies did not use techniques allowing observation of CG fusion in real-time, these VAMP isoforms may play a role in CG maturation, which resulted in the observed phenotype.

With the help of pH sensitive (pHuji) and insensitive (mTFP, mCherry) fluorophores combined with TIRFM studies, we found that VAMP7 fuses at the IS along with GzmB containing CGs on anti-CD3 coated coverslips when secretion is stimulated with 10 mM extracellular Ca^{2+} containing solution. Further, VAMP7 down-regulation by siRNA led to a strong reduction in the percentage of cells with CG fusion and

the average number of granules fused per cell (Figure 34D & E). This indicates two possible roles of VAMP7 in reduced CG fusion. First, due to defective transport of CGs toward the IS by its longin domain interactome and second, due to direct involvement in the formation of SNARE complex or a defect in both functions.
Thus, our main findings from primary human $CD8^+$ T cells showed here broaden the available data on human immune cells and identify the vSNARE that mediates CG fusion at the IS. We found a very significant co-localization of VAMP7 with GzmB and Perforin (CG markers), and also demonstrated the simultaneous loss of VAMP7 and release of GzmB at the IS. At the same time, the potential role of VAMP4 in the release of CG could be ruled out by both co-location studies with an EGFP-VAMP4 fusion construct co-transfected with GzmB-mCherry and CG fusion analysis by TIRFM after siRNA mediated VAMP4 knockdown (Figure 35).
It has also been shown that in vitro VAMP7 and SNAP-23 form a SNARE complex with Syntaxin11, and not Syntaxin4, which mediates CG fusion in primary human CTLs (Figure 24). Syntaxin4 appears to be involved in the early stages of IS formation of CTLs by regulating, in conjunction with VAMP8, the fusion of recycling endosomes with the plasma membrane (Marshall et al., 2015; Spessott et al., 2017a). In our study, we showed that CGs (containing VAMP7) arrive much later than recycling endosomes (containing VAMP8) and also fused with lower frequency thanVAMP8 vesicles (Figure 33). These data indicate that VAMP7 and VAMP8 play different roles in CTL function.

4.8 Function of longin domain

VAMP7 is composed of longin, SNARE and tail-anchor transmembrane domain. In addition to its regulatory function, the longin domain of VAMP7 plays an important role in the localization of the protein. It has been shown that the longin domain interacts with AP-3 delta subunit for its late endosomal localization in non-neuronal cells (Martinez-Arca et al., 2000). Consistent with the above findings, overexpression of only longin domain resulted in a strong reduction in the number of CGs appearing in the TIRF plane followed by a significant reduction in CG fusion (Figure 38). Whereas, Rab11 containing vesicle polarization and fusion at the IS was unchanged (Figure 39) in primary human CTLs. There was a slight reduction in the number of Rab11 containing vesicles fusing at the later time points. This might be due to fewer CG fusion at the plasma membrane which indirectly affects the requirement of recycling endosomal fusion.
Taken together, the longin domain of VAMP7 might prove helpful in fighting lethal diseases in humans like FHL and allow modification of the efficiency of CTL cytotoxicity. In the FHL4 (Syntaxin 11 deficiency) condition, the formation of the SNARE complex for CG fusion involving VAMP7, SNAP-23 and Syntaxin11, is an all-or-none reaction. In contrast, the regulatory longin domain in VAMP7 allows for

a subtle interference of subcellular localization and endocytic efficiency. These manipulations would then allow us gradually altering the cytotoxicity of human CTLs in a very subtle way and at least theoretically, enable novel strategies for immunotherapy in pathophysiological conditions.

In agreement with the findings described above and based on our results, it is clear that VAMP7 functions as the major vSNARE for the fusion of CGs in primary, human CTLs. Expression of fusion constructs of VAMP7 along with CG markers, visualization of CG fusion with TIRFM, knockdown of VAMP7 followed by killing assays, pulldowns with Twin-Strep-tag fusion proteins and overexpression of longin domain constructs allowed us to determine the molecular machinery involved in CG fusion. Since this process is of utmost importance to protect our body against infections and tumors, VAMP7 might serve as a major target for the development of innovative drugs for immunotherapy in the future.

5. Outlook

In addition to the already described genetic disease mechanisms associated with mutations in a3 gene, identification of a functional role in CG fusion further enhances our understanding of the overall osteopetrosis disease. Despite having some unanswered questions about the exact molecular machinery involved in the trafficking of CGs, this study using electron microscopy and high-resolution STED microscopy, combined with other high-resolution microscopic techniques such as TIRFM (with 100 nm Z resolution) allowed us to study the role of a3 in primary mouse CTLs.

Since 50 % of human osteopetrosis cases are due to mutations in Tcirg1 gene and lack of redundancy the a3 subunit with other V-ATPase isoforms, which could compensate for a3 function, this subunit could be an important therapeutic target, leading to alternative treatments to bone marrow transplantation.

Based on our results from EM, a3 subunit knockdown in CTLs showed striking morphological defects in CGs affecting a major function of CTLs. This might be the reason behind the increased occurrence of incidence of infections in diseased individuals. Based on our current findings, we postulate that the a3 subunit might play a crucial role in CTL function.

Identification of a vSNARE in CG fusion further enhances our understanding of CTL function. Despite having some unanswered questions about the exact molecular machinery involved in the trafficking of CGs, this study, using high-resolution microscopy and molecular biology techniques, allowed us to study the role of VAMP7 in primary human CTLs. Thus, as an important protein in CG fusion, VAMP7 is a potential target for modulating CTL function.

Lack of human mutations in VAMP7 or FHL phenotype might be due to redundancy of other VAMP isoforms that compensate for VAMP7 function. This is in line with our findings from VAMP7 knockdown combined with TIRFM or target cell killing assay that showed only 50 % reduction in CG fusion compared to control. This result must be verified.

The most important function of CTLs is to release the cytotoxic substances and kill the target cells. Based on our current findings, we postulate that VAMP7 might play a dual role in the transport and fusion of CGs. Targeting the longin domain region specifically in CTLs and modulating it could potentially lead to treatment of inflammatory or autoimmune diseases.

6. Summary

In this study, we identified the a3 subunit of the V-ATPase as a key player mediating the fusion of cytotoxic granules at the immune synapse of primary mouse $CD8^+$ T cells. Knockdown of this subunit seriously affects the integrity of CGs. This is due to the neutralization or lack of proton pumping activity of a3-subunit when its expression is downregulated. The life-threatening autosomal recessive infantile malignant osteopetrosis has led to the identification of Tcirg1 as a major cause of the disease. But the function of a3 isoform in CTLs is unknown.

We measured pH *in vivo* by various pH sensors in CGs from primary mouse $CD8^+$ T lymphocytes. In this study, we generated a GzmB-mTFP knockin mouse as a tool for studying CG fusion in vivo. To investigate which 'a' subunit isoform is involved in pH regulation in CGs, we used siRNA mediated knockdown approach coupled with high-resolution, real-time TIRF microscopy we showed that granule fusion in mouse CTLs is severely affected by a3 knockdown. By using quantitative PCR and SIM microscopy techniques, from the four 'a' isoforms, we showed that a1, a2 and a3 isoforms are expressed in mouse CTLs but only the a3 isoform is localized to CGs and regulates pH homeostasis in CGs. Using a calcein-AM killing assay combined with knockdown we demonstrated that lack of a3 dramatically reduces granule trafficking and fusion at the IS. We also showed with Twin-Strep-tag pulldown assays that a3 did not interact with either syb2 or Rab GTPases, indicating that other Rab proteins may be involved in the movement of CGs or that these interactions might be transient and cannot be detected in our experimental conditions. Finally, we showed by electron microscopy that a3 knockdown in CTLs changes the morphology of CGs dramatically. This confirms a specific role of a3 in CTL function. With super resolution STED microscopy we quantitatively showed that CGs in a3 knockdown CTLs showed greater distances from microtubules labelled with siR-tubulin compared to control *in vivo*.

Overall, our work establishes that a3 is a crucial player in CG biogenesis by keeping the GzmB in active form and protecting Perforin from the degradation due to neutral pH. Thus, the a3 subunit helps in sustained CTL killing function.

In this study, we also identified VAMP7 as the vSNARE that mediates, in conjunction with Syntaxin11 and SNAP-23, the fusion of cytotoxic granules at the immune synapse of primary human T cells. The life-threatening immune disease familial hemophagocytic lymphohistiocytosis type 4 (HLH4) has led to the identification of Syntaxin11 (tSNARE) as an essential component of the SNARE complex mediating cytotoxic granule fusion in human immune cells. But the vSNARE partner on the granule membrane was unknown.

We used primary human $CD8^+$ T lymphocytes to investigate which of the vSNAREs is involved in this process. By using high-resolution, real-time TIRF microscopy we

showed that granule fusion in human CTLs is not sensitive to tetanus toxin and excluded tetanus-sensitive VAMPs as candidates for vSNARE. Of the remaining tetanus-insensitive VAMPs, we demonstrated not only that VAMP7 shows a high degree of co-localization with the cytotoxic granule markers Perforin and GzmB, but that it's knock-down also dramatically reduces granule fusion at the IS. Finally, we showed by Twin-Strep-tag pulldown assay that VAMP7 forms a complex with SNAP-23 and Syntaxin11, thus identifying the members of the SNARE complex that drives fusion. We also showed that overexpression of VAMP7 (longing domain) in CTLs not only inhibited granule polarization in cells coated with anti-CD3 antibody but also reduced the average percentage of cells showing CG fusion without affecting the endosomal exocytosis. This confirms a specific role of VAMP7 longin domain in CG fusion.

Overall, our work establishes that VAMP7 is a central member of the fusion machinery for cytotoxic granules in human T lymphocytes. Because of the unique features of the N-terminus of VAMP7, the longin domain, VAMP7 might actually become a preferential target for drug development in immunotherapy of HLH and related immune diseases.

7. References

Advani, R.J., Yang, B., Prekeris, R., Lee, K.C., Klumperman, J., and Scheller, R.H. (1999). VAMP-7 mediates vesicular transport from endosomes to lysosomes. J. Cell Biol. *146*, 765-776.

Ai, H.W., Henderson, J.N., Remington, S.J., and Campbell, R.E. (2006). Directed evolution of a monomeric, bright and photostable version of Clavularia cyan fluorescent protein: structural characterization and applications in fluorescence imaging. Biochem. J. *400*, 531-540.

Amara, S.G., and Kuhar, M.J. (1993). Neurotransmitter Transporters - Recent Progress. Annu Rev Neurosci *16*, 73-93.

Aniento, F., Gu, F., Parton, R.G., and Gruenberg, J. (1996). An endosomal beta COP is involved in the pH-dependent formation of transport vesicles destined for late endosomes. J Cell Biol *133*, 29-41.

Arosio, D., Ricci, F., Marchetti, L., Gualdani, R., Albertazzi, L., and Beltram, F. (2010). Simultaneous intracellular chloride and pH measurements using a GFP-based sensor. Nat Methods *7*, 516-U544.

Baars, T.L., Petri, S., Peters, C., and Mayer, A. (2007). Role of the V-ATPase in regulation of the vacuolar fission-fusion equilibrium. Mol Biol Cell *18*, 3873-3882.

Barten, R., Torkar, M., Haude, A., Trowsdale, J., and Wilson, M.J. (2001). Divergent and convergent evolution of NK-cell receptors. Trends Immunol *22*, 52-57.

Baumert M, Maycox PR, Navone F, De Camilli P, Jahn R. Synaptobrevin: an integral membrane protein of 18,000 daltons present in small synaptic vesicles of rat brain. EMBO J. 1989;8:379–384.

Bennett MK, Calakos N, Scheller RH. Syntaxin: a synaptic protein implicated in docking of synaptic vesicles at presynaptic active zones. Science. 1992;257:255–259.

Braun, V., Fraisier, V., Raposo, G., Hurbain, I., Sibarita, J.B., Chavrier, P., Galli, T., and Niedergang, F. (2004a). TI-VAMP/VAMP7 is required for optimal phagocytosis of opsonised particles in macrophages. EMBO J. *23*, 4166-4176.

Braun, V., Fraisier, V., Raposo, G., Hurbain, I., Sibarita, J.B., Chavrier, P., Galli, T., and Niedergang, F. (2004b). TI-VAMP/VAMP7 is required for optimal phagocytosis of opsonised particles in macrophages. Embo J *23*, 4166-4176.

Berke, G., and Rosen, D. (1988). Highly lytic in vivo primed cytolytic T lymphocytes devoid of lytic granules and BLT-esterase activity acquire these constituents in the presence of T cell growth factors upon blast transformation in vitro. J Immunol *141*, 1429-1436.

Burgo, A., Sotirakis, E., Simmler, M.C., Verraes, A., Chamot, C., Simpson, J.C., Lanzetti, L., Proux-Gillardeaux, V., and Galli, T. (2009). Role of Varp, a Rab21 exchange factor and TI-VAMP/VAMP7 partner, in neurite growth. EMBO Rep *10*, 1117-1124.

Burkhardt, J.K., Hester, S., Lapham, C.K., and Argon, Y. (1990). The Lytic Granules of Natural-Killer-Cells Are Dual-Function Organelles Combining Secretory and Pre-Lysosomal Compartments. J Cell Biol *111*, 2327-2340.

Bzeih, H (2016). The Role of Synaptobrevin2 in Exo-Endocytosis in Primary Mouse Cytotoxic T Lymphocytes (Unpublished doctoral dissertation). Universitätsklinikum Homburg, Germany.

Chaineau, M., Danglot, L., and Galli, T. (2009). Multiple roles of the vesicular-SNARE TI-VAMP in post-Golgi and endosomal trafficking. FEBS Lett. *583*, 3817-3826.

Chaineau, M., Danglot, L., Proux-Gillardeaux, V., and Galli, T. (2008). Role of HRB in clathrin-dependent endocytosis. J. Biol. Chem. *283*, 34365-34373.

Chen, Y.A., and Scheller, R.H. (2001). SNARE-mediated membrane fusion. Nat Rev Mol Cell Biol *2*, 98-106.

Chang, H.F., Mannebach, S., Beck, A., Ravichandran, K., Krause, E., Frohnweiler, K., Fecher-Trost, C., Schirra, C., Pattu, V., Flockerzi, V., and Rettig, J. (2018). Cytotoxic granule endocytosis depends on the Flower protein. J Cell Biol *217*, 667-683.

Chiaruttini, G., Piperno, G.M., Jouve, M., De Nardi, F., Larghi, P., Peden, A.A., Baj, G., Muller, S., Valitutti, S., Galli, T., and Benvenuti, F. (2016). The SNARE VAMP7 Regulates Exocytic Trafficking of Interleukin-12 in Dendritic Cells. Cell Reports *14*, 2624-2636.

Chitirala, P., Ravichandran, K., Galgano, D., Sleiman, M., Krause, E., Bryceson, Y.T., and Rettig, J. (2019). Cytotoxic Granule Exocytosis From Human Cytotoxic T Lymphocytes Is Mediated by VAMP7. Frontiers in Immunology *10*.

Clague, M.J., Urbe, S., Aniento, F., and Gruenberg, J. (1994). Vacuolar Atpase Activity Is Required for Endosomal Carrier Vesicle Formation. J Biol Chem *269*, 21-24.

Cotter, K., Stransky, L., McGuire, C., and Forgac, M. (2015). Recent Insights into the Structure, Regulation, and Function of the V-ATPases. Trends Biochem Sci *40*, 611-622.
Das, V., Nal, B., Dujeancourt, A., Thoulouze, M.I., Galli, T., Roux, P., Dautry-Varsat, A., and Alcover, A. (2004). Activation-induced polarized recycling targets T cell antigen receptors to the immunological synapse: Involvement of SNARE complexes. Immunity *20*, 577-588.
Daste, F., Galli, T., and Tareste, D. (2015a). Structure and function of longin SNAREs. J Cell Sci *128*, 4263-4272.
Daste, F., Galli, T., and Tareste, D. (2015b). Structure and function of longin SNAREs. J. Cell Sci. *128*, 4263-4272.
DEsposito, M., Ciccodicola, A., Gianfrancesco, F., Esposito, T., Flagiello, L., Mazzarella, R., Schlessinger, D., and DUrso, M. (1996). A synaptobrevin-like gene in the Xq28 pseudoautosomal region undergoes X inactivation. Nature Genetics *13*, 227-229.
Di Giovanni, J., Boudkkazi, S., Mochida, S., Bialowas, A., Samari, N., Leveque, C., Youssouf, F., Brechet, A., Iborra, C., Maulet, Y*., et al.* (2010a). V-ATPase Membrane Sector Associates with Synaptobrevin to Modulate Neurotransmitter Release. Neuron *67*, 268-279.
Di Giovanni, J., Boudkkazi, S., Mochida, S., Bialowas, A., Samari, N., Leveque, C., Youssouf, F., Brechet, A., Iborra, C., Maulet, Y*., et al.* (2010b). V-ATPase membrane sector associates with synaptobrevin to modulate neurotransmitter release. Neuron *67*, 268-279.
Diab, H., Ohira, M., Liu, M., Cobb, E., and Kane, P.M. (2009). Subunit interactions and requirements for inhibition of the yeast V1-ATPase. J Biol Chem *284*, 13316-13325.
Dressel, R., Elsner, L., Novota, P., Kanwar, N., and Fischer von Mollard, G. (2010). The exocytosis of lytic granules is impaired in Vti1b- or Vamp8-deficient CTL leading to a reduced cytotoxic activity following antigen-specific activation. J. Immunol. *185*, 1005-1014.
Fasshauer, D., Sutton, R.B., Brunger, A.T., and Jahn, R. (1998). Conserved structural features of the synaptic fusion complex: SNARE proteins reclassified as Q- and R-SNAREs. Proc Natl Acad Sci U S A *95*, 15781-15786.
Fader, C.M., Aguilera, M.O., and Colombo, M.I. (2012). ATP is released from autophagic vesicles to the extracellular space in a VAMP7-dependent manner. Autophagy *8*, 1741-1756.
Forgac, M. (2007a). Vacuolar ATPases: rotary proton pumps in physiology and pathophysiology. Nat Rev Mol Cell Biol *8*, 917-929.
Forgac, M. (2007b). Vacuolar ATPases: rotary proton pumps in physiology and pathophysiology. Nat Rev Mol Cell Bio *8*, 917-929.
Freeman, M. (2000). Feedback control of intercellular signaling in development. Nature *408*, 313-319.
Frattini, A., Orchard, P.J., Sobacchi, C., Giliani, S., Abinun, M., Mattsson, J.P., Keeling, D.J., Andersson, A.K., Wallbrandt, P., Zecca, L*., et al.* (2000). Defects in TCIRG1 subunit of the vacuolar proton pump are responsible for a subset of human autosomal recessive osteopetrosis. Nature Genetics *25*, 343-346.
Galli, T., Zahraoui, A., Vaidyanathan, V.V., Raposo, G., Tian, J.M., Karin, M., Niemann, H., and Louvard, D. (1998). A novel tetanus neurotoxin-insensitive vesicle-associated membrane protein in SNARE complexes of the apical plasma membrane of epithelial cells. Mol Biol Cell *9*, 1437-1448.
Germain, R.N. (2002). T-cell development and the CD4-CD8 lineage decision. Nature Reviews Immunology *2*, 309-322.
Gerritsen, E.J.A., Vossen, J.M., Vanloo, I.H.G., Hermans, J., Helfrich, M.H., Griscelli, C., and Fischer, A. (1994). Autosomal Recessive Osteopetrosis - Variability of Findings at Diagnosis and during the Natural Course. Pediatrics *93*, 247-253.
Griesbeck, O., Baird, G.S., Campbell, R.E., Zacharias, D.A., and Tsien, R.Y. (2001). Reducing the environmental sensitivity of yellow fluorescent protein. Mechanism and applications. J Biol Chem *276*, 29188-29194.
Godfrey, D.I., Kennedy, J., Suda, T. & Zlotnik, A. A developmental pathway involving four phenotypically and functionally distinct subsets of $CD3^{-}CD4^{-}CD8^{-}$ triple-negative adult mouse thymocytes defined by CD44 and CD25 expression. J. Immunol. **150**, 4244–4252 (1993).
Grakoui, A., Bromley, S.K., Sumen, C., Davis, M.M., Shaw, A.S., Allen, P.M., and Dustin, M.L. (1999). The immunological synapse: a molecular machine controlling T cell activation. Science *285*, 221-227.
Griffiths G.M., and Isaaz S. 1993. Granzymes A and B are targeted to the lytic granules of lymphocytes by the mannose-6-phosphate receptor. J. Cell Biol. 120:885–896 10.1083/jcb.120.4.885

Hazeldine, J., and Lord, J.M. (2015). Innate immunesenescence: underlying mechanisms and clinical relevance. Biogerontology *16*, 187-201.
Garcia KC, Degano M, Stanfield RL, Brunmark A, Jackson MR, Peterson PA, Teyton L, Wilson IA. An alphabeta T cell receptor structure at 2.5 A and its orientation in the TCR-MHC complex. Science. 1996;274:209–219.
Heinemann, T., Bulwin, G.C., Randall, J., Schnieders, B., Sandhoff, K., Volk, H.D., Milford, E., Gullans, S.R., and Utku, N. (1999). Genomic organization of the gene coding for TIRC7, a novel membrane protein essential for T cell activation. Genomics *57*, 398-406.
Heidelberger R, Heinemann C, Neher E, Matthews G. Calcium dependence of the rate of exocytosis in a synaptic terminal. Nature. 1994;371:513–5.
Hiesinger, P.R., Fayyazuddin, A., Mehta, S.Q., Rosenmund, T., Schulze, K.L., Zhai, R.G., Verstreken, P., Cao, Y., Zhou, Y., Kunz, J., and Bellen, H.J. (2005). The v-ATPase V-0 subunit a1 is required for a late step in synaptic vesicle exocytosis in Drosophila. Cell *121*, 607-620.
Humeau, Y., Doussau, F., Grant, N.J., and Poulain, B. (2000). How botulinum and tetanus neurotoxins block neurotransmitter release. Biochimie *82*, 427-446.
Huppa, J.B., and Davis, M.M. (2003). T-cell-antigen recognition and the immunological synapse. Nature Reviews Immunology *3*, 973-983.
Hurtado-Lorenzo, A., Skinner, M., El Annan, J., Futai, M., Sun-Wada, G.H., Bourgoin, S., Casanova, J., Wildeman, A., Ausiello, D., Brown, D., and Marshansky, V. (2006). V-ATPase interacts with ARNO and Arf6 in early endosomes and regulates the protein degradative pathway. Faseb Journal *20*, A1225-A1225.
Kabanova, A., Zurli, V., and Baldari, C.T. (2018). Signals Controlling Lytic Granule Polarization at the Cytotoxic immune Synapse. Front Immunol *9*.
Kataoka, T., Sato, M., Kondo, S., and Nagai, K. (1996). Estimation of pH and the number of lytic granules in a CD8+ CTL clone treated with an inhibitor of vacuolar type H(+)-ATPase concanamycin A. Biosci Biotechnol Biochem *60*, 1729-1731.
Kataoka, T., Takaku, K., Magae, J., Shinohara, N., Takayama, H., Kondo, S., and Nagai, K. (1994). Acidification Is Essential for Maintaining the Structure and Function of Lytic Granules of Ctl - Effect of Concanamycin-a, an Inhibitor of Vacuolar-Type H+-Atpase, on Ctl-Mediated Cytotoxicity. Journal of Immunology *153*, 3938-3947.
Kataoka, T., Togashi, K., Takayama, H., Takaku, K., and Nagai, K. (1997). Inactivation and proteolytic degradation of perforin within lytic granules upon neutralization of acidic pH. Immunology *91*, 493-500.
Kent, H.M., Evans, P.R., Schafer, I.B., Gray, S.R., Sanderson, C.M., Luzio, J.P., Peden, A.A., and Owen, D.J. (2012). Structural basis of the intracellular sorting of the SNARE VAMP7 by the AP3 adaptor complex. Dev Cell *22*, 979-988.
Klenchin, V.A., and Martin, T.F. (2000). Priming in exocytosis: attaining fusion-competence after vesicle docking. Biochimie *82*, 399-407.
Klemmer, P., Smit, A.B., and Li, K.W. (2009). Proteomics analyses of immuno-precipitated synaptic protein complexes. J Proteomics *72*, 82-90.
Kong, Y.Y., Yoshida, H., Sarosi, I., Tan, H.L., Timms, E., Capparelli, C., Morony, S., Oliveira-dos-Santos, A.J., Van, G., Itie, A.*, et al.* (1999). OPGL is a key regulator of osteoclastogenesis, lymphocyte development and lymph-node organogenesis. Nature *397*, 315-323.
Kornak, U., Reynders, E., Dimopoulou, A., van Reeuwijk, J., Fischer, B., Rajab, A., Budde, B., Nurnberg, P., Foulquier, F., Lefeber, D.*, et al.* (2008). Impaired glycosylation and cutis laxa caused by mutations in the vesicular H+-ATPase subunit ATP6V0A2. Nature Genetics *40*, 32-34.
Kornak, U., Schulz, A., Friedrich, W., Uhlhaas, S., Kremens, B., Voit, T., Hasan, C., Bode, U., Jentsch, T.J., and Kubisch, C. (2000). Mutations in the a3 subunit of the vacuolar H+-ATPase cause infantile malignant osteopetrosis. Hum Mol Genet *9*, 2059-2063.
Krzewski, K., Gil-Krzewska, A., Watts, J., Stern, J.N., and Strominger, J.L. (2011a). VAMP4- and VAMP7-expressing vesicles are both required for cytotoxic granule exocytosis in NK cells. Eur. J. Immunol. *41*, 3323-3329.
Krzewski, K., Gil-Krzewska, A., Watts, J., Stern, J.N.H., and Strominger, J.L. (2011b). VAMP4- and VAMP7-expressing vesicles are both required for cytotoxic granule exocytosis in NK cells. Eur J Immunol *41*, 3323-3329.
Kummerow, C., Schwarz, E.C., Bufe, B., Zufall, F., Hoth, M., and Qu, B. (2014). A simple, economic, time-resolved killing assay. Eur J Immunol *44*, 1870-1872.
Larghi, P., Williamson, D.J., Carpier, J.M., Dogniaux, S., Chemin, K., Bohineust, A., Danglot, L., Gaus, K., Galli, T., and Hivroz, C. (2013a). VAMP7 controls T cell activation by regulating

the recruitment and phosphorylation of vesicular Lat at TCR-activation sites. Nat Immunol *14*, 723-+.
Larghi, P., Williamson, D.J., Carpier, J.M., Dogniaux, S., Chemin, K., Bohineust, A., Danglot, L., Gaus, K., Galli, T., and Hivroz, C. (2013b). VAMP7 controls T cell activation by regulating the recruitment and phosphorylation of vesicular Lat at TCR-activation sites. Nat. Immunol. *14*, 723-731.
Lazner, F., Gowen, M., Pavasovic, D., and Kola, I. (1999). Osteopetrosis and osteoporosis: two sides of the same coin. Hum Mol Genet *8*, 1839-1846.
Lee, S.H., Rho, J., Jeong, D., Sul, J.Y., Kim, T., Kim, N., Kang, J.S., Miyamoto, T., Suda, T., Lee, S.K.*, et al.* (2006). v-ATPase V0 subunit d2-deficient mice exhibit impaired osteoclast fusion and increased bone formation. Nat Med *12*, 1403-1409.
Liegeois, S., Benedetto, A., Garnier, J.M., Schwab, Y., and Labouesse, M. (2006). The V0-ATPase mediates apical secretion of exosomes containing Hedgehog-related proteins in Caenorhabditis elegans. J Cell Biol *173*, 949-961.
Lippert, U., Ferrari, D.M., and Jahn, R. (2007). Endobrevin/VAMP8 mediates exocytotic release of hexosaminidase from rat basophilic leukaemia cells. Febs Lett *581*, 3479-3484.
Liu, S., Sahid, M.N.A., Takemasa, E., Maeyama, K., and Mogi, M. (2018). Zoledronate modulates intracellular vesicle trafficking in mast cells via disturbing the interaction of myosinVa/Rab3a and sytaxin4/VAMP7. Biochem. Pharmacol. *151*, 18-25.
Lledo, P.M., Zhang, X., Sudhof, T.C., Malenka, R.C., and Nicoll, R.A. (1998). Postsynaptic membrane fusion and long-term potentiation. Science *279*, 399-403.
Logan, M.R., Lacy, P., Odemuyiwa, S.O., Steward, M., Davoine, F., Kita, H., and Moqbel, R. (2006). A critical role for vesicle-associated membrane protein-7 in exocytosis from human eosinophils and neutrophils. Allergy *61*, 777-784.
Loo, L.S., Hwang, L.A., Ong, Y.M., Tay, H.S., Wang, C.C., and Hong, W. (2009). A role for endobrevin/VAMP8 in CTL lytic granule exocytosis. Eur. J. Immunol. *39*, 3520-3528.
Mahon, M.J. (2011). pHluorin2: an enhanced, ratiometric, pH-sensitive green florescent protein. Adv Biosci Biotechnol *2*, 132-137.
Mallard, F., Tang, B.L., Galli, T., Tenza, D., Saint-Pol, A., Yue, X., Antony, C., Hong, W.J., Goud, B., and Johannes, L. (2002). Early/recycling endosomes-to-TGN transport involves two SNARE complexes and a Rab6 isoform. J Cell Biol *156*, 653-664.
Manders, E.M.M., Verbeek, F.J., and Aten, J.A. (1993). Measurement of Colocalization of Objects in Dual-Color Confocal Images. Journal of Microscopy-Oxford *169*, 375-382.
Marcet-Palacios, M., Odemuyiwa, S.O., Coughlin, J.J., Garofoli, D., Ewen, C., Davidson, C.E., Ghaffari, M., Kane, K.P., Lacy, P., Logan, M.R.*, et al.* (2008). Vesicle-associated membrane protein 7 (VAMP-7) is essential for target cell killing in a natural killer cell line. Biochem. Biophys. Res. Commun. *366*, 617-623.
Marks, S.C., Seifert, M.F., and Lane, P.W. (1985). Osteosclerosis, a Recessive Skeletal Mutation on Chromosome 19 in the Mouse. J Hered *76*, 171-176.
Marshall, M.R., Pattu, V., Halimani, M., Maier-Peuschel, M., Muller, M.L., Becherer, U., Hong, W., Hoth, M., Tschernig, T., Bryceson, Y.T., and Rettig, J. (2015). VAMP8-dependent fusion of recycling endosomes with the plasma membrane facilitates T lymphocyte cytotoxicity. J. Cell Biol. *210*, 135-151.
Marshansky, V., and Futai, M. (2008). The V-type H+-ATPase in vesicular trafficking: targeting, regulation and function. Curr Opin Cell Biol *20*, 415-426.
Martinez-Arca, S., Alberts, P., Zahraoui, A., Louvard, D., and Galli, T. (2000). Role of tetanus neurotoxin insensitive vesicle-associated membrane protein (TI-VAMP) in vesicular transport mediating neurite outgrowth. J Cell Biol *149*, 889-899.
Martinez-Arca, S., Rudge, R., Vacca, M., Raposo, G., Camonis, J., Proux-Gillardeaux, V., Daviet, L., Formstecher, E., Hamburger, A., Filippini, F.*, et al.* (2003). A dual mechanism controlling the localization and function of exocytic v-SNAREs. Proc. Natl. Acad. Sci. U. S. A. *100*, 9011-9016.
Matarazzo, M.R., De Bonis, M.L., Gregory, R.I., Vacca, M., Hansen, R.S., Mercadante, G., D'Urso, M., Feil, R., and D'Esposito, M. (2002). Allelic inactivation of the pseudoautosomal gene SYBL1 is controlled by epigenetic mechanisms common to the X and Y chromosomes. Hum Mol Genet *11*, 3191-3198.
Matsumoto, N., Sekiya, M., Tohyama, K., Ishiyama-Matsuura, E., Sun-Wada, G.H., Wada, Y., Futai, M., and Nakanishi-Matsui, M. (2018). Essential Role of the a3 Isoform of V-ATPase in Secretory Lysosome Trafficking via Rab7 Recruitment. Sci Rep *8*, 6701.

Matti, U., Pattu, V., Halimani, M., Schirra, C., Krause, E., Liu, Y., Weins, L., Chang, H.F., Guzman, R., Olausson, J*., et al.* (2013a). Synaptobrevin2 is the v-SNARE required for cytotoxic T-lymphocyte lytic granule fusion. Nat. Commun. *4*, 1439.
Matti, U., Pattu, V., Halimani, M., Schirra, C., Krause, E., Liu, Y.Y., Weins, L., Chang, H.F., Guzman, R., Olausson, J*., et al.* (2013b). Synaptobrevin2 is the v-SNARE required for cytotoxic T-lymphocyte lytic granule fusion. Nature Communications *4*.
Ming, M., Schirra, C., Becherer, U., Stevens, D.R., and Rettig, J. (2015). Behavior and Properties of Mature Lytic Granules at the Immunological Synapse of Human Cytotoxic T Lymphocytes. PLoS One *10*, e0135994.
Mollinedo, F., Calafat, J., Janssen, H., Martin-Martin, B., Canchado, J., Nabokina, S.M., and Gajate, C. (2006). Combinatorial SNARE complexes modulate the secretion of cytoplasmic granules in human neutrophils. J. Immunol. *177*, 2831-2841.
Mollinedo, F., Martin-Martin, B., Calafat, J., Nabokina, S.M., and Lazo, P.A. (2003). Role of vesicle-associated membrane protein-2, through Q-soluble N-ethylmaleimide-sensitive factor attachment protein receptor/R-soluble N-ethylmaleimide-sensitive factor attachment protein receptor interaction, in the exocytosis of specific and tertiary granules of human neutrophils. Journal of Immunology *170*, 1034-1042.
Morel, N., Dedieu, J.C., and Philippe, J.M. (2003). Specific sorting of the a1 isoform of the V-H(+)ATPase a subunit to nerve terminals where it associates with both synaptic vesicles and the presynaptic plasma membrane. J Cell Sci *116*, 4751-4762.
Monks, C.R., Freiberg, B.A., Kupfer, H., Sciaky, N., and Kupfer, A. (1998). Three-dimensional segregation of supramolecular activation clusters in T cells. Nature *395*, 82-86.
Morel, N., and Poea-Guyon, S. (2015). The membrane domain of vacuolar H(+)ATPase: a crucial player in neurotransmitter exocytotic release. Cell Mol Life Sci *72*, 2561-2573.
Nakanishi-Matsui, M., Sekiya, M., Nakamoto, R.K., and Futai, M. (2010). The mechanism of rotating proton pumping ATPases. Bba-Bioenergetics *1797*, 1343-1352.
Obino, D., Diaz, J., Saez, J.J., Ibanez-Vega, J., Saez, P.J., Alamo, M., Lankar, D., and Yuseff, M.I. (2017). Vamp-7-dependent secretion at the immune synapse regulates antigen extraction and presentation in B-lymphocytes. Mol Biol Cell *28*, 890-897.
Oishi, Y., Arakawa, T., Tanimura, A., Itakura, M., Takahashi, M., Tajima, Y., Mizoguchi, I., and Takuma, T. (2006). Role of VAMP-2, VAMP-7, and VAMP-8 in constitutive exocytosis from HSY cells. Histochem. Cell Biol. *125*, 273-281.
Oka, T., Toyomura, T., Honjo, K., Wada, Y., and Futai, M. (2001). Four subunit a isoforms of Caenorhabditis elegans vacuolar H+-ATPase - Cell-specific expression during development. J Biol Chem *276*, 33079-33085.
Palagano, E., Menale, C., Sobacchi, C., and Villa, A. (2018). Genetics of Osteopetrosis. Curr Osteoporos Rep *16*, 13-25.
Pattu, V., Qu, B., Schwarz, E.C., Strauss, B., Weins, L., Bhat, S.S., Halimani, M., Marshall, M., Rettig, J., and Hoth, M. (2012). SNARE protein expression and localization in human cytotoxic T lymphocytes. Eur J Immunol *42*, 470-475.
Pearson, K. (1909). Determination of the Coefficient of Correlation. Science *30*, 23-25.
Pietrement, C., Sun-Wada, G.H., Da Silva, N., McKee, M., Marshansky, V., Brown, D., Futai, M., and Breton, S. (2006). Distinct expression patterns of different subunit Isoforms of the V-ATPase in the rat epididymis. Biol Reprod *74*, 185-194.
Pocard, T., Le Bivic, A., Galli, T., and Zurzolo, C. (2007). Distinct v-SNAREs regulate direct and indirect apical delivery in polarized epithelial cells. J. Cell Sci. *120*, 3309-3320.
Podack, E.R., and Kupfer, A. (1991). T-Cell Effector Functions - Mechanisms for Delivery of Cytotoxicity and Help. Annu Rev Cell Biol *7*, 479-504.
Poea-Guyon, S., Ammar, M.R., Erard, M., Amar, M., Moreau, A.W., Fossier, P., Gleize, V., Vitale, N., and Morel, N. (2013). The V-ATPase membrane domain is a sensor of granular pH that controls the exocytotic machinery. J Cell Biol *203*, 283-298.
Pols, M.S., van Meel, E., Oorschot, V., ten Brink, C., Fukuda, M., Swetha, M.G., Mayor, S., and Klumperman, J. (2013). hVps41 and VAMP7 function in direct TGN to late endosome transport of lysosomal membrane proteins. Nat Commun *4*.
Porcelli, A.M., Ghelli, A., Zanna, C., Pinton, P., Rizzuto, R., and Rugolo, M. (2005). pH difference across the outer mitochondrial membrane measured with a green fluorescent protein mutant. Biochem Biophys Res Commun *326*, 799-804.
Proux-Gillardeaux, V., Rudge, R., and Galli, T. (2005). The tetanus neurotoxin-sensitive and insensitive routes to and from the plasma membrane: Fast and slow pathways? Traffic *6*, 366-373.

Pryor, P.R., Jackson, L., Gray, S.R., Edeling, M.A., Thompson, A., Sanderson, C.M., Evans, P.R., Owen, D.J., and Luzio, J.P. (2008). Molecular basis for the sorting of the SNARE VAMP7 into endocytic clathrin-coated vesicles by the ArfGAP Hrb. Cell *134*, 817-827.
Pryor, P.R., Mullock, B.M., Bright, N.A., Lindsay, M.R., Gray, S.R., Richardson, S.C., Stewart, A., James, D.E., Piper, R.C., and Luzio, J.P. (2004a). Combinatorial SNARE complexes with VAMP7 or VAMP8 define different late endocytic fusion events. EMBO Rep *5*, 590-595.
Pryor, P.R., Mullock, B.M., Bright, N.A., Lindsay, M.R., Gray, S.R., Richardson, S.C.W., Stewart, A., James, D.E., Piper, R.C., and Luzio, J.P. (2004b). Combinatorial SNARE complexes with VAMP7 or VAMP8 define different late endocytic fusion events. Embo Rep *5*, 590-595.
Pui, J.C., Allman, D., Xu, L., DeRocco, S., Karnell, F.G., Bakkour, S., Lee, J.Y., Kadesch, T., Hardy, R.R., Aster, J.C., and Pear, W.S. (1999). Notch1 expression in early lymphopoiesis influences B versus T lineage determination. Immunity *11*, 299-308.
Qin, A., Cheng, T.S., Pavlos, N.J., Lin, Z., Dai, K.R., and Zheng, M.H. (2012). V-ATPases in osteoclasts: Structure, function and potential inhibitors of bone resorption. Int J Biochem Cell B *44*, 1422-1435.
Raimondo, J.V., Joyce, B., Kay, L., Schlagheck, T., Newey, S.E., Srinivas, S., and Akerman, C.J. (2013). A genetically-encoded chloride and pH sensor for dissociating ion dynamics in the nervous system. Front Cell Neurosci *7*, 202.
Sander, L.E., Frank, S.P., Bolat, S., Blank, U., Galli, T., Bigalke, H., Bischoff, S.C., and Lorentz, A. (2008). Vesicle associated membrane protein (VAMP)-7 and VAMP-8, but not VAMP-2 or VAMP-3, are required for activation-induced degranulation of mature human mast cells. Eur. J. Immunol. *38*, 855-863.
Shen, Y., Rosendale, M., Campbell, R.E., and Perrais, D. (2014). pHuji, a pH-sensitive red fluorescent protein for imaging of exo- and endocytosis. J. Cell Biol. *207*, 419-432.
Siddiqi, S.A., Mahan, J., Siddiqi, S., Gorelick, F.S., and Mansbach, C.M. (2006). Vesicle-associated membrane protein 7 is expressed in intestinal ER. J Cell Sci *119*, 943-950.
Smyth, M.J., Kelly, J.M., Sutton, V.R., Davis, J.E., Browne, K.A., Sayers, T.J., and Trapani, J.A. (2001). Unlocking the secrets of cytotoxic granule proteins. J Leukocyte Biol *70*, 18-29.
Spessott, W.A., Sanmillan, M.L., Kulkarni, V.V., McCormick, M.E., and Giraudo, C.G. (2017a). Syntaxin 4 mediates endosome recycling for lytic granule exocytosis in cytotoxic T-lymphocytes. Traffic *18*, 442-452.
Spessott, W.A., Sanmillan, M.L., McCormick, M.E., Kulkarni, V.V., and Giraudo, C.G. (2017b). SM protein Munc18-2 facilitates transition of Syntaxin 11-mediated lipid mixing to complete fusion for T-lymphocyte cytotoxicity. Proc Natl Acad Sci U S A *114*, E2176-E2185.
Sutton, V.R., J.E. Davis, M. Cancilla, R.W. Johnstone, A.A. Ruefli, K. Sedelies, K.A. Browne, and J.A. Trapani. 2000. Initiation of apoptosis by granzyme B requires direct cleavage of bid, but not direct granzyme B–mediated caspase activation. J. Exp. Med. 192:1403–1414.
Sun-Wada, G.H., Tabata, H., Kawamura, N., Futai, M., and Wada, Y. (2007). Differential expression of a subunit isoforms of the vacuolar-type proton pump ATPase in mouse endocrine tissues. Cell Tissue Res *329*, 239-248.
Sun-Wada, G.H., Toyomura, T., Murata, Y., Yamamoto, A., Futai, M., and Wada, Y. (2006). The a3 isoform of V-ATPase regulates insulin secretion from pancreatic beta-cells. J Cell Sci *119*, 4531-4540.
Sun-Wada, G.H., and Wada, Y. (2013). Vacuolar-type proton pump ATPases: Acidification and pathological relationships. Histol Histopathol *28*, 805-815.
Susani, L., Pangrazio, A., Sobacchi, C., Taranta, A., Mortier, G., Savarirayan, R., Villa, A., Orchard, P., Vezzoni, P., Albertini, A*., et al.* (2004). TCIRG1-dependent recessive osteopetrosis: mutation analysis, functional identification of the splicing defects, and in vitro rescue by U1 snRNA. Hum Mutat *24*, 225-235.
Toei, M., Saum, R., and Forgac, M. (2010). Regulation and isoform function of the V-ATPases. Biochemistry *49*, 4715-4723.
Toei, M., Toei, S., and Forgac, M. (2011). Definition of membrane topology and identification of residues important for transport in subunit a of the vacuolar ATPase. J Biol Chem *286*, 35176-35186.
Toyomura, T., Murata, Y., Yamamoto, A., Oka, T., Sun-Wada, G.H., Wada, Y., and Futai, M. (2003). From lysosomes to the plasma membrane - Localization of vacuolar type H+-ATPase with the a3 isoform during osteoclast differentiation. J Biol Chem *278*, 22023-22030.

Toyomura, T., Oka, T., Yamaguchi, C., Wada, Y., and Futai, M. (2000). Three subunit a isoforms of mouse vacuolar H(+)-ATPase. Preferential expression of the a3 isoform during osteoclast differentiation. J Biol Chem *275*, 8760-8765.
van der Sluijs, P., Zibouche, M., and van Kerkhof, P. (2013). Late steps in secretory lysosome exocytosis in cytotoxic lymphocytes. Front Immunol *4*, 359.
Verderio, C., Cagnoli, C., Bergami, M., Francolini, M., Schenk, U., Colombo, A., Riganti, L., Frassoni, C., Zuccaro, E., Danglot, L.*, et al.* (2012). TI-VAMP/VAMP7 is the SNARE of secretory lysosomes contributing to ATP secretion from astrocytes. Biol Cell *104*, 213-228.
von Boehmer, H., Teh, H.S., and Kisielow, P. (1989). The thymus selects the useful, neglects the useless and destroys the harmful. Immunol Today *10*, 57-61.
Vivona, S., Liu, C.W., Strop, P., Rossi, V., Filippini, F., and Brunger, A.T. (2010). The longin SNARE VAMP7/TI-VAMP adopts a closed conformation. J. Biol. Chem. *285*, 17965-17973.
Xiao, Y.T., Xiang, L.X., and Shao, J.Z. (2008). Vacuolar H(+)-ATPase. Int J Biochem Cell B *40*, 2002-2006.

8. Publications

1. **Chitirala, P.**, Ravichandran, K., Galgano, D., Sleiman, M., Krause, E., Bryceson, Y.T., and Rettig, J. (2019). Cytotoxic Granule Exocytosis From Human Cytotoxic T Lymphocytes Is Mediated by VAMP7. **Frontiers in Immunology** *10*.

2. Ratai, O., Schirra, C., Rajabov, E., Brunk, I., Ahnert-Hilger, G., **Chitirala, P.**, Becherer, U., Stevens, D.R., and Rettig, J. (2019). An Alternative Exon of CAPS2 Influences Catecholamine Loading into LDCVs of Chromaffin Cells. **Journal of Neuroscience** *39*, 18-27.

3. Chang, H.F., Bzeih, H., **Chitirala, P.**, Ravichandran, K., Sleiman, M., Krause, E., Hahn, U., Pattu, V., and Rettig, J. (2017). Preparing the lethal hit: interplay between exo- and endocytic pathways in cytotoxic T lymphocytes. **Cell Mol Life Sci** *74*, 399-408.

4. Mahanty, S., Ravichandran, K., **Chitirala, P**., Prabha, J., Jani, R.A., and Setty, S.R.G. (2016). Rab9A is required for delivery of cargo from recycling endosomes to melanosomes. **Pigm Cell Melanoma R** *29*, 43-59.

5. Chang, H.F., Bzeih, H., Schirra, C., **Chitirala, P**., Halimani, M., Cordat, E., Krause, E., Rettig, J., and Pattu, V. (2016). Endocytosis of Cytotoxic Granules Is Essential for Multiple Killing of Target Cells by T Lymphocytes. **Journal of Immunology** 197, 2473-2484.

9. Disclosure

This work was funded by:

The **Sonderforschungsbereich 894 (SFB894):**
Calcium Signals: Molecular Mechanisms and Integrative Functions

&

IRTG 1830 (German/Canadian Research Training Group)
Complex Membrane Proteins In Cellular Development and Disease

From April 14th, 2014- July 31st, 2018.

All Experiments were performed in the department of Cellular Neurophysiology, Prof. Dr. Jens Rettig Laboratory, CIPMM-University of Saarland, 66421, Homburg (Saar), Germany.

The curriculum vitae was removed from the electronic version of the doctoral thesis for reasons of data protection!